




Spring 5-17-2010

Statistical Medial Model dor Cardiac Segmentation and Morphometry

Hui Sun

University of Pennsylvania, sunhui@seas.upenn.edu

Follow this and additional works at: <http://repository.upenn.edu/edissertations>

 Part of the [Applied Mathematics Commons](#), [Biomedical Engineering and Bioengineering Commons](#), [Cardiovascular System Commons](#), and the [Other Analytical, Diagnostic and Therapeutic Techniques and Equipment Commons](#)

Recommended Citation

Sun, Hui, "Statistical Medial Model dor Cardiac Segmentation and Morphometry" (2010). *Publicly Accessible Penn Dissertations*. 97.
<http://repository.upenn.edu/edissertations/97>

This paper is posted at ScholarlyCommons. <http://repository.upenn.edu/edissertations/97>
For more information, please contact libraryrepository@pobox.upenn.edu.

Statistical Medial Model for Cardiac Segmentation and Morphometry

Abstract

In biomedical image analysis, shape information can be utilized for many purposes. For example, irregular shape features can help identify diseases; shape features can help match different instances of anatomical structures for statistical comparison; and prior knowledge of the mean and possible variation of an anatomical structure's shape can help segment a new example of this structure in noisy, low-contrast images. A good shape representation helps to improve the performance of the above techniques. The overall goal of the proposed research is to develop and evaluate methods for representing shapes of anatomical structures. The medial model is a shape representation method that models a 3D object by explicitly defining its skeleton (medial axis) and deriving the object's boundary via "inverse-skeletonization". This model represents shape compactly, and naturally expresses descriptive global shape features like "thickening", "bending", and "elongation". However, its application in biomedical image analysis has been limited, and it has not yet been applied to the heart, which has a complex shape. In this thesis, I focus on developing efficient methods to construct the medial model, and apply it to solve biomedical image analysis problems. I propose a new 3D medial model which can be efficiently applied to complex shapes. The proposed medial model closely approximates the medial geometry along medial edge curves and medial branching curves by soft-penalty optimization and local correction. I further develop a scheme to perform model-based segmentation using a statistical medial model which incorporates prior shape and appearance information. The proposed medial models are applied to a series of image analysis tasks. The 2D medial model is applied to the corpus callosum which results in an improved alignment of the patterns of commissural connectivity compared to a volumetric registration method. The 3D medial model is used to describe the myocardium of the left and right ventricles, which provides detailed thickness maps characterizing different disease states. The model-based myocardium segmentation scheme is tested in a heterogeneous adult MRI dataset. Our segmentation experiments demonstrate that the statistical medial model can accurately segment the ventricular myocardium and provide useful parameters to characterize heart function.

Degree Type

Dissertation

Degree Name

Doctor of Philosophy (PhD)

Graduate Group

Bioengineering

First Advisor

Paul A. Yushkevich

Second Advisor

James C. Gee

Keywords

Heart Model, Image Segmentation, Medial Model, Medial Axis, Shape Representation, Image Processing

Subject Categories

Applied Mathematics | Biomedical Engineering and Bioengineering | Cardiovascular System | Other
Analytical, Diagnostic and Therapeutic Techniques and Equipment

STATISTICAL MEDIAL MODEL FOR
CARDIAC SEGMENTATION AND MORPHOMETRY

Hui Sun

A DISSERTATION

in

Bioengineering

Presented to the Faculties of the University of Pennsylvania

in

Partial Fulfillment of the Requirements for the

Degree of Doctor of Philosophy

2010

Supervisor of Dissertation

Co-supervisor

Signature: _____

Signature: _____

Paul A. Yushkevich

James C. Gee

Assistant Professor, Radiology

Associate Professor, Radiology

Graduate Group Chairperson

Signature: _____

Susan S. Margulies, Professor, Bioengineering

Dissertation Committee

Guido Gerig, Professor, Computer Science

Alejandro F. Frangi, Associate Professor, Information and Communication
Technologies

Jeffrey C. Hellinger, Assistant Professor, Radiology and Cardiology

Andrew Tsourkas, Assistant Professor, Bioengineering

Acknowledgements

I would like to take the opportunity to thank many people who have contributed to the thesis and research in one way or another.

First, my sincere gratitude goes to my advisors, Dr. Paul A. Yushkevich and Dr. James C. Gee, for the time and effort they have invested in my education over the past five years. I have worked closely with Paul and he is the perfect type of advisor that I can think of: he has real passion on research but also knows how to keep the balance, he is always willing to listen and leaves you enough freedom to explore, he always shares his insights using clearest expressions, and he is always ready to help, not only on research but also on all life aspects. Jim, although less involved in my research details, has always been valuable resource on matters professional and personal. I can never forget during the first time I met him at the interview how he explained shape and diffeomorphisms to me that totally intrigued my interest on medical image analysis. And I can never forget his kind words on my wedding day that almost bring down my tears.

My committee members, Dr. Guido Gerig, Dr. Alejandro F. Frangi, Dr. Jeffrey C. Hellinger and Dr. Andrew Tsourkas have helped shape my research and lead me in worthwhile directions. I thank them for their interest in my research and education. Especially, Dr. Alejandro F. Frangi and his group at University Pompeu Fabra have helped me enormously along the way by involving themselves in my research, collaborating on research projects, and co-authoring publications. And Dr. Jeffrey C. Hellinger deserves my special thanks for showing me how the real clinical practice is conducted and how my research work can be useful in it.

I need to thank the current and former lab mates in Penn Image Computing and Science Lab (PICSL) who shared their knowledge in the weekly lab meeting and during daily discussion. Hui (Gary) Zhang, Philip Cook, Jeffrey Duda, Brian Avants, Sandhitsu Das and Hongzhi Wang are coauthors of my papers. My research won't be complete without their contribution. And I thank Nick Tustison, Yuanjie Zheng, Suyash P. Awate and Zhuang Song for the discussion and insights. Jeffrey Duda, Gang Song and Jon Perry kept my workstation running when I was in Seattle, which is essential for me to stay connected and keep working.

I thank my friends, especially Dan Huang, Yingting Liu and Ye Xing. The winter in Philadelphia would have been much colder without their company.

I thank Dr. Britton Chance and his optical imaging lab who supported me during my first year of doctoral study at Penn. My study in the following years and the work on medial modeling are funded by NIH grants AG027785 and NS061111.

Finally and most of all I would like to thank my families who have made it all worthwhile. Throughout my life, my mom Chuanhua Yin and my dad Dianshuang Sun have given me all their love and constant support. They are my first teachers on many things and I am still learning from them, especially their life attitude. And I can not imagine my life without my husband, Peng Li, who fixes all the problems in my apartment, my computer and my brain. Thank him for his unflagging support and daily encouragement. And I thank my dearest daughter, Grace, who makes every day an adventure for me.

ABSTRACT

STATISTICAL MEDIAL MODEL FOR CARDIAC SEGMENTATION AND MORPHOMETRY

Hui Sun

Paul A. Yushkevich and James C. Gee

In biomedical image analysis, shape information can be utilized for many purposes. For example, irregular shape features can help identify diseases; shape features can help match different instances of anatomical structures for statistical comparison; and prior knowledge of the mean and possible variation of an anatomical structure's shape can help segment a new example of this structure in noisy, low-contrast images. A good shape representation helps to improve the performance of the above techniques. The overall goal of the proposed research is to develop and evaluate methods for representing shapes of anatomical structures. The medial model is a shape representation method that models a 3D object by explicitly defining its skeleton (medial axis) and deriving the object's boundary via "inverse-skeletonization". This model represents shape compactly, and naturally expresses descriptive global shape features like "thickening", "bending", and "elongation". However, its application in biomedical image analysis has been limited, and it has not yet been applied to the heart, which has a complex shape. In this thesis, I focus on developing efficient methods to construct the medial model, and apply it to solve biomedical image analysis problems. I propose a new 3D medial model which can be efficiently applied to complex shapes. The proposed medial model closely approximates the medial geometry along medial edge curves and medial branching curves by soft-penalty optimization and local correction. I further develop a scheme to perform model-based segmentation using a statistical medial model which incorporates prior shape and appearance information. The proposed medial models are applied to a series of image analysis tasks. The 2D medial

model is applied to the corpus callosum which results in an improved alignment of the patterns of commissural connectivity compared to a volumetric registration method. The 3D medial model is used to describe the myocardium of the left and right ventricles, which provides detailed thickness maps characterizing different disease states. The model-based myocardium segmentation scheme is tested in a heterogeneous adult MRI dataset. Our segmentation experiments demonstrate that the statistical medial model can accurately segment the ventricular myocardium and provide useful parameters to characterize heart function.

Contents

Acknowledgements	ii
1 Introduction	1
1.1 Motivation	1
1.1.1 Medial Model of Object Geometry	1
1.1.2 Geometric Model of the Heart	4
1.2 Contributions	6
1.3 Chapter Overview	8
2 Background	9
2.1 Statistical Shape Models and Image Segmentation	9
2.1.1 Shape Representation Methods	9
2.1.2 Model-Based Image Segmentation using the PDM	11
2.2 Medial Geometry and Medial Models	18
2.2.1 Basics of Medial Geometry	19
2.2.2 Inverse-Skeletonization and Medial Constraints	22
2.2.3 M-REP Approach	24
2.2.4 Implicit Domain Approach for CM-REP	25
2.2.5 PDE-Based Approach for CM-REP	26
2.2.6 Control Curve Approach for CM-REP	27

3	An Efficient CM-REP for 2D Geometric Objects	29
3.1	Introduction	30
3.1.1	Diffusion tensor imaging	31
3.1.2	Significance of Corpus Callosum in Neuroscience	31
3.1.3	Alternatives to Whole-Brain Normalization in Neuroimaging	32
3.2	Methods	33
3.2.1	2D Inverse-Skeletonization Problem and ODE-Based Approach	33
3.2.2	Solution for ODE in 2D Via Green’s Function	34
3.2.3	Closed Form Solution via Pythagorean Hodograph Curves	36
3.2.4	Model Fitting and Smoothed Local Symmetries	38
3.2.5	Shape-Based Normalization	40
3.2.6	Application and Validation of the Normalization	41
3.3	Results	46
3.3.1	Subjects and Data Acquisition	46
3.3.2	Cm-Rep Fitting Accuracy Analysis	47
3.3.3	Validation of the Closed Form Solution	48
3.3.4	Matching of the Connectivity Labels	49
3.3.5	Statistics on Tract FA Maps	53
3.4	Discussion	54
4	A New Branching Medial Model for 3D Geometric Objects	57
4.1	Introduction	57
4.2	Methods	59
4.2.1	Soft Penalty Terms	60
4.2.2	Deformable Model Fitting	61
4.2.3	Local Correction	62
4.2.4	Bi-Ventricular Medial Template	63
4.2.5	Implementation Details For The Medial Model	64
4.2.6	Cluster-Based Comparison Between Subject Groups	66

4.3	Results	67
4.3.1	Materials	67
4.3.2	Branching Topology	68
4.3.3	Fitting Accuracy	69
4.3.4	Groupwise Comparison of the Thickness and Thickening Maps	69
4.4	Discussion and Conclusion	77
5	Model-Based Segmentation using Statistical Medial Model	79
5.1	Introduction	80
5.2	Shape Priors	82
5.3	Appearance Model and Boundary Detection	83
5.3.1	AdaBoost Training and Classification	84
5.3.2	Features of AdaBoost	88
5.4	Segmentation Algorithm	89
5.5	Experiments	91
5.5.1	Data Set	91
5.5.2	Experimental Design	92
5.5.3	Initialization Error Tests	92
5.5.4	Boundary Delineation	94
5.5.5	Thickness Measurements	95
5.5.6	Left Ventricular Volume	95
5.5.7	Right Ventricular Volume	96
5.6	Discussion	97
5.6.1	Compare with Literatures	97
5.6.2	On the Establishment of Model Correspondence	98
5.6.3	Limitations and Future Work	99
5.7	Conclusion	100

6	Conclusions	101
6.1	Summary of Contributions	101
6.2	Discussion and Future Work	105
	References	106

List of Tables

3.1	Comparison of deformable registration based normalization and <i>cm-rep</i> based normalization for matching the connectivity label of each lobe in 30 subjects from a DS22q11.2 study. The quality of label matching is quantified using Dice similarity coefficients between pairs of subjects. Statistics are carried out to measure the significance of the differences between normalization methods. Results are listed for tracking setting 1 (FACT, FA threshold 0.25 and curvature threshold 60 degrees). The max p-values over all 8 tracking settings are also listed.	51
4.1	The results of fitting branching medial model to 428 cardiac segmentations.	69
4.2	Table enumerating clusters of significant differences in thickness and thickening between different pairs of subject groups, as defined in column 1. Column 1 also gives information of which group has a greater thickness/thickening for the particular cluster. Cluster mass is the integral of $ t $ over the cluster. Every cluster is defined as a connected region with a $p < p_0$. p_{corr} is the FWER-corrected p-value of the cluster.	77
5.1	Initialization error tests. The errors (\pm standard deviation) are point-to-mesh distances with the manual segmentation meshes. Here LV/RV indicate the endocardial surface of the left/right ventricle, while EPI means the epicardial surface of both left and right ventricles.	93

5.2	The mean point to mesh errors (\pm standard deviation) between the manual segmentation meshes and model-based segmentation meshes based on cross-validation. Here LV/RV indicate the endocardial surface of the left-/right ventricle, while EPI means the epicardial surface of both left and right ventricles.	94
5.3	Error of the heart wall thickness estimation in medial models fitted directly to MRI images comparing with medial models fitted to manual segmentations.	95
5.4	The mean left ventricular volume (\pm standard deviation) through manual measurement and model-based estimation, as well as the mean accuracy of model-based estimation (\pm standard deviation)	96
5.5	Errors (\pm standard deviation if applicable) reported in the literature for MR image segmentation.	98

List of Figures

1.1	An illustration of three-dimensional m-rep figure organized as a 3×3 quadrilateral mesh of medial atoms. The atom in the middle of the mesh is a regular medial atom, the rest are end atoms.	3
2.1	Examples of the medial axes for 2D and 3D objects.	19
2.2	(a) Example of <i>maximal inscribed balls (MIBs)</i> for a 2D object. The color of the MIBs identified the type of points on the medial axis associated with those MIBs: pink MIBs (A_1^2 points) are tangent to the boundary at two points, green MIBs (A_3 points) are tangent to the boundary at one point; and yellow MIBs (A_1^3 points) are tangent to boundary at three points. (b) Illustration of medial geometry in 2D. \mathbf{m} is defined as the center of the MIB. \mathbf{b}^\pm are the corresponding boundary points. $\vec{\mathbf{N}}_{\mathbf{m}}$ is the unit normal vector of the medial curve at point \mathbf{m} . $\vec{\mathbf{U}}^\pm$ are unit length vectors called “spokes”, which are orthogonal to the object boundary at \mathbf{b}^\pm	22
3.1	Example of two T1-weighted images with large anatomical differences. There is a topological difference, both in 3D and in the midsagittal section, in the connectivity between the fornix and the corpus callosum. Such differences pose a challenge to whole-brain registration methods.	33

3.2	Illustration of medial geometry in 2D. (a) Blum skeleton \mathbf{m} is defined as the center of the maximal inscribed disk (MID), with “spokes” goes from the \mathbf{m} to \mathbf{b}^\pm (b) SLS $\hat{\mathbf{m}}$ is defined as the center of the “chord” which connects the two MID tangency points \mathbf{b}^\pm on the boundary.	39
3.3	The grid lines of the two different parametrizations are shown, the zoomed sections show the details near the right endpoints. Note that the grid lines for Blum-skeleton-based parametrization are getting more and more sparse when approaching the endpoint, while the grid lines for SLS-based parametrization remain dense.	41
3.4	Examples of warped labeled atlas in the space of T1-weighted image (top row) and labeled fibers (bottom row). The left ones are axial view, and the right ones are sagittal view. The colors are: red for frontal lobe, blue for parietal lobe, yellow for temporal lobe and purple for occipital lobe.) . .	45
3.5	An illustration of 2D diffeomorphic registration, (a) is a single subject, (c) is the template constructed from the population of 30 corpora callosa, and (b) and (d) are the results after registering (a) and (c) diffeomorphically and symmetrically.	46
3.6	Illustration of fitted cm-reps overlaid on the binary images of corpora callosa, with Dice coefficients given on the top. The boundary of the fitted cm-reps are outlined in dark blue. The red lines are PISA medial curves. The thin, light blue curves indicate the grid lines of PISA reference frame. Example (a) Dice coefficient is the highest among all 30 subjects, and example (b) Dice coefficient is the lowest.	48

3.7	The convergence of the Voronoi skeleton of the <i>cm-rep</i> boundary to the <i>cm-rep</i> medial curve, over increasing sample density. The number of sample points on the <i>cm-rep</i> boundary is plotted on the horizontal axis, and the distance from the discrete Voronoi skeleton to the continuous <i>cm-rep</i> medial curve is plotted on the vertical axis. Both the mean distance and the maximum distance are plotted. The values are averages over 30 <i>cm-rep</i> models.	49
3.8	Example of connectivity labeling on MSCC. The left and right figures are for FACT and VINT tracking method respectively, with FA threshold 0.25 and curvature threshold 60 degrees. A number of voxels have a clear label, which means that the tractography could not trace a streamline passing through that voxel with both ends close enough to the same cortical regions in the left and right hemispheres.	50
3.9	The mean connectivity map rendered on the <i>cm-rep</i> coordinate system. The left and right figures are for FACT and VINT tracking method respectively, with FA threshold 0.25 and curvature threshold 60 degrees.	51
3.10	The mean connectivity map obtained by the <i>cm-rep</i> approach rendered on mean MSCC shape. The left and right figures are for FACT and VINT tracking method respectively, with FA threshold 0.25 and the curvature threshold 60 degrees.	52
3.11	Illustration of the Jacobian determinant maps inside the MSCC for one subject. On the left is the result for <i>cm-rep</i> mapping, on the right is the result for deformable registration. The color coded Jacobian determinant maps are plotted on the top. The histograms of the Jacobian determinant maps are plotted on the bottom.	52
3.12	An example of the tract-wise mean FA map for one subject.	53

3.13 Areas showing significant differences for tract FA maps between the control and DS22q11.2 groups, shown as colored overlays on the mean MSCC shape. The left and right images are results for FACT and VINT fiber tracking method respectively, with FA threshold 0.25 and curvature threshold 60 degrees. Results obtained by cm-rep based normalization and permutation based clustered pixel analysis. The adjusted p-values for colored regions are below the 0.05 threshold. 54

3.14 This figure illustrates the differences of summarized tract FA on PISA skeleton between the control group and DS22q11.2 group. Different tracking methods are used for producing figures on left and right, both with FA threshold 0.25 and curvature threshold 60 degrees. FACT is used for the images on the left, and VINT is used for the images on the right. Figures on the top shows the mean tract FA map of each groups after collapsing onto the PISA skeleton. The blue curves are for control group and red curves are for DS22q11.2 group. Figures on the bottom are the plot of $-\text{Log}(\text{adjusted p-values})$ for multiple statistical tests on the difference between the two groups. The p-values are corrected for multiple comparison using step down permutation. The blue line is the significant threshold corresponding to adjusted-p=0.05. 55

- 4.1 This figure illustrates the result of the deformable model with soft penalties and the effect of local correction. The left column shows the results after deformable fitting with soft penalties. The right column shows the results after local correction. The top row is part of the model boundary, note that before the correction, there are very tiny seams on the boundary, indicated by the arrows, which disappears after the correction. The bottom row shows part of the spoke vector field. Note that before the correction, the 6 spokes for the point on medial seam do not match perfectly into 3, but have very small discrepancy within each pair (one red and one blue as a pair), while after the correction only 3 spokes can be observed. 63
- 4.2 Medial template building and deformable model initialization pipeline. First: the boundary of the binrized volumetric template constructed by iterative unbiased averaging algorithm. Second: the pruned Voronoi Skeleton; note that it still has some small branches and the mesh is dense. Third: the medial template constructed under manual control. Fourth: example of a deformed medial template as the initialization for one cardiac shape. 65
- 4.3 Illustration of the medial template. The top row and bottom row are shown from different viewpoints. The medial surfaces are shown as colored meshes with the color indicating different branches of the medial model. There are three different branches: the *blue* surface models the left ventricular posterior wall; the *green* surface models the interventricular septal wall; and the *red* surface models the right ventricular wall. The curve where these three different colored surfaces join together is the branching curve, which is marked using *yellow* color on the left figure where the medial surfaces are rendered as transparent meshes. The boundary surfaces are shown as *white transparent* meshes on the right figure. 68

4.4	Examples of medial models fitted to binary segmentations of 2-chamber heart shapes. For each heart shape, shown are the medial manifold colored by the radius function R , the model boundary generated by inverse skeletonization, and the boundary of the segmentation to which the medial model was fitted.	70
4.5	Illustration of distance (mm) between the boundary of the target shape and the fitted medial model. The left figure overlays the model boundary, which is shown as white wireframe, on the binary segmentation boundary, which is shown as green surfaces. The middle figure is the distance map from the target to the model. And the right figure is the distance map from the model to the target.	71
4.6	Average pointwise distance (mm) from the model boundary to the target for all 428 cardiac shapes.	71
4.7	The mean thickness (left) and thickening (right) map for 28 healthy hearts in our data set.	72
4.8	The abnormal thickness (left) and thickening (right) regions for a patient are depicted with contours on the difference maps of the normal group mean and this patient (patient minus the average of normal group). . . .	73
4.9	Thickness differences between the healthy heart group (28 subjects) and the acute myocardial infarction group (38 subjects). The left column shows the average group difference (healthy group minus AMI group) whereas the right column shows the corresponding t-statistic map. Significant clusters of group difference are depicted with contours on the t-maps, and are also listed in Table 4.2. Different rows are shown from different viewpoints.	74

4.10 Thickness differences between the healthy heart group (28 subjects) and the hypertrophic cardiomyopathy group (7 subjects). The left column shows the average group difference (healthy group minus HCM group) whereas the right column shows the corresponding t-statistic map. Significant clusters of group difference are depicted with contours on the t-maps, and are also listed in Table 4.2. Different rows are shown from different viewpoints.	75
--	----

4.11 Systolic thickening differences between the healthy heart group (28 subjects) and the acute myocardial infarction group (38 subjects). The left column shows the average group difference (healthy group minus AMI group) whereas the right column shows the corresponding t-statistic map. Significant clusters of group difference are depicted with contours on the t-maps, and are also listed in Table 4.2. Different rows are shown from different viewpoints.	76
---	----

5.1 Illustration of appearance matching using the AdaBoost classifier. (a). The classifier is trained to differentiate between boundary nodes located at the correct anatomical boundary and displaced boundary nodes. In the figure, the yellow bars show samples drawn from correct anatomical boundary, while the red bars are samples that are displaced. During training, each boundary node is displaced along the *chord direction* (illustrated in Figure 5.2), and samples from the image neighborhood are used to generate appearance features. Combining features from different subjects, at each boundary node, I train an AdaBoost classifier with two classes (displaced node vs. not displaced). (b). The deformable model is shown in red color while the underlying object is shown in green color. During segmentation, the classifier is used to position boundary nodes close to anatomical boundaries. Pairs of boundary nodes that share a medial pseudo-landmark are displaced along the chord direction, governed by the AdaBoost classifiers corresponding to the nodes. Following these displacements, the deformable model is updated so as to satisfy the necessary geometric constraints and to abide by the shape priors. 85

5.2 Illustration of chord direction. For boundary nodes \mathbf{b}^{\pm} which correspond to the medial pseudo-landmark \mathbf{m} , the chord direction which crosses \mathbf{b}^{+} and \mathbf{b}^{-} shown as purple line in the figure. 86

5.3	Illustration of training exemplars of a “well-placed” boundary node (class 0) and a “misplaced” boundary node (class 1) in AdaBoost training. The manual segmentation of the anatomical structure is shown in gray. The medial model is fitted to the manual segmentation to obtain medial pseudo-landmarks and corresponding boundary points. The left figure shows a “well-placed” boundary node centered at the exact boundary of the manual segmentation. Note that since the manual segmentation can not be perfect, I actually place three “well-placed” boundary nodes for each boundary location: one is on the exact boundary of the manual segmentation as illustrated in the left figure, the other two are on two sides of the first one and are obtained by applying a small displacement to it along the chord direction. The right figure shows a “misplaced” boundary nodes, which is obtained by applying displacements to the well-placed boundary nodes along chord direction.	87
5.4	Example of automatic segmentation in a single subject. The top row shows the manual segmentation in green and the model initialized by landmarks in blue. The bottom row shows the segmentation result in red, with manual segmentation in green. From left to right, slices progress from most basal slice to the apex.	90
5.5	Illustrate the mean segmentation error. The meshes are colored by the mean point-to-surface distance from the model boundary mesh to the manual segmentation boundary mesh. The left figures show the endocardial boundary of the left and right ventricles. The right figures show the epicardial boundary of the left and right ventricles. The top row and bottom row are figures from different view point.	91
5.6	Bland-Altman plot for LVV comparing the manual measurement and model-based measurement.	96

5.7	Bland-Altman plot for RVV comparing the manual measurement and model-based measurement.	97
-----	---	----

Chapter 1

Introduction

1.1 Motivation

Medical imaging technologies are providing physicians and researchers with images of increasing spatial and temporal resolution. With the large amount of data being generated, there has been increased interest in automatic image analysis tools which can help physicians and researchers answer critical questions in morphology, physiology, and pathology studies. In many applications, an accurate, informative and consistent description of an object’s shape is particularly useful. For example, shape information can help characterize disease. It can also be learned, and prior knowledge of shape variability can aid automatic segmentation of the object in a new medical image. The work in this thesis develops a shape representation method called the medial model, which naturally expresses intuitive and descriptive global shape features like “thickening”, “bending”, “twisting” and “elongation”. This model is evaluated in a variety of image analysis tasks, with a focus on cardiac images.

1.1.1 Medial Model of Object Geometry

The medial model represents an object by its medial axis (skeleton). Informally, the skeleton is the set of curves in 2D, or surfaces in 3D, that results from thinning an object by

moving each of the boundary points inwards along the normal vector. Since the seminal paper by (Blum, 1967), medial axis geometry has been studied extensively (Damon, 2005; Giblin and Kimia, 2003; Choi et al., 1997; Bruce et al., 1985). The interest in medial axes arises from their ability to provide a rich and intuitive description of an object’s shape. The branching properties of the medial axis can be used to examine the hierarchical composition of an object into simple sub-shapes. The curvature of the curves forming the medial axis describes how the object bends locally. Each point on the medial axis is associated with a circle in 2D (or sphere in 3D) that lies inside the object and is tangent to the object’s boundary, usually at two points. This circle/sphere is the *maximal inscribed ball* of the object. The radii/diameters of these *maximal inscribed balls* describe the thickness of the object, a feature that is particularly relevant when studying heart pathology (Azhari et al., 1990; Sheehan et al., 1986) or neurodegeneration (Thompson et al., 2003; Bouix et al., 2005).

There are numerous deterministic algorithms that can compute the medial axis given the boundary of an object (Bouix et al., 2005; Kimia et al., 1995; Ogniewicz and Kübler, 1995; Näf et al., 1996; Siddiqi et al., 1999). However, given a set of similar objects (e.g., some anatomical structure taken across a set of subjects), deterministic methods cannot guarantee that the extracted medial axes will have the same number or configuration of branches. This makes it difficult, if not impossible, to construct a statistical shape model.

The medial representation (m-rep) developed by Pizer et al. (Pizer et al., 1999, 2003; Joshi et al., 2002) provides consistent medial features for statistical analysis. In this approach, a deformable template, defined in terms of its medial axis, is fitted to objects under constraints that prevent changes in the number and configuration of medial branches. As illustrated in Figure 1.1, an m-rep is an inherently discrete representation that uses sparsely sampled primitives called *medial atoms* as the building blocks of the model. Although interpolation methods for discrete m-reps have been proposed (Thall, 2004; Han et al., 2006), the exact medial geometric relations are not explicitly satisfied by the interpolated primitives.

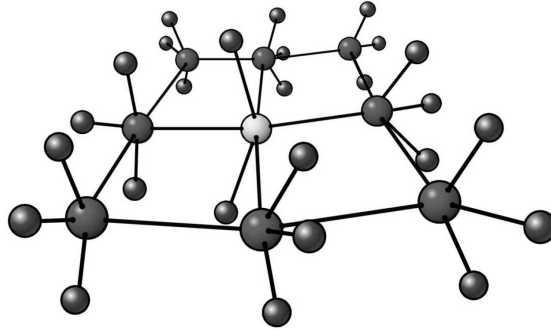


Figure 1.1: An illustration of three-dimensional m-rep figure organized as a 3×3 quadrilateral mesh of medial atoms. The atom in the middle of the mesh is a regular medial atom, the rest are end atoms.

The continuous version of m-rep (cm-rep) has been proposed (Yushkevich et al., 2003). In the cm-rep approach (Yushkevich et al., 2003, 2006b; Terriberry, 2006; Yushkevich, 2008), an object is modeled by first defining a *synthetic medial axis* as a collection of continuous manifolds, and then deriving the boundary of the model using *inverse skeletonization*, which achieves the inverse effect of the thinning process (also called skeletonization). However, because of the nature of medial geometry, inverse skeletonization is well-posed only if the synthetic medial axis satisfies a set of constraints, which include non-linear equality constraints that have to hold along the edge curves (or in 2D, end-points) or branching curves (or in 2D, branching-points) of the synthetic medial axis. In (Yushkevich et al., 2006b; Yushkevich, 2008), the constraints are satisfied by defining the synthetic medial axis as the solution of a partial differential equation (PDE) with boundary conditions equivalent to the equality constraints. In (Terriberry and Gerig, 2006; Terriberry, 2006), Terriberry and Gerig proposed another way to handle the constraints by using Catmull-Clark subdivision surfaces to model the medial axis and enforcing the constraints by locally modifying the medial axis at edge and branching curves to use interpolating splines. However, until now the applications of the cm-rep have been limited to simple shapes, whose medial axes consist of a single 3D surface.

In this thesis, I further develop the medial model methodologies used for applications

in biomedical imaging. In Chapter 3, I work out the explicit closed form solution of the ordinary differential equation (ODE) which is a 2D equivalent of the PDE used in (Yushkevich et al., 2006b). In Chapter 4, I propose a new way to construct the medial model by enforcing the medial model constraints using soft penalty terms and local corrections in the deformable model, which can be efficiently applied to a 3D complex shape whose medial axis has branches. In Chapter 5, based on the medial model proposed in Chapter 4, I develop a statistical medial model which incorporates both shape and appearance priors, and I use this model for image segmentation.

1.1.2 Geometric Model of the Heart

In cardiac studies, geometric models can help automate the extraction of clinically relevant parameters and provide better visualization. Simple geometric models, such as assuming that the left ventricle (LV) is ellipsoidal in shape, are traditional methods to obtain LV parameters from echocardiography and angiocardiography. In fact, simple assumptions are sometimes quite elegant and some of them are still actively in use, as shown in the standard scheme to divide the LV into sixteen segments in a polar plot (equal height and equal angle division). Another example is the method developed by (Germano et al., 1995) for automatic quantification of LV function from gated-perfusion single photon emission computed tomography (SPECT) images, which also uses the ellipsoidal model and can accurately determine most of the classical cardiac functional parameters.

In the last few decades, along with the rapid development of cardiac imaging technology, many advanced geometric models have been developed and applied to analyze cardiac shapes. For example, researchers have utilized superquadrics (Barr, 1981; Chen et al., 1995), Fourier functions (Staib and Duncan, 1996), 3D/4D harmonic descriptions (Matheny and Goldgof, 1995), B-Splines (Gustavsson et al., 1993) and polyhedral meshes (Gopal et al., 1992) to represent the LV boundaries using continuous functions; utilized dense point distributions (Assen et al., 2006; Shi et al., 2000; Peters et al., 2009) to discretely represent heart boundaries, and also utilized level sets (Yezzi et al., 1997) and

neural networks (Tseng et al., 1998) to implicitly represent the heart boundaries. Volumetric and deformation models (Frangi et al., 2002; Tustison and Amini, 2006; Mansi et al., 2009; Peyrat et al., 2008) are also quite popular, especially for the analysis of tagged MRI. (Frangi et al., 2001a) give a thorough review for the geometric models being used in cardiac applications.

The heart walls are thin, sheet-like structures which can be readily described by their medial axes. And there have been some efforts to use the medial axis in cardiac analysis. (Cauvin et al., 1993) proposed representing the LV by fitting a “truncated bullet” model to its skeleton. (Scellier et al., 1996) also leveraged the skeleton in the segmentation and quantification scheme for myocardial SPECT. The 2D “centerline method” (Sheehan et al., 1986) based on skeletons of 2D cardiac slices is widely used for measuring heart wall thickness, and it has been extended to 3D by Bolson and Sheehan (Bolson and Sheehan, 1993). However, statistical medial models that represent the heart using a medial axis with a consistent branching configuration and describe data-driven shape variations have not yet been constructed for the heart.

In this thesis, I construct statistical medial models for walls of the left and right ventricles and use these models in two important applications: heart wall thickness analysis in Chapter 4 and myocardium segmentation in Chapter 5.

The first application of the medial model is to provide a detailed wall thickness map of the left and right ventricles. The value of heart wall thickness and systolic thickening (the changing ratio of thickness during a cardiac cycle) in characterizing myocardial function has long been recognized (Azhari et al., 1990). The thickness or thickening can change in response to a number of stimuli, such as exercise, high blood pressure, myocardial ischemia and oxygen shortage. The change can be either localized or uniformly distributed, depending on the cause. A detailed map describing the thickness and thickening in the normal state and their changes in different disease states can provide valuable information from clinical, prognostic and therapeutic points of view. However, the way

that *thickness* is defined and computed varies considerably (Frangi et al., 2001a). Manual measurements are frequently used in clinical studies. Approximate approaches, such as dividing the myocardium into small cuboid elements and computing the ratio between volume and surface area, have also been used (Azhari et al., 1990). A widely accepted way to define thickness is based on the medial axis, from which a point-wise local thickness map can be derived. The 2D “centerline method” (Sheehan et al., 1986) and its 3D version “centersurface method” (Bolson and Sheehan, 1993) are widely used. However, the centersurface method only deals with a single heart chamber. In addition, the detailed thickness maps generated from different objects are not aligned, which poses problems for population comparison. In Chapter 4, I apply the branching medial model to generate aligned detailed thickness and thickening maps, and compare these maps across different heart conditions.

Segmentation of the heart is frequently required to quantitatively assess global or local functional parameters of the heart, such as the ejection fraction (EF) and heart wall thickness and thickening. A large number of cardiac segmentation studies are conducted using statistical boundary models, such as (Lotjonen et al., 2004; Assen et al., 2006; Lorenz and von Berg, 2006; Zheng et al., 2008; Wierzbicki et al., 2008; Peters et al., 2009). But segmentation of the heart using a statistical medial model has not been reported. In this thesis, I use a statistical medial model which has an explicit thickness shape prior to segment the bi-ventricular myocardium.

1.2 Contributions

The overall goal of this thesis is to further develop the medial modeling technique, making it easily applicable for 3D complex shapes and demonstrating its properties through these applications. Towards this goal, I claim the following contributions:

1. New method: Constructing a 2D cm-rep by obtaining the explicit closed-form solution of the ODE, which is a 2D equivalent of the PDE used in (Yushkevich et al.,

2006b).

2. Application: Being the first to use the medial model to perform shape-based normalization of the corpus callosum and to demonstrate potential advantages over a registration-based approach.
3. New method: Constructing a 3D branching medial model by enforcing the equality medial constraints using soft penalty terms and local corrections in the deformable model.
4. Application: Using the 3D branching medial model to represent the left and right ventricular myocardium, which yields aligned thickness and thickening maps.
5. New method: Constructing a statistical medial model comprising a shape prior of the medial manifolds using principal component analysis (PCA), a shape prior of the radial thickness field using Markov random field (MRF), and an appearance prior of the image features around the model boundaries using the Adaptive Boosting (Adaboost) algorithm.
6. Application: Being the first to apply the statistical medial model to cardiac image segmentation and show that it can segment the left and right ventricular myocardium accurately.

These contributions highlight the development of the medial modeling approach in terms of both methodology and application. The methodology developments include new methods to construct the medial model for both 2D objects with simple shapes and 3D objects with complex shapes. The applications demonstrate three usages of the medial model: providing shape-based normalization for different instances of an anatomical structure prior to comparison, providing meaningful shape features for disease characterization, and providing model-based segmentation. The constructed medial model, which describes intuitive shape features, can effectively represent shapes of biological objects and help to answer critical questions in morphology, physiology, and pathology studies.

1.3 Chapter Overview

The thesis is organized into six chapters:

Chapter 2 presents the background information on the related methodology. It reviews the statistical shape models and their applications to image segmentation. Medial geometry and the existing medial model approaches are also introduced in detail.

Chapter 3 analyzes the unique properties of the 2D equivalent of the PDE-based cm-rep method (Yushkevich et al., 2006b) and derives the solution to the ODE as a closed-form expression. This enables efficient generation of the cm-rep for 2D objects. The model is applied to the corpus callosum to examine the ability of the medial model to provide shape-based correspondence that matches different instances of anatomical structures. Such shape-based correspondence is evaluated and compared with a correspondence based on a volumetric registration in a DTI connectivity study for chromosome 22q11.2 deletion syndrome.

Chapter 4 presents a novel branching medial model for 3D objects. The model is generated and evaluated in a large cardiac MRI dataset, which demonstrates the robustness of the method. The ability of the medial model to provide descriptive shape features, particularly the *thickness measure*, is also demonstrated in the chapter. The thickness and thickening of different clinical groups are compared with those of the healthy group through statistical analysis.

Chapter 5 proposes a heart segmentation scheme that uses the statistical medial model. The segmentation scheme uses prior knowledge which is learned based on medial shape features. Learning-based classifiers for boundary detection are trained on appearance features which are sampled according to the medial model. The proposed scheme is evaluated on two clinical datasets, and the results demonstrate the accuracy and robustness of the method.

Chapter 6 concludes the thesis by summarizing the work in the thesis and discussing future work.

Chapter 2

Background

In this chapter, I first review general shape representation methods and their usage in model-based segmentation. Then I focus on the continuous medial representation (cm-rep), a particular type of shape representation method, and introduce its geometric background and the current approaches to constructing it.

2.1 Statistical Shape Models and Image Segmentation

This section begins with a brief summary of various shape representation methods. Then I review one of the most important applications of shape models: model-based image segmentation. Specifically, I focus on the cardiac image segmentation that is closely related to the thesis work in Chapter 5.

2.1.1 Shape Representation Methods

In order to study shapes using statistical methods, one must represent each shape with a fixed number of homologous measurements. A variety of shape representations have been described in the literature. This section briefly describes some approaches besides medial modeling.

Representing a shape using a set of points sampled from the boundary surface, as employed by (Cootes et al., 1995; Dryden and Mardia, 1998; Bookstein, 1989), has been extensively used in computer vision and medical image analysis. These points are commonly referred as *landmarks*. (Dryden and Mardia, 1998) define three types of landmarks: *anatomical landmarks* that are points of special biological or structural significance, *mathematical landmarks* that are points with unique geometric properties (such as singularity or critical points), and *pseudo-landmarks* that are points whose positions are derived from the positions of other landmarks. There are representations using a sparse set of landmarks, such as (Bookstein, 1989) which uses interpolation to reconstruct the geometrical form of objects between the landmarks. The point distribution model (PDM) is constructed using the coordinates of a dense set of boundary landmarks. In the popular active shape model (ASM) (Cootes et al., 1995) and active appearance model (AAM) (Cootes et al., 2001), the PDM is used as a part of a combined model that describes both shape and appearance features. These types of combined shape and appearance models can serve as the prior knowledge of anatomical structures and are widely used for automatic cardiac segmentation (Lotjonen et al., 2004; Assen et al., 2006; Lorenz and von Berg, 2006; Zheng et al., 2008; Wierzbicki et al., 2008; Peters et al., 2009).

Instead of using discrete points to represent boundaries of objects, another class of geometric models uses continuous functions to approximate the boundaries. For example, the boundary can be decomposed into a set of Fourier (Staib and Duncan, 1992) or spherical harmonic (Brechtbühler et al., 1995) basis functions, and the coefficients can be used as shape features. These kinds of basis decomposition representations are well adapted to a coarse-to-fine shape representation framework (Staib and Duncan, 1992). They have also been employed in deformable models for image segmentation (Kelemen et al., 1999; Székely et al., 1996), among which there is cardiac image segmentation (Staib and Duncan, 1996).

The above methods represent a shape by explicitly describing the boundary. An alternative approach is to represent the boundary implicitly, such as with the level set approach,

which embeds the boundary of the object as the zero level set of a high-dimensional function (Sethian, 1996). The level set representation has the ability to handle changes in topology. As a numerical technique that can follow the evolution of interfaces, it is widely used to achieve image segmentation (Caselles et al., 1995; Malladi and Sethian, 1995; Li et al., 2007). The level-set representation has also been used in statistical shape modeling for prior-based heart segmentation (Tsai et al., 2003).

In shape characterization based on volumetric registrations (Davatzikos et al., 1995; Christensen et al., 1997; Joshi, 1997; Csernansky et al., 1998; Zhuang et al., 2008), the shape difference between two objects is measured by the magnitude of deformation needed to optimally warp one object to the other based on maximizing the image similarity. To regularize the deformation, the deformation field needs to adhere to certain constraints, such as rules of elastic deformations or diffeomorphic mapping. When combined with a labeled atlas, volumetric registration can also be used to achieve heart segmentation (Zhuang et al., 2008).

2.1.2 Model-Based Image Segmentation using the PDM

Model-based image segmentation is usually much more robust than low-level algorithms since the model contains expected shape and appearance information. Among all shape representation methods used to construct statistical shape models to achieve image segmentation, the PDM is frequently used, especially given the popularity gained by the ASM and AAM. Additionally, our statistical medial modeling approach in Chapter 5 is more analogous to the ASM. Therefore, in this subsection, I focus on the model-based image segmentation using the PDM. Below, I review the key components for these approaches.

Statistical Shape Model Construction

Before constructing the statistical model, corresponding boundary landmarks need to be aligned to remove the similarity transformations between different shape instances. Generalized Procrustes analysis (Gower, 1975) and tangent space scaling (Dryden and Mardia, 1998) are frequently used for this purpose.

We assume each shape in the training sample is now represented by an aligned fixed-length shape feature \mathbf{x}_i (for the boundary landmark system, \mathbf{x}_i would consist of all the coordinates of landmarks). Constructing a statistical shape model basically consists of extracting the mean shape and modes of variation. Until now, the most often used approach in statistical shape model is principal component analysis (PCA), although many techniques (Hyvärinen and Oja, 2000; Twining and Taylor, 2001; De La Torre and Black, 2003; Fletcher and Joshi, 2004; Stegmann et al., 2006; Sjöstrand et al., 2007) have been proposed either to improve or to replace it.

In the PCA approach, given s shape samples, the mean shape is just a direct average

$$\bar{\mathbf{x}} = \frac{1}{s} \sum_{i=1}^s \mathbf{x}_i \quad (2.1)$$

The corresponding covariance matrix is

$$S = \frac{1}{s-1} \sum_{i=1}^s (\mathbf{x}_i - \bar{\mathbf{x}})(\mathbf{x}_i - \bar{\mathbf{x}})^T \quad (2.2)$$

Then, using eigendecomposition or singular value decomposition (SVD) methods, the eigenvectors \mathbf{v}_j and eigenvalues λ_j can be calculated. \mathbf{v}_j are the modes of shape variations, and λ_j measures the respective variances. Now, we can approximate a valid shape that has the same shape variation with the training data by a linear combination of the modes:

$$\mathbf{x} = \bar{\mathbf{x}} + \sum_{j=1}^c b_j \mathbf{v}_j, \quad (2.3)$$

where b_j are the shape parameters that quantify the variation. Therefore, they need to be limited to a certain interval. A common approach is to constrain each b_j to lie inside $[-3\lambda_j, 3\lambda_j]$. Alternatively b_j can be constrained by $(\sum_{j=1}^c \frac{b_j^2}{\lambda_j}) < M$, where M is a

threshold chosen from the χ^2 distribution. Other methods to constrain b_j include utilizing Gaussian mixture models (Cootes and Taylor, 1997) or multi-dimensional tables that are constructed from the training data (Li and Ito, 2005).

c , which is the number of modes used in the statistical shape model, can be chosen according to the specific application. One popular way is to choose it so that the accumulated variance $\sum_{j=1}^c \lambda_j$ reaches a certain ratio (most often $0.9 - 0.99$) of the total variance.

Various techniques have been proposed to improve or replace PCA. Robust PCA is proposed in (De La Torre and Black, 2003) to ensure that the computation of PCA modes is less susceptible to outliers. The PCA modes generally do not have sparse structure, meaning the modes would influence all shape features simultaneously. Since sparsity is usually desired, a number of techniques have been proposed to introduce sparse modes, such as the Orthomax rotation (Stegmann et al., 2006) and sparse PCA (Sjöstrand et al., 2007). Independent component analysis (ICA) (Hyvärinen and Oja, 2000) is proposed to separate independent components linearly mixed in the data without assuming the orthogonality of the components. (Fletcher and Joshi, 2004) introduced principal geodesic analysis (PGA) for models where the features are parameterized on a curved Riemannian manifold rather than in an Euclidean space. Kernel PCA (Twining and Taylor, 2001) has been proposed to perform a nonlinear form of PCA efficiently using techniques of kernel methods, in which data points are implicitly mapped to a high-dimensional Euclidean feature space.

Establishment and Evaluation of Model Correspondence

The construction of the statistical shape model for a population requires the extraction of corresponding measurements from objects. The method for defining correspondence can vary according to the shape representation method. In the context of landmark descriptions, the problem would be finding a set of landmark points, sometimes also called “pseudo-landmarks”, that are consistent across a population of objects. In early research, those points were obtained by first manually identifying the anatomical landmarks and

then constructing new points via interpolation. However, this is not only labor-intensive but also limited by the inherent sparsity of available anatomical landmarks, especially for 3D shape characterization. Therefore, fully automatic pseudo-landmark selection, which involves identifying corresponding locations across a population of objects, has been widely explored.

Establishing landmark correspondence can be viewed as a shape registration problem that can be categorized by the type of data representation. First, correspondence can be computed through *mesh-to-mesh registration*. Well-established algorithms, such as the iterative closest point (ICP) algorithm by (Besl and Mckay, 1992) and the softassign procrustes by (Rangarajan et al., 1997), can match two meshes with potentially different numbers of vertices using a similarity transform. Non-rigid registration of meshes has also been used (Subsol et al., 1998). Yet another approach has been proposed to identify corresponding parts/points on meshes using classifiers (Pitiot et al., 2007). Second, correspondence can be computed through *mesh-to-volume registration*, that is, adapting a deformable surface model to the segmented binary volumes and defining the correspondences by the vertex locations of the deformable template after the surface evolution has converged. This is the approach adopted in (Kaus et al., 2003; Zhao and Teoh, 2008; Lorenz and von Berg, 2006). A third way to compute correspondence is to register a volumetric atlas and using the resulting deformation field to propagate the landmarks placed on the atlas to the training data (Frangi et al., 2001b), which can be categorized as establishing correspondence through *volume-to-volume registration*. Finally, it is possible to establish correspondence through *parameterization-to-parameterization registration*. For 2D curves, this is often equivalent to uniform arc-length correspondence (Brechtbühler et al., 1995). In 3D, it would be much more complex, and different approaches have been proposed, such as using spherical harmonics (SPHARM) (Kelemen et al., 1999) or other methods to parameterize or to re-parameterize the objects possibly regularized by a limited set of known/assumed correspondences (Thompson et al., 1996).

The approaches described above register a pair of shapes at a time. However, it is hard

to define a general rule of “good correspondence” that can be effectively applied to pairwise registration. (Kotcheff and Taylor, 1998) proposed to determine the correspondence through the population-wise optimization which minimizes the determinant of the covariance matrix (DetCov) to favor a compact statistical model. Based on the DetCov approach, (Davies et al., 2002) proposed the minimum description length (MDL) method. It searches for the correspondence that allows the PDM to be expressed using the shortest possible message. The objective function directly relates to having as much variability as possible occur in the first few principal components while keeping the variability in the remaining components on the order of imaging noise. Following the MDL method, approaches have been proposed to simplify the computation of the objective function (Thodberg, 2003) and its gradient (Ericsson and Astrom, 2003) for the MDL method which helps to speed up the computation.

The evaluation of the correspondence is not easy since the true correspondences of biological shapes are generally not known. (Davies, 2002; Styner et al., 2003c) proposed a method to measure the goodness of a correspondence using three qualities of the PCA model built based on it: generalization ability, specificity, and compactness. The generalization ability is the capability to describe shape outside of the training set, which can be quantified by the approximation error when the PCA model is used to fit an unseen shape example in leave-one-out experiments. Compactness is the ability to use a minimal set of parameters to capture the shape variation within a population, which can be quantified by the cumulative variance in the PCA model. Specificity is the ability to represent only valid shapes, which can be quantified by the similarity between examples generated by the PCA model and their nearest neighborhood in the training set. (Styner et al., 2003c) employed these three measures to compare models built by manually initialized subdivision surfaces, SPHARM parameterization, DetCov, and MDL using lateral brain ventricle and femoral head data and reported that DetCov and MDL give the best results.

Appearance Model

In order to automatically fit the statistical shape model to unseen image data to achieve segmentation, an appearance model is needed. Depending on the way that the appearance features are sampled in the model, appearance models can be divided into two categories: boundary-based sampling and region-based sampling.

A representative of boundary-based sampling methods is the ASM (Cootes et al., 1995), where appearance features are sampled along the direction perpendicular to the model boundary. In the original version of the ASM (Cootes et al., 1995), appearance features are modeled using PCA, extracting a mean feature vector and principal modes of variations for each landmark. Later, the ASM was adapted to various segmentation tasks in the biomedical image field, during which different appearance features have been explored, and different ways for constructing the appearance model out of the features have been proposed. Commonly used appearance features include image intensity values, their derivatives, Haar wavelets, Gabor wavelets (Daugman, 1988; McKenna et al., 1997), and steerable features (Freeman and Adelson, 1991). During the model-based segmentation, ASM searches along the directions perpendicular to the boundary to locate new boundary landmarks. This is usually achieved by evaluating a designed match function that is supposed to achieve maximum at the boundary. The match function can be Mahalanobis distance, a gradient-based edge detector, a k-nearest-neighbor (kNN) classifier (de Bruijne et al., 2003), or other discriminative training-based classifiers (Zheng et al., 2008). Depending on the application, appearance features may or may not vary significantly over the model boundary. Therefore, some choose to train a different appearance model at each landmark point (Zheng et al., 2008; Peters et al., 2009), while others may cluster the landmarks into regions of similar appearance according to the feature vectors (Brejl and Sonka, 2000) to obtain more training data.

A popular method using region-based sampling is the AAM (Cootes et al., 2001), which samples the entire interior region of the model to build a feature vector. To obtain the feature vectors for different shapes, the regions need to be normalized first, which is

usually achieved by transforming each shape into the mean shape. Then, PCA is applied to build a combined shape and appearance model. Examples of using AAM in cardiac image segmentation are (Mitchell et al., 2002; Lapp et al., 2004).

Search Algorithms to Achieve Segmentation

The segmentation is achieved by matching the statistical shape model to new image data. This is naturally formulated as a Bayesian posterior probability estimation problem. The Bayesian probability states that, given some data and some hypothesis, the posterior probability that the hypothesis is true is proportional to the product of the likelihood multiplied by the prior probability. Let H be a model (hypothesis) and D be the image data, we have

$$P(H|D) = \frac{P(D|H)P(H)}{P(D)}. \quad (2.4)$$

Here $P(H)$ is the *prior probability* of H : the probability that H is correct before the data D was seen. $P(H)$ is derived from the statistical model constructed from training data. $P(D|H)$ is the *conditional probability* of seeing the data D given that the hypothesis H is true, which can be measured by the match between D and H . $P(D)$ is the marginal probability of D , which is a constant during the model fitting since the data is fixed. $P(H|D)$ is the *posterior probability*: the probability that the model is true, given the data and the prior knowledge about the model. Locating the model in new image data thus can be formulated as maximizing the posterior probability defined in (2.4) by altering the parameters that define the model. However, it is usually inefficient to solve this optimization directly, given the large size of the search space. Instead, various search algorithms are formulated to match an initial estimate of the model to image data. Below I summarize the classical ASM and AAM approach.

In the ASM, an instance of the shape model \mathbf{x} in an image is defined by a similarity transform T and the shape parameters \mathbf{b} according to

$$\mathbf{x} = T(\bar{\mathbf{x}} + \Phi\mathbf{b}). \quad (2.5)$$

Starting from an initial model state, the ASM searches new position for each landmark by evaluating the fit of the appearance model at different positions along the normal vector to the boundary surface. This gives a vector of new landmark candidates $\tilde{\mathbf{x}}$. Now the pose difference between the current state of the model \mathbf{x} and the new candidate $\tilde{\mathbf{x}}$ is eliminated by a similarity alignment, leading to a new similarity transform \tilde{T} . Assume that the current model \mathbf{x} is brought to \mathbf{y} by the new similarity transform, the new shape parameters can be computed by

$$\tilde{\mathbf{b}} = \mathbf{b} + \Phi^T \tilde{T}^{-1}(\tilde{\mathbf{x}} - \mathbf{y}).$$

After constraining $\tilde{\mathbf{b}}$ to lie within appropriate parameter limits as described in Section 2.1.2, we have an updated valid instance of the model. The above steps are conducted iteratively, until a specified convergence criterion is hit, e.g. the maximum or average landmark movement is below a given threshold.

The AAM by (Cootes et al., 2001) features an unique search algorithm during the model-based segmentation. Since AAM stores the complete appearance of the object, it can synthesize realistic appearance of the modeled data. AAM assumes a constant linear relationship between appearance residuals and parameter updates. This relationship is learned using the training images. Then, during the segmentation, AAM updates the parameters in each step by computing a synthesized appearance, comparing with the real appearance features to calculate the appearance residual, and obtaining the updates using the learned linear relationship.

2.2 Medial Geometry and Medial Models

This section provides the reader with necessary backgrounds on the Blum medial axis and introduces medial modeling techniques.

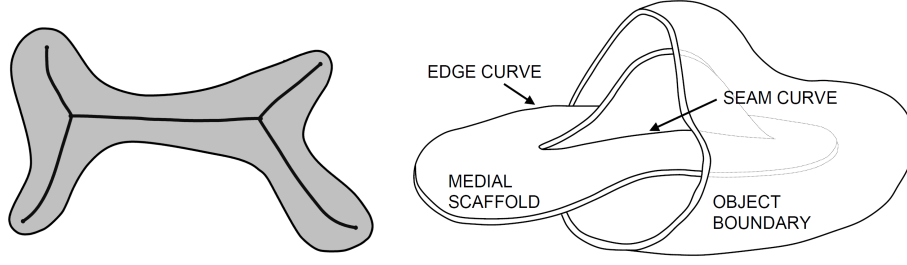


Figure 2.1: Examples of the medial axes for 2D and 3D objects.

2.2.1 Basics of Medial Geometry

I first briefly introduce the terminology and concepts of medial geometry. There is more than one way to define the Blum medial axis of an object: as the shock set of the Eikonal PDE, or, as I do below, as the locus formed by maximal inscribed balls. Given a geometric object \mathcal{O} in \mathbb{R}^3 , I define a *maximal inscribed ball (MIB)* in \mathcal{O} as any ball \mathcal{B} satisfying $\mathcal{B} \subseteq \mathcal{O}$ and for which there exists no ball $\mathcal{B}' \neq \mathcal{B}$ such that $\mathcal{B} \subset \mathcal{B}' \subseteq \mathcal{O}$. The locus of the centers and radii of all MIBs is called the *medial axis* of the object. The medial axis is thus composed of two components: the locus of the centers of all MIBs in \mathbb{R}^3 denoted by \mathbf{m} , and the locus of radii in \mathbb{R}^+ denoted by R . In the literature, \mathbf{m} is also sometimes called *medial surfaces*, *medial scaffold*, *centersurface*, *skeleton*, or even *medial axis* with the (\mathbf{m}, R) being called *augmented Blum medial axis*. Examples of the medial surfaces are illustrated in Fig 2.1.

The medial scaffold is a *Whitney stratified set* (Damon, 2005), that is, a collection of manifolds with boundaries that are connected along edges. These manifolds will be referred to as *medial manifolds*. The parts of their boundaries that are shared by multiple *medial manifolds* will be called *medial seams* or *branch curves*, while the parts of the boundaries that only belong to one medial manifold will be called *medial edges*.

Here I adopt the notation of (Giblin and Kimia, 2000) to classify the type of points that form the medial scaffold according to the order and multiplicity of tangency between their MIBs and the boundary of the object. Each point is assigned a label of the form A_k^m , where

m indicates the number of unique points at which the maximal inscribed ball is tangent to the boundary, and k indicates the order of tangency between the maximal inscribed ball and the boundary. There are only two possible orders of tangency contact of a maximal inscribed ball \mathcal{B} at a point P on the boundary surface S :

- A_1 contact: \mathcal{B} is tangent to S at P ;
- A_3 contact: \mathcal{B} is tangent to S at P . The radius of \mathcal{B} is one of the principal radii of curvature of S at P , and the corresponding principal curvature is a local extremum (P is also called a ridge point of S).

For other orders of contact of a ball at a boundary point, the boundary must penetrate the surface of the ball. Therefore the ball can never be maximally inscribed.

(Giblin and Kimia, 2000) proved that for 3D objects, there are five types of generic points that form the medial scaffold. They are the following:

1. A_1^2 points on the interior of medial manifolds, where the MIB is tangent to the object's boundary at two points; these points form two-dimensional manifolds;
2. A_3 points on medial edges, where the MIB is tangent to the boundary at one point; these points form one-dimensional manifolds;
3. A_1^3 points on medial seams, where the MIB is tangent to the boundary at three points with first-order contact with the boundary; these points form one-dimensional manifolds;
4. $A_1 A_3$ points at medial seam-edge intersections; these points form zero-dimensional manifolds;
5. A_1^4 points at medial seam-seam intersections; these points form zero-dimensional manifolds.

For 2D objects, there are three types of generic points that form medial curves, which are:

1. A_1^2 interior points of the medial curves, where the MIB is tangent to the object's boundary at two points; these points form one-dimensional manifolds;
2. A_3 edge points, where the MIB is tangent to the boundary at one point; these points form zero-dimensional manifolds;
3. A_1^3 branching points, where the MIB is tangent to the boundary at three points with first-order contact with the boundary; these points form zero-dimensional manifolds.

The composition of the medial scaffold into interconnected *medial manifolds* makes it possible to decompose geometrically complex objects into simple components called *figures*, which are the union of closed balls whose centers and radii form a single *medial manifold* in the medial axis of an object.

Given a parameterized medial axis $(\mathbf{m}(u, v), R(u, v))$, spheres (or disks) of radius $R(u, v)$ are placed at each location $\mathbf{m}(u, v)$ on the medial manifold, and the generated boundary is the envelope of such a family of spheres or disks. In 3D, the points \mathbf{x} that belong to this two-parameter family of spheres are defined by the implicit equation:

$$f(\mathbf{x}, u, v) = |\mathbf{x} - \mathbf{m}(u, v)|^2 - R(u, v)^2 = 0. \quad (2.6)$$

Thus, any point \mathbf{x} on the boundary of an object must satisfy the following envelope equations:

$$f = 0, \quad \frac{\partial f}{\partial u} = 0, \quad \frac{\partial f}{\partial v} = 0. \quad (2.7)$$

By solving these equations, we can derive two boundary points \mathbf{b}^+ and \mathbf{b}^- for each point \mathbf{m} on a medial manifold, where the MIB is tangent to the object boundary for this *figure*.

$$\mathbf{b}^\pm = \mathbf{m} + R \vec{\mathbf{U}}^\pm \quad (2.8)$$

$$\vec{\mathbf{U}}^\pm = -\nabla_{\mathbf{m}} R \pm \sqrt{1 - \|\nabla_{\mathbf{m}} R\|^2} \vec{\mathbf{N}}_{\mathbf{m}}, \quad (2.9)$$

where $\vec{\mathbf{N}}_{\mathbf{m}}$ is the unit normal vector of the medial manifold at point \mathbf{m} , $\vec{\mathbf{U}}^\pm$ are unit length vectors orthogonal to ∂O at \mathbf{b}^\pm , and $\nabla_{\mathbf{m}}$ is the Riemannian gradient of R on the medial manifold. The vectors $R \cdot \vec{\mathbf{U}}^\pm$, that is, the vectors pointing from the center of an MIB

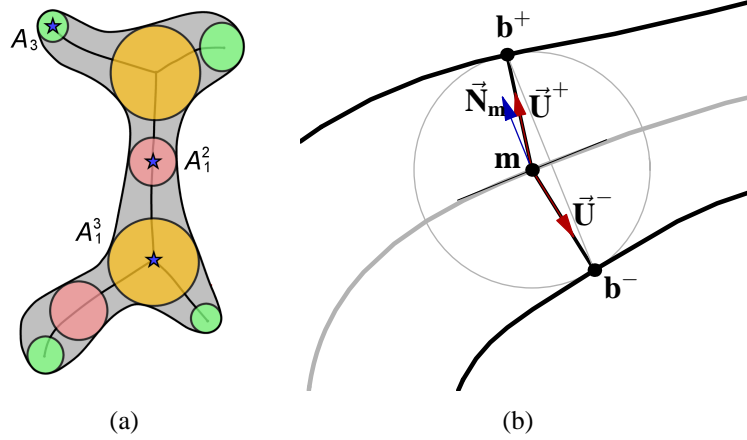


Figure 2.2: (a) Example of *maximal inscribed balls (MIBs)* for a 2D object. The color of the MIBs identified the type of points on the medial axis associated with those MIBs: pink MIBs (A_1^2 points) are tangent to the boundary at two points, green MIBs (A_3 points) are tangent to the boundary at one point; and yellow MIBs (A_1^3 points) are tangent to boundary at three points. (b) Illustration of medial geometry in 2D. \mathbf{m} is defined as the center of the MIB. \mathbf{b}^\pm are the corresponding boundary points. \vec{N}_m is the unit normal vector of the medial curve at point \mathbf{m} . \vec{U}^\pm are unit length vectors called “spokes”, which are orthogonal to the object boundary at \mathbf{b}^\pm .

to the corresponding boundary tangency points, are called *spokes*. The local geometry is illustrated in 2D by Fig 2.2.

2.2.2 Inverse-Skeletonization and Medial Constraints

The cm-rep approach leverages the idea of *inverse skeletonization* (Yushkevich et al., 2006b), where the skeleton (medial axis) of the model is defined first, and the model’s boundary is derived analytically from the skeleton by Eq (2.8). Because the topology and configuration of the skeleton (commonly referred to as *branching topology*) are pre-defined, this approach guarantees the consistency of the skeleton within a cohort, which makes population studies possible. The key difficulty lies in the well-posedness of the inverse skeletonization problem. That is, given arbitrary connected surface patches \mathbf{m} and arbitrary positive field R , the $\{\mathbf{m}, R\}$ pair may not form the skeleton of any object. Rather,

inverse skeletonization is only possible for the $\{\mathbf{m}, R\}$ pairs that satisfy a set of constraints enforced by the medial geometry. The medial constraints fall into two classes. The first class ensures that the boundary generated by the medial axis is closed and connected. The second class ensures that the boundary is nonsingular.

According to Eq. 2.8, one medial surface will generate two boundary surface patches. Therefore if all the boundary patches are to meet seamlessly to form the boundary of an object, different constraints are needed for points on different positions of the medial manifolds.

Near a medial edge, the two spokes will get closer and closer to each other, collapsing to a single vector once the medial edge is reached, so the two boundary patches generated by the medial surface close. The corresponding equality constraint is:

$$\|\nabla_{\mathbf{m}} R\| = 1. \quad (2.10)$$

Points on the medial seam belong to three medial manifolds \mathbf{m}_i $\{i = 1, 2, 3\}$. For these points, the six spokes belonging to three medial manifolds pair up in such a way that $\vec{\mathbf{U}}_{\mathbf{m}_i}^+$ and $\vec{\mathbf{U}}_{\mathbf{m}_{i\oplus 1}}^-$ (\oplus denotes additional modulo 3) get closer, and eventually pairs of spokes collapse to three vectors. This ensures that different boundary patches generated from the three medial manifolds come together to form the boundary of an object. These constraints can be written as follows:

$$\nabla_{\mathbf{m}_{i\oplus 2}} R - \nabla_{\mathbf{m}_{i\oplus 1}} R = \sqrt{1 - \|\nabla_{\mathbf{m}_i} R\|^2} \vec{\mathbf{N}}_{\mathbf{m}_i}. \quad (2.11)$$

At the seam-edge intersection, $\|\nabla_{\mathbf{m}_i} R\| = 1$ for the medial manifold whose edge is crossing the intersection, and the other two manifolds will have angle π (actually, they merge into one manifold at the intersection point).

For the interior points of the medial manifolds, the two boundary patches should stay disjointed, and the inequality constraint $\|\nabla_{\mathbf{m}} R\| < 1$ should hold.

The above constraints ensure that the boundary is closed and connected. However, it is still possible for the boundary to form singularities. First, R needs to be constrained to

be always positive:

$$R > 0 \quad (2.12)$$

The Jacobian constraint

$$J^\pm = \pm \left(\frac{\partial \mathbf{b}^\pm}{\partial u} \times \frac{\partial \mathbf{b}^\pm}{\partial v} \cdot \vec{\mathbf{U}}^\pm \right) / \left(\frac{\partial \mathbf{m}}{\partial u} \times \frac{\partial \mathbf{m}}{\partial v} \cdot \vec{\mathbf{N}} \right) > 0 \quad (2.13)$$

prevents the swallowtail singularity on the boundary patch.

The Jacobian constraint can prevent local crosses of the boundaries. However, it is still possible for a global intersection to occur. For example, a global intersection can occur when one end of an object wraps around and enters another end. These are difficult to describe mathematically. Fortunately, for most objects, they are relatively easy to avoid during modeling, especially when geometric priors exist.

As can be seen from Equations (2.10) and (2.11), the equality constraints need to be satisfied along curves (medial seams and medial edges), which have an infinite number of points, while a cm-rep model can only have a finite number of coefficients, making the model severely over constrained. This is the most challenging problem for constructing a cm-rep model, and various solutions have been proposed, which are described in the following subsections.

2.2.3 M-REP Approach

(Pizer et al., 1999) introduced the m-rep approach which was later extended to 3D (Pizer et al., 2001; Joshi et al., 2002). The m-rep uses sparsely sampled primitives called *medial atoms* as the building blocks of the model. A basic medial atom is a tuple $m = \{x, r, U^1, U^2\}$, where x is a point on the medial scaffold; r is the radius of the MIB at x ; and U^1, U^2 are the unit spoke vectors pointing towards the boundary points (Fletcher et al., 2004). Another way to define a medial atom is to use a tuple $m = \{x, r, \mathbf{R}, \theta\}$, where x and r are still the center and radius of the MIB; \mathbf{R} is the orientation which can be expressed as an orthogonal frame $\{b, n, t\}$ placed at x to define the bisector $b = \frac{U^1 + U^2}{\|U^1 + U^2\|}$, the unit normal vector n of the medial manifold, and $t = b \times n$; and θ is the angle between

the spoke vector and the bisector b . Both tuples contain sufficient information to reconstruct two points on the boundary per medial atom. And one can easily convert between the two representations of the medial atom.

A special class of medial atoms is used to model the locally cylindrical geometry of nearly-tubular 3D objects such as blood vessels. These atoms can be imagined as a regular medial atom that is spinning around the bisector b . In (Aylward and Bullitt, 2002), such medial atoms are used to model vessel trees.

Another special class of medial atoms is used around medial edge curves. The *end atom* contains one extra parameter, an elongation factor η , which is used to add a third boundary point $x + r\eta b$. Therefore an end atom does not try to represent a precise A_3 medial point on a medial edge curve, but rather describes a whole section of the object in the neighborhood of the A_3 point. In such representation, the end of a figure is approximated by an oval arc (2D) or a locus of such arcs (3D).

(Han et al., 2004, 2005) proposed a multi-figure m-rep that represents each part of a complex object using single-figure m-rep, and then uses surface blending to attach a child single-figure m-rep to its parent. Each figure is an array of medial atoms. This type of model is very useful when complex objects have a parent-child organization of parts (like the hand, with a palm and five fingers). It uses a membrane-like connection between parts instead of following the Blum’s medial geometry.

The medial atoms are typically sampled on a coarse mesh. Therefore the constructed boundary nodes need to be interpolated to produce a finer sampling or a continuous description of the boundary, which can be achieved using subdivision surfaces (Thall, 2002).

2.2.4 Implicit Domain Approach for CM-REP

The first cm-rep approach is proposed in (Yushkevich et al., 2003), which deals with simple shapes whose medial axes consist of a single medial manifold. In this approach, the boundary of the domain Ω of the medial manifold is defined implicitly. Specifically, the parametric manifold \mathbf{m} and the scalar field R are first defined in a large region Q , which has

the properties that $\|\nabla_{\mathbf{m}}R\| > 1$ on the boundary of Q while at the same time, $\|\nabla_{\mathbf{m}}R\| < 1$ somewhere inside Q . Then, the domain of the medial manifold is defined as the set

$$\Omega = \{\mathbf{u} \in Q : \|\nabla_{\mathbf{m}}R(\mathbf{u})\| \leq 1\}.$$

By construction, the equality constraint (2.10) holds on $\partial\Omega$. Although this approach makes it possible to represent medial manifolds and deform them by adjusting the values of basis function coefficients, it has shortcomings in the context of deformable modeling and statistical analysis. It is difficult to prevent Ω from changing topology during deformation, and, since Ω changes as the model deforms, models of different instances of the same anatomical structure are defined on different domains, making it difficult to establish correspondences.

2.2.5 PDE-Based Approach for CM-REP

To overcome the above mentioned shortcomings in (Yushkevich et al., 2003), Yushkevich et al. later proposed a PDE-based approach (Yushkevich et al., 2006b; Yushkevich, 2008). The method in (Yushkevich et al., 2006b) only deals with simple shapes, but the improved version (Yushkevich, 2008) can deal with complex shapes whose medial axis consist of more than one medial manifold.

In (Yushkevich et al., 2006b), the equality constraint (2.10) can be satisfied if the radial field R is defined as a solution of a Poisson PDE with the boundary condition that incorporates (2.10). This PDE is expressed in terms of $\phi = R^2$ and has the following form:

$$\Delta_{\mathbf{m}}\phi = \rho, \text{ subject to: } \|\nabla_{\mathbf{m}}\phi\|^2 = 4\phi \text{ on } \partial\Omega, \quad (2.14)$$

where $\Omega \in \mathbb{R}^2$ is the domain on which the medial manifold \mathbf{m} is defined, $\Delta_{\mathbf{m}}$ denotes the Laplace-Beltrami operator on \mathbf{m} , and ρ is some smooth function defined on Ω . A 3D cm-rep model is formed by specifying the manifold, \mathbf{m} , and the field, ρ , and then solving the PDE to obtain the radial field R .

(Yushkevich, 2008) generalized the PDE approach to complex shapes by using a fourth-order biharmonic PDE. Let γ be the boundary of \mathbf{m} , γ_{edge} be the medial edge curve, and γ_{seam} be the medial seam curve. Let $\vec{T}_\gamma(s)$ be the unit tangent vector along γ and $\vec{\nu}_i(s)$ be the outward unit normal vector along $\gamma(s)$ for medial manifold \mathbf{m}_i ($i = 1, 2, 3$), i.e., $\vec{\nu}_i \perp \vec{\mathbf{N}}_{\mathbf{m}_i}$ and $\vec{\nu}_i \perp \vec{T}_\gamma$. Let τ be a one-dimensional scalar field on γ such that $\tau > 0$ and $d\tau/ds < 1$ everywhere on γ . Then $\phi = R^2$ satisfies

$$\Delta_{\mathbf{m}}^2 \phi = \rho, \quad (2.15)$$

$$\phi|_\gamma = \tau^2, \quad (2.16)$$

$$\phi, \vec{\nu}_i|_{\gamma_{\text{seam}}} = 2\tau \sqrt{1 - (d\tau/ds)^2} \vec{\nu}_i \oplus_1 \cdot \vec{\nu}_i \oplus_2, \quad (2.17)$$

$$\phi, \vec{\nu}_i|_{\gamma_{\text{edge}}} = -2\tau \sqrt{1 - (d\tau/ds)^2}. \quad (2.18)$$

The PDE-based approach requires solving a PDE each time the model coefficients are adjusted, which can be cumbersome for deformable modeling. It has been successfully applied to model 3D hippocampus (Yushkevich et al., 2006b; Yushkevich, 2008) and white matter tracts (Yushkevich et al., 2008) which have simple shapes. No application on complex shapes has been published.

In Chapter 3, I solve the corresponding ODE for 2D shapes, which allows for the efficient generation of cm-rep for 2D applications.

2.2.6 Control Curve Approach for CM-REP

Before (Yushkevich, 2008) was published, (Terriberry and Gerig, 2006; Terriberry, 2006) proposed the first solution to construct a 3D branching cm-rep using Catmull-Clark subdivision surfaces and “control curves”. Catmull-Clark subdivision surfaces are a generalization of B-spline knot insertion to meshes of arbitrary topology. To enforce the medial constraint (2.10), the medial surface \mathbf{m} is still normally interpolated using control points along the medial edges, but the radial scalar field R is interpolated using a control curve instead of a few isolated control points. Given \mathbf{m} and the derivative of R along the medial curve, the derivative of R along the normal direction to the medial curve can be solved to

satisfy the constraint (2.10), from which the control curve can be computed. This method also works for medial seams, along which the medial constraints (2.11) can be enforced by adjusting the radial scalar field R using control curves away from the seam-edge intersections. At seam-edge intersections, the adjustment involves both the control points and control curves.

This is the first published branching cm-rep approach. However, no application has yet been published for this method. One limitation of this approach is that it requires skeletons to be defined using Catmull-Clark subdivision surfaces with quadrilateral elements, which cannot handle corners on the edge due to the asymmetry of the interpolation, while the biharmonic PDE-based approach (Yushkevich, 2008) and the approach proposed in Chapter 4 are independent of the type of representation used to model the medial axis.

Chapter 3

An Efficient CM-REP for 2D Geometric Objects

In this chapter, the unique properties of the 2D equivalent of the PDE-based cm-rep method is examined and the solution to the ODE is formulated as a closed form expression by utilizing Pythagorean hodograph splines (Farouki and Sakkalis, 1990; Farouki and Neff, 1995). Then the ability of the medial model to match different instances of anatomical structures is explored. The medial model can extend boundary-based correspondences to the interiors of structures, providing a shape-based normalization to the texture information before further comparison can be conducted. This medial shape-based normalization is compared with the normalization provided by diffeomorphic registration algorithm and the experimental results are reported.

This chapter is based on a paper (Sun et al., 2007b) that was written together with Dr. Paul A. Yushkevich, Dr. Hui Zhang, Dr. Philip A. Cook, Jeffrey T. Duda and Dr. James C. Gee at University of Pennsylvania and Dr. Tony J. Simon at University of California-Davis. The coauthors' contributions were invaluable for the conception, implementation, and publication of the research described below. The comparison experiments were made possible thanks to Dr. Brian B. Avants, who generously provided the diffeomorphic registration algorithm.

3.1 Introduction

Geometric models are emerging as a powerful tool for analyzing multi-modality and multivariate imaging data. In today's imaging studies, it is not uncommon to collect T1- or T2-weighted, diffusion-weighted and functional MRI data in a single session. Group analysis of such rich datasets requires anatomical differences between individuals to be normalized. This is usually achieved by registration of structure weighted images to a common template (Friston et al., 1994; Miller et al., 2005). However, registration may not be the ideal normalization tool in cases where one is interested in analyzing data associated with a specific structure, especially in presence of irreconcilable anatomical differences in other structures present in the images. In these cases, geometric models can provide a basis for normalization, especially given the large body of research on correspondence methods for these models (Davies et al., 2002; Kotcheff and Taylor, 1997; Tagare et al., 1995). And the medial model is especially suitable for normalization of anatomical structures in multivariate datasets because of its ability to extend boundary-based correspondences to the interiors of structures.

Yushkevich et al. (Yushkevich et al., 2006b) have previously presented the PDE-based cm-rep approach for modeling 3D structures. However, some structures, such as the corpus callosum, lend themselves well to two-dimensional modeling. This chapter examines the unique properties of the 2D equivalent of the PDE-based cm-rep method. One contribution is to formulate the solution to the equivalent ordinary differential equation as a closed form expression by utilizing Pythagorean hodograph splines (Farouki and Sakkalis, 1990; Farouki and Neff, 1995). Another contribution is the study of the medial shape-based normalization of the corpus callosum, which is used to analyze patterns of commissural connectivity in the human brain as derived from diffusion tensor imaging. Shape-based normalization of the corpus callosum is compared to registration paradigms, with results favoring the shape-based approach.

3.1.1 Diffusion tensor imaging

Diffusion tensor imaging (DTI) (Basser et al., 1994) has a number of potential applications for the study of brain white matter. The anisotropy of water diffusion is sensitive to the tissue composition and organization: when the fibers are organized into bundles with similar orientation, the diffusion of water is hindered more across the fibers than along them. This anisotropy can be quantified in various ways within the diffusion tensor framework, the most widely used index is the fractional anisotropy (FA) (Basser and Pierpaoli, 1996), which we use in this work.

Tractography makes use of the directional information in the diffusion tensor to trace the path of white matter tracts. The tractography algorithms used in this paper belong to the family of streamline-based methods. In these methods, streamlines are derived by following the local fiber orientation, which is assumed to be the direction with the maximum apparent diffusion coefficient (the principal eigenvector of the diffusion tensor). Anatomical connectivity between voxels can then be inferred from the resulting streamlines. Several methods have been proposed for tracking the streamline paths, Mori and van Zijl (Mori and van Zijl, 2002) give a review.

3.1.2 Significance of Corpus Callosum in Neuroscience

The corpus callosum is the largest white matter structure in the brain, and it is of great interest in studies of brain connectivity. The shape and area of the midsagittal section of the corpus callosum (MSCC) have been analyzed in studies of sexual dimorphism (DeLacoste-Utamsing and Holloway, 1982; Witelson, 1989; Allen et al., 1991), schizophrenia (Foong et al., 2000; Woodruff et al., 1997; Jacobsen et al., 1997), autism (Just et al., 2006; Vidal et al., 2006; Piven et al., 1997) and many other studies. Differences in the size and area of the MSCC are hypothesized to relate to differences in interhemispheric connectivity. The advent of DTI has allowed a new way of analyzing connectivity differences in the brain, i.e., by estimating the location of major fiber tracts and examining anisotropy

in diffusion. However, since DTI does not provide a complete description of connectivity, it is natural to combine morphometric measurements of the MSCC with measurements derived from DTI in white matter studies. The cm-rep approach that we advocate in this paper allows precisely that: the analysis of features derived from DTI in the corpus callosum coordinate frame.

Medial modeling has been applied to the corpus callosum in earlier morphometric studies. Golland et al. (Golland et al., 1999) fitted a piecewise linear deformable model to a distance map to compare the medial axes of the MSCC between patients and controls. Yushkevich et al. (Yushkevich et al., 2001) used discrete m-reps to derive a set of morphometric features that are invariant under similarity transformations. However, there is no prior work on using continuous medial modeling in the MSCC or on using medial models to normalize the MSCC between subjects.

3.1.3 Alternatives to Whole-Brain Normalization in Neuroimaging

In multi-subject studies of functional MRI, DTI and other multivariate imaging data, normalization is typically achieved by registering subjects' anatomical images to a common template, and warping the multivariate data into the template's space. Such is the approach taken in SPM (Friston et al., 1994). In neuroimaging, whole-brain registration can lead to poor alignment of smaller structures, such as the hippocampus (Carmichael et al., 2005). This is especially true in the presence of large-scale anatomical differences, which are common in certain neurological conditions: Fig. 3.1 shows an example from a study of DS22q11.2 deletion syndrome (Emanuel et al., 2001), where the topology of the corpus callosum and fornix is different between two subjects. In studies interested in specific structures, some alternatives to whole-brain registration have been proposed. The ROI-AL method (Stark and Okado; Miller et al., 2005) applies registration to regions of interest, rather than whole brains, resulting in higher sensitivity of fMRI group analysis. However, concerns have been raised in the community that the correspondences computed by the registration within homogeneous structures are primarily driven by regularization priors

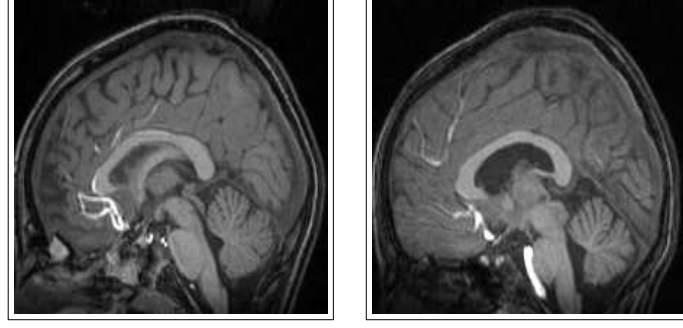


Figure 3.1: Example of two T1-weighted images with large anatomical differences. There is a topological difference, both in 3D and in the midsagittal section, in the connectivity between the fornix and the corpus callosum. Such differences pose a challenge to whole-brain registration methods.

that differ among algorithms (Rohlfing, 2006). From this perspective, normalization based on explicit geometric correspondences may be advantageous. As this paper shows, in the corpus callosum, shape-based normalization appears to align anatomically-defined corpus callosum sub-regions better than whole-brain and region-of-interest registration.

3.2 Methods

3.2.1 2D Inverse-Skeletonization Problem and ODE-Based Approach

In 2D, the boundary of a medial model can still be derived as

$$\mathbf{b}^\pm(t) = \mathbf{m}(t) + R(t) \vec{\mathbf{U}}^\pm(t) \quad (3.1)$$

where

$$\vec{\mathbf{U}}^\pm = -\frac{dR}{ds} \vec{\tau} \pm \sqrt{1 - \left| \frac{dR}{ds} \right|^2} \vec{\mathbf{N}}. \quad (3.2)$$

According to (Yushkevich et al., 2006b) which deals with 3D models, in order to ensure the validity of the Inverse-Skeletonization, the medial model should satisfy $\|\nabla_{\mathbf{m}} R\| = 1$, where $\nabla_{\mathbf{m}}$ is the Riemannian gradient on manifold \mathbf{m} , and in 2D it has the form

$$\left| \frac{dR}{ds} \right| = 1 \quad \text{for } t = 0, 1. \quad (3.3)$$

In 3D, this constraint can be satisfied if the radial field R is defined as a solution of a Poisson PDE with the boundary condition that incorporates the non-linear equality constraint. This PDE is expressed in terms of $\phi = R^2$ and has the following form:

$$\Delta_{\mathbf{m}}\phi = \rho, \quad \text{subject to: } \|\nabla_{\mathbf{m}}\phi\|^2 = 4\phi \text{ on } \partial\Omega, \quad (3.4)$$

where $\Omega \in \mathbb{R}^2$ is the domain on which the medial manifold \mathbf{m} is defined, $\Delta_{\mathbf{m}}$ denotes the Laplace-Beltrami operator on \mathbf{m} , and ρ is some smooth function defined on Ω . A 3D cm-rep model is formed by specifying the manifold, \mathbf{m} , and the field, ρ , and then solving the PDE to get the radial field R . Since \mathbf{m} and R satisfy the sufficient conditions of inverse skeletonization, the boundary of a cm-rep model can then be derived analytically.

An equivalent construction is possible in 2D. For a medial curve $\mathbf{m}(t) = \{x(t), y(t)\}$ with arc length $s(t)$ and $t \in [0, 1]$, the Poisson PDE simplifies to the following ODE:

$$\begin{aligned} \frac{d^2\phi}{ds^2} &= \rho(t); \\ \text{subject to: } \left(\frac{d\phi}{ds}\right)^2 &= 4\phi \text{ at } t = 0, 1. \end{aligned} \quad (3.5)$$

As described in (Yushkevich et al., 2006b), cm-rep models can be fitted to anatomical structures in a Bayesian framework by iteratively applying deformations to \mathbf{m} and ρ , deriving the radial field and the boundary, and comparing the cm-rep boundary to the boundary of the target object. However, this requires the PDE/ODE to be solved at every iteration of this optimization. In 3D, the PDE is solved numerically, which is costly and, due to the non-linear nature of the PDE, sensitive to initialization. However, in 2D, a closed-form expression for the solution of the ODE (3.5) can be derived, which will improve both the efficiency and accuracy. This derivation is described in the following two sections.

3.2.2 Solution for ODE in 2D Via Green's Function

First note that the ODE (3.5) has a non-linear boundary condition. That is, if ϕ_1 and ϕ_2 are the solutions of (3.5) for right hand sides ρ_1 and ρ_2 respectively, then $\phi_1 + \phi_2$ is not a

solution for the right hand side $\rho_1 + \rho_2$:

$$\begin{aligned} \frac{d^2(\phi_1 + \phi_2)}{ds^2} &= \rho_1(t) + \rho_2(t); \\ \text{but: } \left(\frac{d(\phi_1 + \phi_2)}{ds}\right)^2 &\neq 4(\phi_1 + \phi_2) \text{ at } t = 0, 1. \end{aligned} \quad (3.6)$$

Denoting $\sigma(t) \equiv \frac{ds}{dt}$, the ODE (3.5) can be expanded using the chain rule

$$\begin{aligned} \left(\frac{\phi'(t)}{\sigma(t)}\right)' &= \rho(t) \sigma(t); \\ \text{subject to: } (\phi'(t))^2 &= 4\sigma^2(t) \phi(t) \text{ at } t = 0, 1, \end{aligned} \quad (3.7)$$

which is a Sturm-Liouville equation with nonlinear boundary conditions. Its Green's function $G(t, u)$ satisfies the equation

$$\left(\frac{G'(t, u)}{\sigma(t)}\right)' = \delta(t - u), \quad (3.8)$$

and the solution can be expressed as

$$\phi(t) = \int_0^1 G(t, u) \rho(u) \sigma(u) du + h(t), \quad (3.9)$$

where $h(t)$ is the harmonic function satisfying $\frac{d^2 h}{ds^2} = 0$, i.e.,

$$h(t) = C_1 s(t) + C_2. \quad (3.10)$$

Here C_1 and C_2 are just constants.

Solving equation (3.8) by integration leads to the following solution

$$G(t, u) = H(t - u)[s(t) - s(u)], \quad (3.11)$$

where H denotes the Heaviside step function, i.e., $\partial H / \partial t = \delta(t)$.

Now, substitute (3.11) and (3.10) into solution (3.9) and use the boundary conditions of (3.7), and that determines C_1 and C_2 :

$$C_1 = \frac{4LP - 4Q - P^2}{2(P - 2L)} \quad (3.12)$$

$$C_2 = \frac{(4LP - 4Q - P^2)^2}{16(P - 2L)^2}. \quad (3.13)$$

Here $L = s(1)$ is the length of the medial curve, $P = \int_0^1 \rho(u)\sigma(u) du$, and $Q = \int_0^1 s(u)\rho(u)\sigma(u) du$. Now the solution of ODE (3.9) can be written as

$$\begin{aligned} \phi(t) = & s(t) \int_0^t \rho(u)\sigma(u) du - \\ & \int_0^t s(u)\rho(u)\sigma(u) du + C_1 s(t) + C_2 \end{aligned} \quad (3.14)$$

Since $s(t)$ is itself an integral of $\sigma(t)$, this solution for $\phi(t)$ involves a double integral:

$$\begin{aligned} \phi(t) = & \int_0^t \sigma(u) du \int_0^t \rho(u)\sigma(u) du - \\ & \int_0^t \int_0^u \sigma(w)\rho(u)\sigma(u) dw du + \end{aligned} \quad (3.15)$$

$$C_1 \int_0^t \sigma(u) du + C_2 \quad (3.16)$$

thus this solution does not have a closed form for arbitrary regular curves $x(t), y(t)$ and $\rho(t)$. In order to further simplify cm-rep modeling, we take advantage of Pythagorean hodograph (PH) curves (Farouki and Sakkalis, 1990; Farouki and Neff, 1995; Choi et al., 1999).

3.2.3 Closed Form Solution via Pythagorean Hodograph Curves

PH curves are polynomial parametric curves $\hat{\alpha}(t) = \{\hat{x}(t), \hat{y}(t)\}$ for which there exists a polynomial $\hat{\sigma}(t)$ such that

$$\hat{x}'^2(t) + \hat{y}'^2(t) \equiv \hat{\sigma}^2(t). \quad (3.17)$$

For PH curves, $\{\hat{x}', \hat{y}', \hat{\sigma}\}$ form a Pythagorean triple, so that not only $\hat{x}(t)$ and $\hat{y}(t)$, but also the arc length $\hat{s}(t)$ along the curve, can be expressed as a polynomial function.

In (Kubota, 1972), it is proved that PH curves must have the form

$$\begin{aligned} \hat{x}'(t) &= w(t)[p^2(t) - q^2(t)], \\ \hat{y}'(t) &= 2w(t)p(t)q(t), \\ \hat{\sigma}(t) &= w(t)[p^2(t) + q^2(t)], \end{aligned} \quad (3.18)$$

where $w(t)$, $p(t)$ and $q(t)$ are polynomial functions.

If we use a piecewise PH curve to define the medial curve $\mathbf{m}(t)$, and also define $\rho(t)$ as a piecewise polynomial function, then all functions in the ODE solution (3.16) are piecewise polynomial functions or integrals of piecewise polynomial functions, and a closed form of ϕ can be obtained with ease. We can also obtain $x(t)$ and $y(t)$ immediately if we are given the boundary condition $(x(0), y(0))$. In practice, we only need to manipulate the coefficients of those polynomial functions, which is extremely fast. However, if $w(t)$ crosses zero, the given $\{x(t), y(t)\}$ pair would fail to generate a regular curve because $\frac{ds}{dt}$ vanishes there. To avoid that, we can simply set $w(t) = 1$. At the same time, since we use piecewise curves, we can subdivide the whole curve into enough pieces to ensure that we have enough freedom to deform the curve for fitting the anatomical structure.

Examining (3.18) reveals that when $w(t) = 1$, the sign of the polynomial functions $p(t)$ and $q(t)$ can be simultaneously changed to get the same pair of $\{x(t), y(t)\}$. Confining the sign of $p(t)$ or $q(t)$ would guarantee the uniqueness of the solution. This could either be done as a constrained optimization, or, by simply checking and flipping the signs after the optimization.

A cm-rep in 2D can be completely defined by the coefficients of $p(t), q(t), \rho(t)$ and a translation term (x_0, y_0) as the following:

$$\{c_0^p, \dots, c_N^p, c_0^q, \dots, c_N^q, c_0^\rho, \dots, c_N^\rho, x_0, y_0\} \quad (3.19)$$

so that

$$\begin{aligned} p(t) &= \sum_{i=0}^N c_i^p B_{i,2}(t), \\ q(t) &= \sum_{i=0}^N c_i^q B_{i,2}(t), \\ \rho(t) &= \sum_{i=0}^N c_i^\rho B_{i,2}(t), \end{aligned} \quad (3.20)$$

where $B_{i,2}(t)$ is the uniform quadratic B-spline basis function.

In our current implementation, $p(t)$, $q(t)$ and $\rho(t)$ are approximated by uniform quadratic B-spline functions. The generated medial curves are piecewise 5th-order polynomial curves, while $\phi(t)$ are piecewise 12th-order polynomial functions, and overall both medial curves and $\phi(t)$ are C^2 .

3.2.4 Model Fitting and Smoothed Local Symmetries

The cm-rep model for a MSCC is constructed by fitting a deformable cm-rep template to a binary segmentation of the structure. The fitting approach is described in detail in (Yushkevich et al., 2006b) for 3D applications, and most of the aspects are identical in 2D.

A 2D cm-rep model is defined by a set of parameters listed in (3.19). By changing the values of these parameters, we can generate cm-rep models that have the same branching topology (i.e., single-curve medial axis) as the original model. To fit a cm-rep model to a binary segmentation of a structure, we minimize the overlap error between the model and the structure while also minimizing a set of prior terms, which incorporate inequality constraints required for inverse skeletonization. These constraints are described in (Yushkevich et al., 2006b). In this application the Conjugate Gradient Descent algorithm provided by GNU Scientific Library(GSL) (Galassi et al.) is used to solve the optimization problem. The objective function can be computed very efficiently because the computation of the cm-rep boundary is analytic, and the derivative of the overlap between a model and an image can be approximated by a boundary integral.

The initial template for the MSCC was constructed from cm-rep fitting results for a large MSCC dataset in a previous morphometry study (Sun et al., 2007a). This template is first aligned to the target structure by optimizing in the space of similarity transformations, and then the parameters defining the cm-rep model are optimized in a multi-resolution scheme. During the fitting, the number of coefficients for the cm-rep template is gradually increased, and at the same time, the standard deviation of the Gaussian kernel, which is used to smooth the binary image segmentation, is gradually decreased. For the uniform quadratic B-spline basis we use, there exists an efficient refinement scheme to increase the number of control points while holding the spline curves unchanged.

Closely related to the Blum skeleton is the *Smoothed Local Symmetries* (SLS) (Brady and Asada, 1984). While the Blum skeleton is formed by the centers of MIDs, SLS is formed by the midpoints of the chords connecting the points $(\mathbf{b}^+, \mathbf{b}^-)$, where the MID is

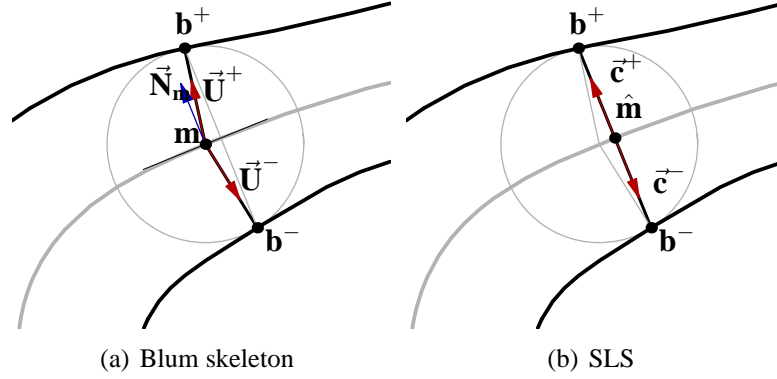


Figure 3.2: Illustration of medial geometry in 2D. (a) Blum skeleton \mathbf{m} is defined as the center of the maximal inscribed disk (MID), with “spokes” goes from the \mathbf{m} to \mathbf{b}^\pm (b) SLS $\hat{\mathbf{m}}$ is defined as the center of the “chord” which connects the two MID tangency points \mathbf{b}^\pm on the boundary.

tangent to the object’s boundary. An attractive property of the SLS axis is that its endpoints lie on the boundary of the object, as opposed to the Blum skeleton, whose endpoints of the axis lie some distance away from the boundary (the distance equals to the radius of the MIB at that endpoint).

The SLS axis, denoted $\hat{\mathbf{m}}$ is derived as:

$$\hat{\mathbf{m}}(t) = \mathbf{m}(t) - R(t) \frac{dR}{ds} \vec{\tau}. \quad (3.21)$$

Like the *spokes* in Blum skeleton, the *chords* in SLS also span the whole object interior, connecting the SLS skeleton with the object boundary. We use $h(\mathbf{t}) = \frac{1}{2} \|\mathbf{b}^+ - \mathbf{b}^-\|$ to denote the half length of the chord, and let $\vec{c}^\pm = \frac{1}{h}(\mathbf{b}^\pm - \hat{\mathbf{m}})$ denote the unit length vector pointing from $\hat{\mathbf{m}}$ to \mathbf{b}^\pm , as illustrated in Fig. 3.2.

After the cm-rep model is fitted, the SLS skeleton is derived and re-parameterized to establish correspondences between subjects. Here the equal arc length parameterization is used, i.e., we find a diffeomorphism $u : [0, 1] \rightarrow [0, 1]$ such that $s(u(t))$ is a linear function of t .

3.2.5 Shape-Based Normalization

In biomedical imaging applications, the need to factor out anatomical differences between individuals often arises in the context of multi-modal or multi-variate analysis. The problem of normalization can be stated in terms of parameterization: each point in each individual must be assigned a set of parameter values such that points that have the same parameter values across individuals are anatomically homologous. Normalization is often resolved by means of volumetric registration. However, most registration methods do not explicitly incorporate shape information. On the other hand, there are many techniques in the shape analysis field that establish shape-based correspondences between boundaries of structures. The cm-rep method has a unique property that allows boundary-based or skeleton-based correspondences to be propagated to the interiors of objects, thus enabling shape-based normalization.

Given a cm-rep model with a parametric expression of the Blum skeleton, the interior of the model can be parameterized by a shape-based coordinate system where one of the axes is the skeleton and the other goes along the spokes, i.e., is orthogonal to the model's boundary. This parameterization associates each point \mathbf{X} on the interior of the object \mathcal{O} with a pair of coordinates $t \in [0, 1]$ and $\xi \in [-1, 1]$ according to the mapping

$$\mathbf{X}(t, \xi) = \mathbf{m}(t) + |\xi|R(t)\vec{\mathbf{U}}^{sign(\xi)}. \quad (3.22)$$

Following the proof in (Yushkevich et al., 2006b), the mapping $\mathbf{X} : [0, 1] \times [-1, 1] \rightarrow \mathcal{O}$ is onto and “almost” one-to-one, with the exception occurring at $t = 0$ and $t = 1$, where $\mathbf{X}(t, \xi) = \mathbf{X}(t, -\xi)$. This coordinate system associates each point $\mathbf{X}(t, \xi)$ inside the object with the nearest boundary point $\mathbf{X}(t, sign(\xi))$ through the coordinate t , and indicates the point's relative position between the skeleton and the boundary through the coordinate ξ .

The SLS axis presents another way to parameterize the interiors of cm-rep models. Similarly to (3.22), we can define the map:

$$\hat{\mathbf{X}}(t, \xi) = \hat{\mathbf{m}}(t) + |\xi|h(t)\vec{\mathbf{c}}^{sign(\xi)}, \quad (3.23)$$

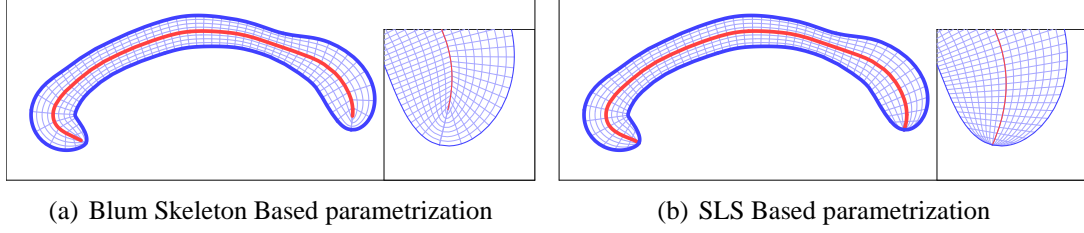


Figure 3.3: The grid lines of the two different parametrizations are shown, the zoomed sections show the details near the right endpoints. Note that the grid lines for Blum-skeleton-based parametrization are getting more and more sparse when approaching the endpoint, while the grid lines for SLS-based parametrization remain dense.

which associates each point $\hat{\mathbf{X}}(t, \xi)$ inside of the object with its corresponding boundary point $\hat{\mathbf{X}}(t, \text{sign}(\xi))$ and SLS skeleton point $\hat{\mathbf{X}}(t, 0)$ through coordinate t , and indicates the point's relative position between the SLS skeleton and boundary through the coordinate ξ .

Besides the parametrization defined by the map (3.22) or (3.23), which is onto and almost one-to-one (except the points with $t = \pm 1$), there also exists a homeomorphism from the cm-rep interior to the interior of an ellipse (Yushkevich et al., 2006b). As a consequence, one can construct a homeomorphism between any two objects with a single-curve medial axis.

The parametrization based on the Blum skeleton can propagate the correspondence along the directions orthogonal to the boundary but it is somewhat ill-behaved near the endpoints of the medial curve, because the Jacobian of the mapping $\mathbf{b}^\pm(\mathbf{m})$ goes to infinity there. This causes increasingly sparse sampling along the cm-rep boundary when approaching the endpoints, if we sample the medial curve uniformly. In contrast, the SLS skeleton, whose endpoints lie on the boundary, allows more uniform sampling of the points on the boundary near the endpoints. Fig. 3.3 shows the two different parametrizations and the details near endpoints. In this application the SLS-based normalization is adopted.

3.2.6 Application and Validation of the Normalization

Diffusion MRI studies provide an attractive framework within which to evaluate the performance of corpus callosum normalization via cm-reps and other techniques. In this

chapter, we compare cm-rep normalization to diffeomorphic registration. With the help of diffusion tensor tractography, every location in the corpus callosum can be associated with a set of features derived from fiber tracts passing through that location. In a multi-subject experiment, these features can be used to detect structural differences between control and DS22q11.2 cohorts. The effect of different normalization methods on the statistical significance of detected differences can then be analyzed. Furthermore, normalization methods can be evaluated by examining how well they align anatomically labeled fiber tracts within cohorts. The following sections describe the approaches used to evaluate normalization from these different standpoints.

Features Derived from Diffusion Tensor Tractography

Diffusion tensor tractography is a tool for studying the white-matter connectivity in the brain. We combine tractography and the cm-rep method to make a quantitative comparison of the white-matter microstructure along the fiber pathways passing through the MSCC. First, the midsagittal plane is identified automatically according to the symmetry of the left and right hemisphere and the MSCC is manually segmented in the midsagittal plane.

In our study two streamline tracking methods implemented in the open source Camino toolkit(Cook et al., 2006) are used. The FACT method proposed by Mori et al (Mori et al., 1999), follows the local fiber orientation in each voxel, changing direction at voxel boundaries. We also track using a fixed, sub-voxel step size, following interpolated orientations taken from the vector field at each step using a simple eight-neighbor trilinear interpolation. This is referred to as the VINT (vector interpolation) method.

Both of the tracking algorithms use an anisotropy threshold to terminate the tracking: when the streamline approaches a voxel where the FA falls below the threshold, the streamline is judged to have left white matter and tracking is terminated. A curvature threshold is also imposed: if the streamline path curves by too much over the length of a voxel, the tracking is stopped. Most white matter pathways have low curvature and thus high curvature is interpreted as a sign that the streamline is following an erroneous path.

The fiber pathways of the corpus callosum in each subject are segmented by seeding streamline tractography in every voxel in the diffusion-tensor image and retaining only streamlines that intersect the MSCC. Following a similar method to Corouge et al. (Corouge et al., 2006), we examine the fractional anisotropy (FA) of diffusion along the length of each streamline. The *tract FA* for a streamline is the mean FA along the whole streamline. The tract FA is plotted on the MSCC. The value of each voxel is the mean tract FA of all streamlines that pass through that voxel.

The shape-based normalization is applied to make an inter-subject comparison of the tract FA in MSCC. Permutation based cluster size inference (Hayasaka and Nichols, 2003) is performed with the null hypotheses of the zero difference on the tract FA between control group and DS22q11.2 group.

In addition, I show another advantage of the shape-based parametrization, which is to further reduce the dimensionality of the data by collapsing the tract FA value to the SLS skeleton. More specifically, at each point along the SLS skeleton, a medial tract FA is obtained as the average of all values along the “chord” centered at this point and connecting two corresponding boundary points. Multiple hypothesis testing is also performed with the null hypotheses of zero difference on the medial tract FA values between control group and DS22q11.2 group.

The fiber trajectories recovered by streamline tractography are dependent on the tracking algorithm and the thresholds used to terminate the tracking. In order to examine the stability of our comparisons with respect to the choice and the parameters of the diffusion tensor tractography algorithm, the tract FA comparisons are repeated using eight different sets of streamlines. The FA threshold is either 0.15 or 0.25, the curvature threshold allows a maximum curvature of either 45 or 60 degrees, and the local fiber direction is determined by either the FACT or VINT algorithm. With the interpolated algorithm, the step size is 0.4mm.

Corpus Callosum Connectivity Labeling

A qualitative examination of the cortical connectivity is complimentary to the quantitative tract-based measures. Following (Mori et al., 1999; Gee et al., 2005; Cook et al., 2005; Styner et al., 2005), the MSCCs are subdivided according to the cortical connectivity. To label the fiber trajectories, an anatomical atlas is used. It was constructed using a combination of manual, semiautomatic and automatic techniques (Yushkevich et al., 2005), and divides each hemisphere of the cerebral cortex into four regions: frontal, parietal, temporal and occipital. The atlas is aligned to the T1-weighted image of each subject using a diffeomorphic image registration algorithm (Avants and Gee, 2004). Examples of the warped atlas in space of the T1-weighted image are shown in Fig. 3.4. Then the warped atlas in the space of the T1-weighted image is further aligned to the space of the diffusion tensor image using the transformation that coregisters the T1-weighted image to the diffusion tensor image.

Now each fiber derived from tractography in the diffusion image space can be assigned a label according to the cortical region of its endpoints. However, given that the principal diffusion direction can not be reliably estimated using the principal eigenvector when FA is low, the derived tracts almost never reach the gray matter area. In practice, some tracts are much shorter and far away from any of the cortical regions. these fibers were filtered out in our algorithm by requiring that the end of the fibers should be at least within 15mm of one of the cortical regions. In addition, when a fiber was determined to be closest to two different cortical regions (from the two hemispheres), it was removed as well to ensure that only homologous connections are considered. Examples of labeled fibers as shown in Fig. 3.4.

Finally, each voxel in the MSCC can be labeled according to the connectivity of fibers crossing it. If streamlines passing through the voxel connect to multiple cortical zones, the voxel is labeled according to the cortical zone that has the most fibers passing through the voxel. If no streamlines pass through a voxel, it has a clear label.

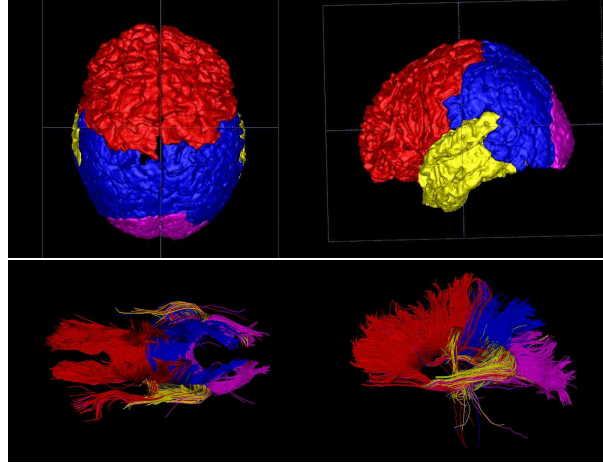


Figure 3.4: Examples of warped labeled atlas in the space of T1-weighted image (top row) and labeled fibers (bottom row). The left ones are axial view, and the right ones are sagittal view. The colors are: red for frontal lobe, blue for parietal lobe, yellow for temporal lobe and purple for occipital lobe.)

Registration Based Normalization

Deformable registration is used to normalize the same dataset, and the results are compared with shape-based normalization. The Symmetric diffeomorphic registration algorithm developed by Avants et al. (Avants and Gee, 2004), one of the state-of-the-art high-dimensional large deformation registration algorithms, is used.

Experiments are carried out for both whole-brain and structure-specific registration. The template used in the registration is iteratively generated from the dataset itself as described in (Avants et al., 2006).

In the whole-brain normalization experiments, the FA images of each subject is registered to the template. Then the labeled fibers are warped into the template space according to the registration result. The MSCC segmentation and the connectivity labeling are therefore performed in the template space. However, in our evaluation dataset, due to the low signal-to-noise ratio in the FA images, the normalization quality is quite poor. And thus the results are not used in the comparison.

In the structure-specific registration, considering the homogeneity on the interior of

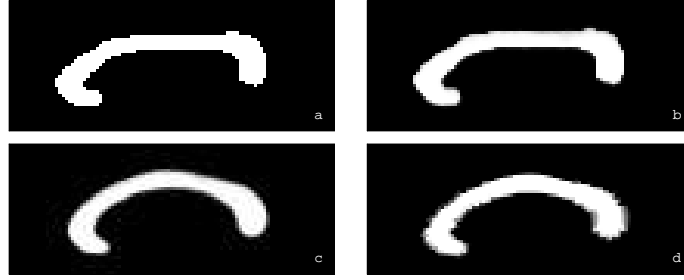


Figure 3.5: An illustration of 2D diffeomorphic registration, (a) is a single subject, (c) is the template constructed from the population of 30 corpora callosa, and (b) and (d) are the results after registering (a) and (c) diffeomorphically and symmetrically.

corpus callosum, the segmented 2D binary mask image of MSCC is directly used for registration. For each subject, the MSCC mask image is registered to the template, and the DTI-based measurements are then warped to the template space according to the registration results.

Fig. 3.5 shows the constructed template for 30 instances of corpus callosum and the registration result for one subject.

3.3 Results

3.3.1 Subjects and Data Acquisition

The evaluation experiments use a dataset from a chromosome 22q11.2 deletion syndrome (DS22q11.2) study at the Department of Psychiatry and Behavioral Science, M.I.N.D. Institute of University of California, Davis and Children’s Hospital of Philadelphia. It includes 3 Tesla high-resolution structural MRI and diffusion tensor MRI scans for 11 typically developing children and 19 children with the DS22q11.2 syndrome. Scans were performed on 3 Tesla Siemens Trio scanners at the Hospital of the University of Pennsylvania (13 children with DS22q11.2 and 7 controls) and at the University of California, Davis Imaging Research Center (6 children with DS22q11.2 and 4 controls). The analysis below does not consider the confounding effects of location; however, similar results of

lower significance are observed when analyzing the data from each location separately. The structural MRI was acquired using a T1-weighted magnetization-prepared rapid gradient echo (MP-RAGE) sequence with the following scanning parameters: repetition time (TR) 1620 ms, echo time (TE) 3.87 ms, 15° flip angle, number of averages = 1, matrix size = 256×192 , slice thickness of 1.0 mm, spacing between slices of 1.0 mm, yielding 160 axial slices with in-plane resolution of 0.98×0.98 mm. A single-shot, spin-echo, diffusion-weighted echo-planar imaging (EPI) sequence was used for the diffusion tensor MRI. The diffusion scheme was as follows: one image without diffusion gradients ($b = 0$ s/mm²), hereafter referred to as the $[b = 0]$ image, followed by twelve images measured with twelve non-collinear and non-coplanar diffusion encoding directions isotropically distributed in space ($b = 1000$ s/mm²). Additional imaging parameters for the diffusion-weighted sequence were: TR = 6500 ms, TE = 99 ms, 90° flip angle, number of averages = 6, matrix size = 128×128 , slice thickness = 3.0 mm, spacing between slices = 3.0 mm, 40 axial slices with in-plane resolution of 1.72×1.72 mm.

3.3.2 Cm-Rep Fitting Accuracy Analysis

The MSCC was manually segmented from the FA images using ITK-SNAP (Yushkevich et al., 2006a) (www.itksnap.org). Then, following the procedure described in the methods section, cm-rep models were fitted to the MSCC mask images. In our current implementation, a multi-resolution cm-rep template is used, in which the number of cm-rep coefficients goes from $16 \times 3 + 2$ to $30 \times 3 + 2$. It usually takes 3-4 mins to fit a cm-rep to one MSCC on a single CPU. Without the closed-form solution described in Sec. 3.2.2, the same process takes 20-30 mins.

Fig. 3.6 shows some fitting examples, in which the fitted cm-rep is overlaid on the mask images of the MSCC. The grid lines of PISA reference frame are also illustrated.

The overlap between a fitted cm-rep model \mathcal{C} and the target MSCC instance \mathcal{H} is

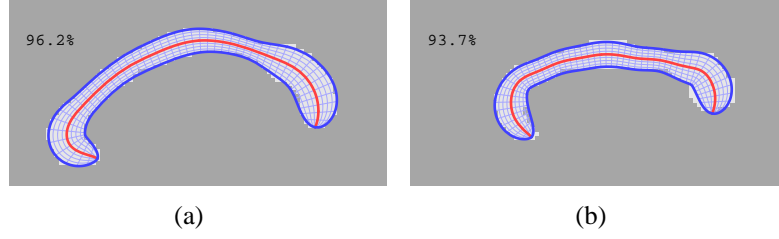


Figure 3.6: Illustration of fitted cm-reps overlaid on the binary images of corpora callosa, with Dice coefficients given on the top. The boundary of the fitted cm-reps are outlined in dark blue. The red lines are PISA medial curves. The thin, light blue curves indicate the grid lines of PISA reference frame. Example (a) Dice coefficient is the highest among all 30 subjects, and example (b) Dice coefficient is the lowest.

measured using the *Dice Similarity Coefficient* (Dice, 1945)

$$\frac{2\text{Vol}(\mathcal{C} \cap \mathcal{H})}{\text{Vol}(\mathcal{C}) + \text{Vol}(\mathcal{H})}.$$

The mean Dice coefficient for 11 controls is $95.26 \pm 1.00\%$, and the 19 DS22q11.2 subjects is $95.31 \pm 0.76\%$, statistics on the Dice coefficients shows that there is no significant difference in fitting accuracy for the groups (p-value: 0.4460). The mean Dice coefficient for all 30 subjects is $95.29 \pm 0.84\%$.

3.3.3 Validation of the Closed Form Solution

The analytical solution given in previous section guarantees that as long as the cm-rep coefficients generated from the solution satisfy certain inequality conditions defined in (Yushkevich et al., 2006b), the locus $\{\mathbf{m}(t), R(t)\}$ is precisely the medial axis of the object b generated by inverse skeletonization. This assertion is validated empirically by examining the displacement between the medial axis encoded in the cm-rep model and the medial axis computed using Voronoi skeletonization of the model's boundary. The model boundary is sampled into discrete points and their internal Voronoi Diagram is computed. Then the distance from each vertex of the internal Voronoi Diagram to the continuous medial curve is computed. The maximum and mean values of this distance, averaged over all 30 MSCC cm-rep models, are plotted in Fig. 3.7. With an increasing number of sampling

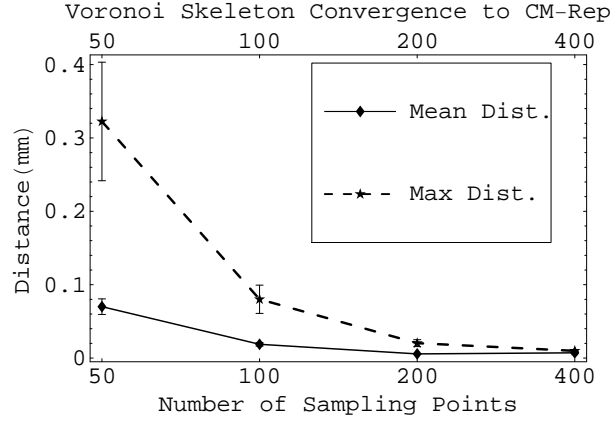


Figure 3.7: The convergence of the Voronoi skeleton of the *cm-rep* boundary to the *cm-rep* medial curve, over increasing sample density. The number of sample points on the *cm-rep* boundary is plotted on the horizontal axis, and the distance from the discrete Voronoi skeleton to the continuous *cm-rep* medial curve is plotted on the vertical axis. Both the mean distance and the maximum distance are plotted. The values are averages over 30 *cm-rep* models.

points, the medial axis computed with Voronoi skeletonization approaches the medial axis encoded in the model.

3.3.4 Matching of the Connectivity Labels

Given the connectivity-based labeling of the MSCC described in Sec. 3.2.6 and shown in Fig. 3.8, it is possible to evaluate normalization algorithms based on how well they align connectivity labels across subjects. Although there is no “ground truth” against which different normalization methods can be evaluated, the degree to which connectivity labels are aligned can be construed to reflect the ability to recover the underlying anatomical correspondences.

In our evaluation experiment, each normalization method was applied to the DS22q11.2 cohort, the control cohort, and the two cohorts combined. In each case, the subjects’ connectivity maps were warped into the normalized space. Connectivity maps vary slightly depending on the variation of the fiber tracking method used to obtain them. Fig. 3.9 and Fig. 3.10 compare the mean connectivity maps of all 30 subjects for two of the 8 tracking

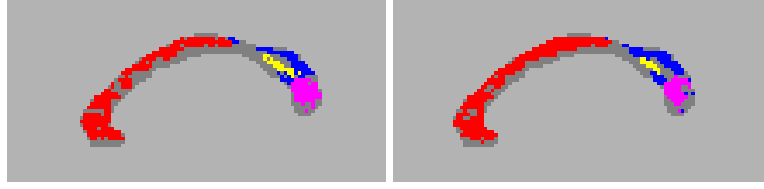


Figure 3.8: Example of connectivity labeling on MSCC. The left and right figures are for FACT and VINT tracking method respectively, with FA threshold 0.25 and curvature threshold 60 degrees. A number of voxels have a clear label, which means that the tractography could not trace a streamline passing through that voxel with both ends close enough to the same cortical regions in the left and right hemispheres.

methods described in Sec. 3.2.6. The boundaries between different labels vary slightly, but the segmentations are broadly similar.

To measure how well each normalization method aligns the connectivity maps, we measure the Dice overlap coefficient between normalized maps. Overlap is computed separately for each of the four labels in the connectivity map and is averaged among all pairs of subjects within each cohort. Table 3.1 lists the average overlaps for one of the tracking settings, showing significantly higher overlap for the cm-rep method. The comparison was repeated for the 8 variations of the tracking setting, and in all 8 cases, the overlaps with the cm-rep method were higher than for region-based registration for all four lobes and for both DS22q11.2 children and controls. The difference in overlaps was statistically significant in almost all cases, with the exception of the temporal lobe, where the p-value exceeded 0.05 (the temporal lobe occupies a very small portion of the connectivity map and is matched poorly by all normalization methods). The maximum p-values among all 8 tracking methods are also included in Table 3.1.

We also attempted to use whole-brain registration directly on FA images to normalize the MSCC. However, the images in the DS22q11.2 dataset have low signal-to-noise ratio, which results in poor normalization quality and low overlap for connectivity maps. Therefore we did not include these results in the comparison, as they may not reflect fairly on the method’s performance in a different dataset.

To help explain the differences between the two normalization methods, we examine

Table 3.1: Comparison of deformable registration based normalization and *cm-rep* based normalization for matching the connectivity label of each lobe in 30 subjects from a DS22q11.2 study. The quality of label matching is quantified using Dice similarity coefficients between pairs of subjects. Statistics are carried out to measure the significance of the differences between normalization methods. Results are listed for tracking setting 1 (FACT, FA threshold 0.25 and curvature threshold 60 degrees). The max p-values over all 8 tracking settings are also listed.

		FRONT	PAR	TEMP	OCC
CTRL (11 sub- jects)	registration (setting 1)	0.735	0.481	0.124	0.514
	cm-rep (setting 1)	0.811	0.553	0.134	0.633
	p-value (setting 1)	< 0.001	0.006	0.387	<0.001
	p-value (max over 8 settings)	< 0.001	0.030	0.478	0.007
DS22q11.2 (19 sub- jects)	registration (setting 1)	0.768	0.481	0.264	0.495
	cm-rep (setting 1)	0.835	0.546	0.272	0.608
	p-value (setting 1)	<0.001	<0.001	0.362	< 0.001
	p-value (max over 8 settings)	<0.001	<0.001	0.408	< 0.001
All (30 sub- jects)	registration (setting 1)	0.761	0.483	0.209	0.503
	cm-rep (setting 1)	0.824	0.543	0.215	0.614
	p-value (setting 1)	<0.001	<0.001	0.334	<0.001
	p-value (max over 8 settings)	<0.001	<0.001	0.420	<0.001

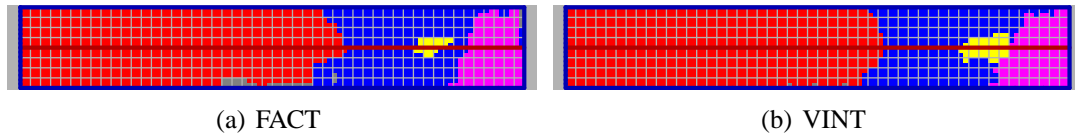


Figure 3.9: The mean connectivity map rendered on the *cm-rep* coordinate system. The left and right figures are for FACT and VINT tracking method respectively, with FA threshold 0.25 and curvature threshold 60 degrees.

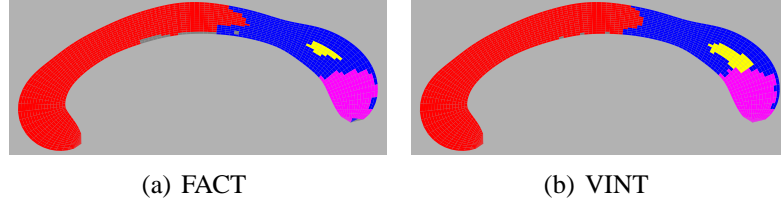


Figure 3.10: The mean connectivity map obtained by the cm-rep approach rendered on mean MSCC shape. The left and right figures are for FACT and VINT tracking method respectively, with FA threshold 0.25 and the curvature threshold 60 degrees.

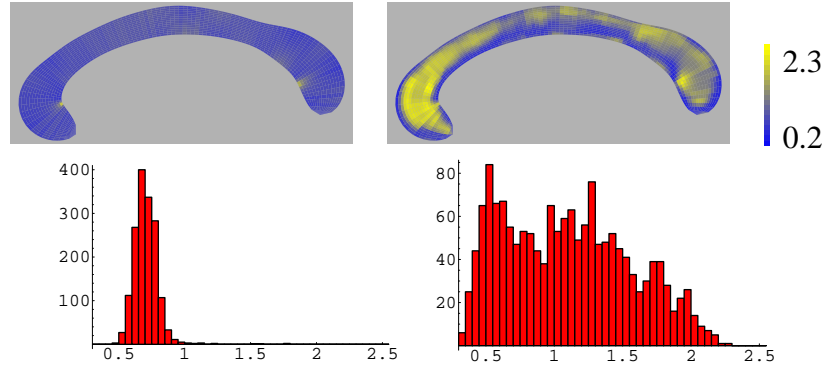


Figure 3.11: Illustration of the Jacobian determinant maps inside the MSCC for one subject. On the left is the result for cm-rep mapping, on the right is the result for deformable registration. The color coded Jacobian determinant maps are plotted on the top. The histograms of the Jacobian determinant maps are plotted on the bottom.

the Jacobian determinant maps associated with warping each subject into the normalized space. The average (over all 30 subjects in the study) variance of the Jacobian determinant map inside MSCC is 0.22 for registration based normalization, and 0.06 for cm-rep based normalization. We plotted the Jacobian determinant maps and their histograms for one of the subjects in Fig. 3.11. The Jacobian map for cm-rep normalization is much more uniform over the extent of the MSCC than the Jacobian map for registration. This is to be expected, since cm-rep correspondences are more global in nature than correspondences based on local regularization priors, which are employed in registration. This difference in deformation fields can help explain better alignment of connectivity maps by the cm-rep method.

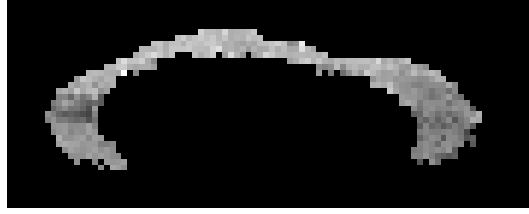


Figure 3.12: An example of the tract-wise mean FA map for one subject.

3.3.5 Statistics on Tract FA Maps

Finally, we compare the effect of normalization on the power of statistical analysis involving mean FA features derived from diffusion tensor tractography. As described in Sec. 3.2.6, a tract-wise mean FA value is associated with each point in the corpus callosum in each subject. An example mean FA map is shown in Fig. 3.12. Using each normalization method, these mean FA maps are warped to a common template space, in which point-wise statistical analysis (a two-sample unpaired t -test comparing DS22q11.2 children and controls; 28 degrees of freedom) is performed. Regions of statistical significance in the template space are found using cluster analysis with permutation testing (Hayasaka and Nichols, 2003), which is a well-established strategy to improve sensitivity by analyzing co-activation at contiguous pixels. The threshold of $t=3.13$ is used to select clusters, and permutation testing is used to build an empirical distribution of cluster size under the null hypothesis.

For normalization based on region-of-interest registration, no clusters with p -value below 0.05 are detected, regardless of the tracking method used. In contrast, cm-rep normalization finds a significant cluster in the mid-section of the MSCC. This cluster is found consistently for different tracking methods, as illustrated in Fig. 3.13.

By collapsing the tract FA data on the PISA skeleton, the different pattern of the two groups becomes more clear. We summarize the value of all points with the same t PISA coordinate, and plot the averaged value along PISA skeleton, as shown in Fig. 3.14. The averaged tract FA values for control group appear to have three peaks along the PISA skeleton, while for DS22q11.2 group there is no obvious middle peak. The statistical

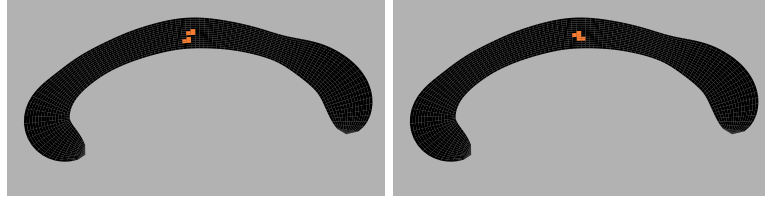


Figure 3.13: Areas showing significant differences for tract FA maps between the control and DS22q11.2 groups, shown as colored overlays on the mean MSCC shape. The left and right images are results for FACT and VINT fiber tracking method respectively, with FA threshold 0.25 and curvature threshold 60 degrees. Results obtained by cm-rep based normalization and permutation based clustered pixel analysis. The adjusted p-values for colored regions are below the 0.05 threshold.

analysis confirms the significance of this difference. This experiment demonstrates an extra utility of the shape-based reference frame. In addition to shape normalization, the shape-based reference frame also offers a way to group voxels meaningfully, which may improve the statistical power in group analysis.

3.4 Discussion

This chapter presents a new efficient algorithm for modeling, measuring and normalizing 2D anatomical structures on the basis of medial geometry. In addition it undertakes a comparison of shape-based normalization of the corpus callosum between the proposed method and the technique most commonly used to normalize imaging data: registration. The purpose of this comparison is to demonstrate the relevance of the proposed method by showing that it can have a positive impact on the outcome of medical imaging studies. The results using DTI data from a chromosome DS22q11.2 deletion study demonstrate that shape-based normalization of the corpus callosum using cm-reps makes it possible to detect statistical differences between populations that were not detected when registration was used to normalize the structures. A direct comparison of the alignment of connectivity maps between cm-reps and registration give further justification to the use of cm-reps,

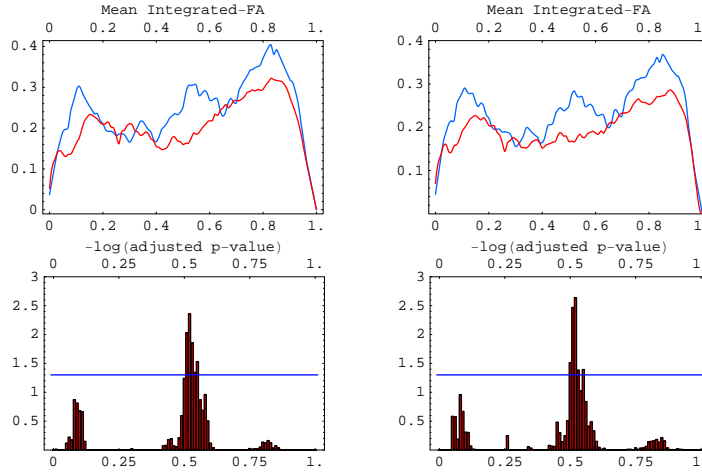


Figure 3.14: This figure illustrates the differences of summarized tract FA on PISA skeleton between the control group and DS22q11.2 group. Different tracking methods are used for producing figures on left and right, both with FA threshold 0.25 and curvature threshold 60 degrees. FACT is used for the images on the left, and VINT is used for the images on the right. Figures on the top shows the mean tract FA map of each groups after collapsing onto the PISA skeleton. The blue curves are for control group and red curves are for DS22q11.2 group. Figures on the bottom are the plot of $-\text{Log}(\text{adjusted p-values})$ for multiple statistical tests on the difference between the two groups. The p-values are corrected for multiple comparison using step down permutation. The blue line is the significant threshold corresponding to adjusted- $p=0.05$.

suggesting that shape-based correspondences in the corpus callosum more accurately reflect the underlying anatomical correspondences. The fact that both types of results are stable with respect to the choice and the parameters of the diffusion tensor tractography algorithm adds further weight to our findings. Together, these findings give compelling support to the use of cm-reps in DTI morphometry studies.

While registration is a general technique, the 2D cm-rep approach is limited in its applicability in the human body. However, given the interest in DTI-based white matter analysis, and given the number of studies that examine corpus callosum morphometry, the method’s ability to improve inferences about this structure’s properties justifies, in our view, the additional efforts associated with using it in a study.

Further improvements to the shape based correspondence are possible under the cm-rep framework. In this study, the correspondence is established by equal arc length subdivision of the PISA skeleton. An alternative would be to use an MDL-style approach to compute optimal boundary or skeleton correspondences, and propagate them to object interiors. The thickness and curvature information, which is attached to each points on the boundary or skeleton curve, can be readily used for such correspondence optimization.

Knowing that the corpus callosum has a homogenous interior in structural MRI, the correspondences computed in the current method are entirely shape-based. If there was intensity or other appearance information inside the structure, the correspondence problem could be formulated as a registration inside of the cm-rep coordinate space. The deformation field by this registration is then just a local refinement of the correspondence established by the global shape, with several available options: (1) deformation restricted to t , which stretches the medial curve and preserves the “depth” coordinate ξ ; (2) deformation that allows us to stretch ξ , but preserves the boundary and medial curve; or (3) fully free deformation in t, ξ .

Chapter 4

A New Branching Medial Model for 3D Geometric Objects

After examining a 2D medial model and its application in Chapter 3, this chapter deals with 3D cases. I propose a new way to construct the branching medial model which can be efficiently applied to 3D complex shapes. The new branching medial model is tested on a large segmented cardiac dataset. I also explored how the medial features of the heart vary among different disease groups.

This chapter is based on papers (Sun et al., 2008a,b, 2009). The coauthors of the three papers include Dr. Paul A. Yushkevich, Dr. Sandhitsu R. Das and Dr. James C. Gee at University of Pennsylvania and Dr. Alejandro F. Frangi, Dr. Federico Sukno, Dr. Sebastian Ordas, Catalina Tobon-Gomez at University of Pompeu Fabra and Dr. Marina Huguet at CETIR Sant Jordi in Barcelona. Their contribution is invaluable for the conduction of the research.

4.1 Introduction

Most 3D applications of the medial models in the literature are for anatomical structures with *simple shape* (also called *single-figure shape*) whose medial axis can be described by

a single curve or surface sheet (Pizer et al., 2003; Gerig et al., 2003; Styner et al., 2003a,b). There have been efforts to model complex shapes (whose medial axes have branches) using m-reps. Han et al. (Han et al., 2005) proposed a “*multi-figure*” m-rep that represents each part of a complex object using single-figure m-rep, and then uses surface blending to attach a “child” single-figure m-rep to its “parent”. This type of model is very useful when complex objects have a “parent-child” organization of parts (like the hand, with a palm and five fingers). But it uses a membrane-like connection between parts instead of following the Blum’s medial geometry. For cm-rep, as I have introduced in Chapter 2, two different types of approaches have been proposed to construct branching medial model. Terriberry et al. proposed the first solution which is tightly coupled to the underlying Catmull-Clark surface representation. And Yushkevich et al. (Yushkevich, 2008) extended the PDE-based cm-rep approach to branching medial model by using biharmonic PDE instead of the Poisson PDE. However, to the best of my knowledge, both approaches have not yet been applied to large-scale anatomical modeling.

An important message conveyed by Terriberry’s method is that the equality constraints required by the medial geometry along edge and branching curves can be enforced by local corrections, without affecting the medial model globally. Inspired by this idea, I propose a new way to resolve the problem and construct branching medial models. I first use soft penalties to admit solutions that only slightly violate the equality constraints, and then use brute-force local adjustment to correct the remaining violations. This approach does not couple the modeling approach to a particular representation of the medial surface and leaves the freedom to choose the suitable representation according to the application.

In this chapter, I demonstrate the proposed branching medial model by applying it to 3D cardiac shapes. Analysis of cardiac images is an active area of research (Frangi et al., 2001a). One important feature of medial axis is that it can be used to compute wall thickness. The 2D “centerline method” (Sheehan et al., 1986) and its 3D extension 3D “centersurface method” (Bolson and Sheehan, 1993) are both based on medial axis. However, the 3D “centersurface method” only deals with a single heart chamber. In addition,

the detailed thickness maps generated from different objects are not aligned, posing problems for further population comparison. Although it is possible to divide the thickness maps into big segments using the standard 17-segments of the left ventricle in polar plot (Cerqueira et al., 2002), the spatial variation within each segment will be lost. As opposed to skeletonization, the medial model describes the skeleton of a structure of interest using parametric surfaces, which allows us to directly perform surface-based statistical analysis. In this chapter, I applied the branching medial model to generate detailed thickness and thickening maps based on the segmented MR images. The mean thickness and thickening maps for healthy population are computed and visualized. I also use the statistics derived from the healthy group to identify regions with abnormal thickness or thickening for a new patient as an example of the usage. The thickness and thickening maps of acute myocardial infarction (AMI) patients and hypertrophic cardiomyopathy (HCM) patients are compared with those of normal subjects using cluster-based analysis.

The rest of this chapter is organized as follows: Sec 4.2 presents the proposed method in detail. Sec 4.3 shows the results of fitting a bi-ventricular medial template to a large set of cardiac segmentations and the comparison between . Finally, Sec 4.4 discusses the paper’s contributions, limitations and future research plans.

4.2 Methods

This section presents the detail of the branching medial model and how the model is constructed for bi-ventricular shapes. As illustrated in Terriberry’s demonstration (Terriberry, 2006), if the medial axis is modeled by Catmull-Clark subdivision surfaces, the equality medial constraints along medial edge and branching curves can be enforced by locally modifying the medial axis at edge and branching curves to use interpolating splines. In fact, examination of equations reveals that the equality medial constraints only involve the first order derivatives of variables along the edge and branching curves, and thus can be

satisfied by localized adjustment. In this chapter, instead of explicitly working out the local adjustment for a special type of surface representation, as done by Terriberry et al., we would like to propose a new method to first obtain solutions that only slightly violate the medial constraints via soft-penalty optimization, and then enforce the constraints implicitly by a local adjustment. Unlike Terriberry's approach which is specific to Catmull-Clark subdivisions surface, the new proposed approach can be easily implemented for a large class of function representations for skeleton in the medial model. In Subsec 4.2.1, we derive the soft penalties corresponding to the equality constraints. The soft penalties will be equal to zero when the equality constraints are satisfied, and have positive values when the equality constraints are violated. In Subsec 4.2.2, we explain how those soft penalties, along with other terms, are incorporated in the deformable model fitting framework to derive medial models for real-world objects. The solution obtained by model fitting is still not perfect, and in Subsec 4.2.3, we describe how to further locally correct the medial model. Subsec 4.2.4 describes the process to construct bi-ventricular medial template for the heart and implementation details are given in Subsec 4.2.5.

4.2.1 Soft Penalty Terms

Along the medial edge curve, the soft penalty for violating the medial constraint can be simply written as:

$$(\|\nabla_{\mathbf{m}} R\| - 1)^2. \quad (4.1)$$

Now let us focus on the equality constraints along medial seam curves. Let $\gamma(s) : [0, L) \rightarrow \mathbb{R}^3$ denote the parametric form of the medial seam curve, parameterized by the arclength s , where L is the length of the seam curve. Let $\vec{T}_\gamma(s)$ be the unit tangent vector along γ and let $\vec{\nu}_i(s)$ be the outward unit normal vector along $\gamma(s)$, i.e., $\vec{\nu}_i \perp \vec{\mathbf{N}}_{\mathbf{m}_i}$ and $\vec{\nu}_i \perp \vec{T}_\gamma$. Note that

$$\nabla_{\mathbf{m}_i} R = R_{,s} \vec{T}_\gamma + R_{,\vec{\nu}_i} \vec{\nu}_i,$$

where $R_{,s}$ and $R_{,\vec{\nu}_i}$ denote the partial derivative of R with respect to s and $\vec{\nu}_i$ respectively. This expression allows us to rewrite the equality constraint along the medial seam curves as:

$$R_{,\vec{\nu}_i} \big|_{\gamma} - \sqrt{1 - (R_{,s})^2} \cos \alpha_i = 0, \quad (4.2)$$

where α_i is the angle between the tangent planes of the medial manifolds $\mathbf{m}_{i \oplus 1}$ and $\mathbf{m}_{i \oplus 2}$, i.e.,

$$\cos \alpha_i = \vec{\nu}_{i \oplus 1} \cdot \vec{\nu}_{i \oplus 2},$$

with \oplus denoting addition modulo 3. Accordingly, the soft penalty for violating this constraint can be put as:

$$(R_{,\vec{\nu}_i} \big|_{\gamma} - \sqrt{1 - (R_{,s})^2} \cos \alpha_i)^2. \quad (4.3)$$

4.2.2 Deformable Model Fitting

This section addresses the problem of how to derive the medial model to describe a real-world object \mathcal{H} . Similar to other continuous medial models (Yushkevich et al., 2006b; Terriberly, 2006), a medial template \mathcal{C} is deformed by modifying the control coefficients of \mathcal{C} , so as to maximize the match between the \mathcal{C} and \mathcal{H} , while ensuring that \mathcal{C} satisfies certain regularity and validity constraints.

Formulated in the Bayesian framework, the branching medial template \mathcal{C} is fitted to a real-world object \mathcal{H} by maximizing the posterior probability $p(\mathcal{C}|\mathcal{H}) \sim p(\mathcal{H}|\mathcal{C})p(\mathcal{C})$. The optimization problem is solved by the Conjugate Gradient Decent method.

The first likelihood term $p(\mathcal{H}|\mathcal{C})$ is measured by the volumetric overlap between the real-world object and the medial model interior. In this chapter, we assume the object is represented by a mask image $\mathcal{M} : \mathbb{R}^3 \rightarrow \mathbb{R}$ such that \mathcal{M} is positive on \mathcal{H} and negative on $\mathbb{R}^3 \setminus \mathcal{H}$. In practice, masks are generated by the interpolation of binary characteristic images, possibly after smoothing. Thus the first term can be computed by:

$$p(\mathcal{H}|\mathcal{C}) = \frac{1}{V_{\mathcal{H}}} \int_{\mathcal{C}} M(x) dx, \text{ where } V_{\mathcal{H}} = \int_{\mathcal{H}} M(x) dx. \quad (4.4)$$

The spoke vectors in the medial model allow us to sample the whole medial model interior, so that the overlap term in (4.4) can be computed efficiently.

The second term is the prior term which ensures the *validity* and *regularity* of the solution. The *validity* terms enforce the medial constraints. The equality constraints along medial seam and edge curves are enforced using soft penalty terms as given in Eqs (4.1) and (4.3). There are also several more inequality constraints that have been described in detail in literatures (Yushkevich et al., 2006b), like $\|\nabla_m R\| < 1$ for all type 1 points and the Jacobian constraint to prevent local self-intersection of the boundary. The *regularity* terms further regularize the solution by enforcing desired properties, such as the quality of the control mesh or the preservation of area elements. The regularity terms in our implementation are described in Subsec 4.2.5.

4.2.3 Local Correction

A small violation of the medial constraints still remains after the soft-penalty optimization. The following local adjustments are applied to ensure that the boundary generated from the medial axis is closed. Along the medial edge, each pair of spokes is given the mean value of this pair:

$$\hat{\mathbf{U}}^\pm = \frac{\mathbf{U}^+ + \mathbf{U}^-}{2}, \quad (4.5)$$

and the corresponding boundary points are updated. Similarly, along the medial seam, we assign spokes to be:

$$\hat{\mathbf{U}}_{\mathbf{m}_i}^+ = \frac{\mathbf{U}_{\mathbf{m}_i}^+ + \mathbf{U}_{\mathbf{m}_i \oplus 1}^-}{2} \quad (4.6)$$

$$\hat{\mathbf{U}}_{\mathbf{m}_i \oplus 1}^- = \frac{\mathbf{U}_{\mathbf{m}_i}^+ + \mathbf{U}_{\mathbf{m}_i \oplus 1}^-}{2}, \quad (4.7)$$

and the corresponding boundary points are subsequently updated.

These small local corrections ensure all parts of the boundary to connect seamlessly, resulting in a similar effect as explicitly adjusting the derivatives of medial axis to enforce the medial constraints in Terriberry's Catmull-Clark subdivision surface medial model

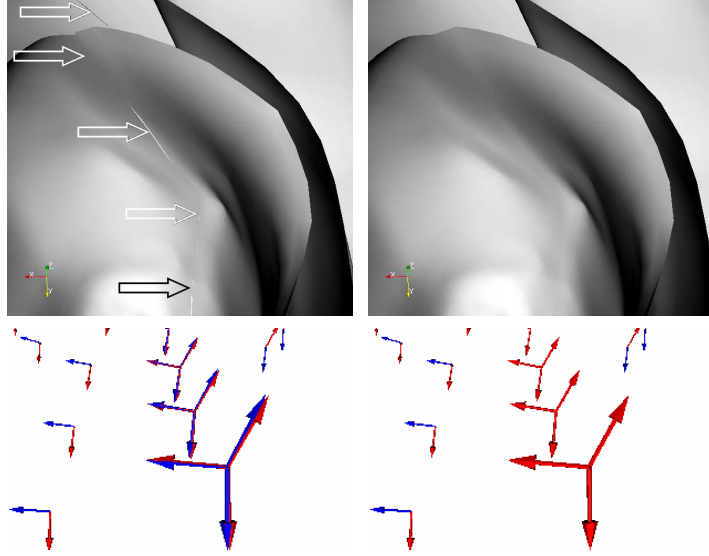


Figure 4.1: This figure illustrates the result of the deformable model with soft penalties and the effect of local correction. The left column shows the results after deformable fitting with soft penalties. The right column shows the results after local correction. The top row is part of the model boundary, note that before the correction, there are very tiny seams on the boundary, indicated by the arrows, which disappears after the correction. The bottom row shows part of the spoke vector field. Note that before the correction, the 6 spokes for the point on medial seam do not match perfectly into 3, but have very small discrepancy within each pair (one red and one blue as a pair), while after the correction only 3 spokes can be observed.

(Terriberry, 2006). As long as the soft penalties are enforced on the geometry at medial edges and seams, the needed correction should be tiny in practice. Fig 4.1 shows the medial geometry before and after the local correction around the medial seam.

4.2.4 Bi-Ventricular Medial Template

The deformable medial model fits an initial cardiac medial template to the cardiac shapes; thus, prior to the fitting, a cardiac medial template needs to be generated. In theory the template can be any simple hand-created model as long as the branching topology is correct. However, a data-driven model which is closer to the true solution obviously would help the deformable model avoid local minima in the optimization process.

In our work, the myocardium of the left and right ventricles are explicitly modeled

using medial surfaces. The template of the heart wall is derived through several steps. We start from the manual segmentations. First, a volumetric template is iteratively generated from the segmentations using a scheme in (Joshi et al., 2004) and the symmetric diffeomorphic registration algorithm developed by Avants et al. (Avants and Gee, 2004). Then, the volumetric template is binarized and the Voronoi Skeleton of the binary image is computed using qhull (Barber et al., 1996). We then intersect the dense Voronoi Skeleton mesh with a set of cutting planes that are orthogonal to the LV long axis and obtain the 2D intersection curves. The curves are uniformly sampled to generate the mesh points. The final medial template for the LV and RV contains 195 points and 381 triangles at the basic control mesh. We note this is sparser than the boundary meshes of some published papers. For example, in (Zheng et al., 2008), 545 points and 1056 triangles are used for the left ventricle while 761 points and 1476 triangles are used for the right ventricle. And in (Peters et al., 2009) 7286 vertices and 14771 triangles are used for all four chambers of the heart. We have experimented to use a denser mesh by subdividing the template control mesh, however, the performance gain is trivial. Thus it seems that a light weighted template is good enough for our application on short-axis MR images. Figure 4.2 illustrated the medial template. To initialize the deformable model for a particular cardiac shape, we warp the medial template according to the deformation field we saved in the volumetric template construction step, and we use the deformed medial template as the initialization. The pipeline is illustrated in Fig 4.2.

4.2.5 Implementation Details For The Medial Model

In our implementation, Loop subdivision surfaces (Loop and DeRose, 1990) are used to represent skeletons. Loop subdivision surfaces are especially well suited for describing the skeleton with complicated topology, because of their triangular elements and simplicity. The triangular control meshes for Loop subdivision surfaces can be recursively refined by inserting a vertex into each edge in the parent-level according to a set of subdivision rules, allowing multi-resolution model fitting. Boundary reconstruction from the skeleton

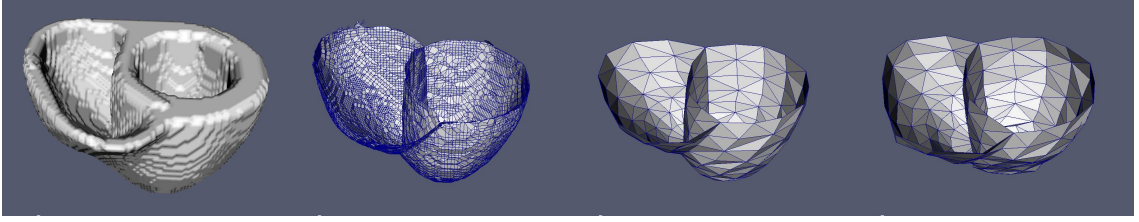


Figure 4.2: Medial template building and deformable model initialization pipeline. First: the boundary of the binarized volumetric template constructed by iterative unbiased averaging algorithm. Second: the pruned Voronoi Skeleton; note that it still has some small branches and the mesh is dense. Third: the medial template constructed under manual control. Fourth: example of a deformed medial template as the initialization for one cardiac shape.

requires only up to first order derivative information. We calculate them according to the equations given by Xu (Xu, 2004), which involves one ring of neighbors for each vertex. The soft penalties are computed on all vertices along medial seams and medial edges and their average values are used in the objective function of the deformable model. In practice, we find that the vertices on the medial seam need to have at least a valence of 3 to get enough freedom to satisfy the branching constraints.

In our implementation, two *regularity* terms are used in the deformable model fitting. Since we use a Loop subdivision surface to represent the skeleton, one regularity term is used to control the quality of the subdivision mesh by penalizing large and small angles in the mesh triangles. It can be put as:

$$p_{regularity-mesh} \sim \sum_{i=1}^T \sum_{k=1}^3 \cos(\theta_k^i), \quad (4.8)$$

where T is the total number of triangles on the subdivision medial surface and θ are the internal angles of these triangles. The second regularity term we use enforces area-based correspondence of the skeleton by penalizing the distortion of area elements with respect to the template. In our Loop subdivision surface representation, this term is implemented as:

$$p_{regularity-correspondence} \sim \sum_{i=1}^V \left\| \nabla_m \left(\frac{A^i}{A_{template}^i} \right) \right\|^2, \quad (4.9)$$

where V is the total number of vertices on the subdivision medial surface, A^i is the effective area element of the i^{th} vertex which can be computed as one third of the total area of all triangles belonging to this vertex, and similarly $A_{template}^i$ is the effective area element of the i^{th} vertex on the template.

The multi-resolution deformable model fitting has two stages. The initial template mesh is subdivided once in the first stage and twice in the second stage to represent the medial axis, and the target bi-ventricular binary mask is smoothed by Gaussian kernel with variance 2 in the first stage and variance 0.6 in the second stage.

4.2.6 Cluster-Based Comparison Between Subject Groups

After the medial model is fitted for each subject, the radial scalar field is used as a local thickness measurements. And the systolic thickening M is defined as the changing ratio in thickness from ED to ES relative to the ED thickness,

$$M = \frac{S_{ES} - S_{ED}}{S_{ED}} \quad (4.10)$$

where S_{ES} and S_{ED} are the ES and ED thicknesses, respectively.

Groupwise comparison can be a useful tool to study various pathology processes. For example, it might be interesting to investigate whether there is a difference in the thickness and thickening pattern of ventricular hypertrophy caused by different stimuli (eg, high blood pressure and exercise). Also, although the AMI occurs locally for each patient, still some areas might be affected more often than others in certain population. This information can potentially be revealed by groupwise comparison of thickness and thickening maps.

The medial model provides a detailed thickness and thickening map on the skeleton mesh where a direct pointwise comparison can be easily performed. To account for multiple hypothesis testing, the widely used non-parametric cluster-based analysis with family-wise error rate (FWER) correction (Hayasaka and Nichols, 2003) is applied to the

groupwise comparison of thickness and thickening. Cluster-based analysis prefers to select larger connected regions with group difference rather than isolated points based on the assumption that the change of myocardium should have certain extent of continuity.

To compare the thickness/thickening between two groups, we first compute a point-wise t-value using two sample Student's t test at every point on the skeleton. Note that the t-value can be either positive or negative depending on which group has a larger mean value. Then, given a threshold t_0 , corresponding to a p-value p_0 , if t_0 is positive, the *clusters* (connected regions on the skeleton mesh) with $t > t_0$ (or $p < p_0$) are extracted; similarly, if t_0 is negative, the *clusters* with $t < t_0$ (or $p < p_0$) are extracted. The cluster mass is defined as the integral of $|t|$ over a cluster. Permutation testing is used to build an empirical distribution of cluster mass which yields the *permutation corrected* p-value for each cluster (Hayasaka and Nichols, 2003).

4.3 Results

4.3.1 Materials

The data set we used contains 428 heart shapes from 90 subjects consisting of both healthy subjects and patients suffering from common cardiovascular pathologies, including myocardium infarction, hypertrophy, LV dilation, LV aneurysm, RV dilation, LA dilation, RA dilation, and pericarditis. The MR images were generously provided to us by CETIR Sant Jordi Centre (Barcelona, Spain). The MR acquisition parameters are: TR: 3.75 4ms, TE: 1.5-1.58 *ms*, FA: 45, slice thickness: 8-10 *mm*, slice size: 256×256 pixels, resolution: 1.56×1.56 *mm* and FOV: 400×300 *mm*², on a General Electric CVI 1.5 T MR facility. Expert segmentations were manually drawn on the endocardial left ventricle and right ventricle borders, and on the epicardial border of the whole heart to construct a 2-chamber heart model usually including 8-12 slices from the base to the apex. Five different phases of the cardiac cycle were segmented: End Diastole (ED), Mid Systole (MS), End Systole (ES), Diastole 1 (D1) and Diastole 2 (D2).

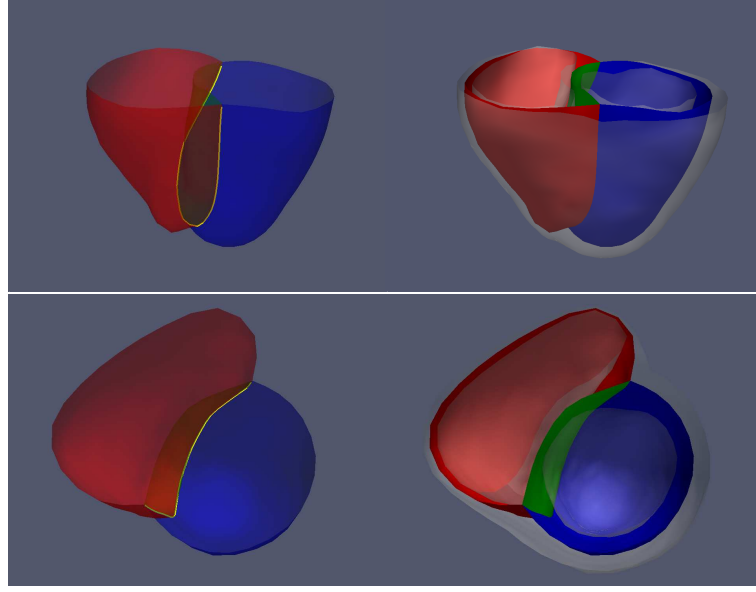


Figure 4.3: Illustration of the medial template. The top row and bottom row are shown from different viewpoints. The medial surfaces are shown as colored meshes with the color indicating different branches of the medial model. There are three different branches: the *blue* surface models the left ventricular posterior wall; the *green* surface models the inter-ventricular septal wall; and the *red* surface models the right ventricular wall. The curve where these three different colored surfaces join together is the branching curve, which is marked using *yellow* color on the left figure where the medial surfaces are rendered as transparent meshes. The boundary surfaces are shown as *white transparent* meshes on the right figure.

4.3.2 Branching Topology

The branching topology of the bi-ventricular medial model is illustrated in Fig 4.3. The medial scaffold is composed of three medial manifolds: one for the septal wall that separates LV and RV, one for the heart wall that only belongs to LV, and one for the heart wall that only belongs to RV. The three medial manifolds join together along a U-shaped branching curve. Because there is a manual cutoff of the left and right ventricles on the base in the segmentation, the model is left open there instead of enforcing a virtual cap. Therefore the medial model does not have medial edge curves. There are two type of points on the medial scaffold for this model: type (3) points on the branching curves and type (1) points on everywhere else.

Table 4.1: The results of fitting branching medial model to 428 cardiac segmentations.

	Mean	Std
Dice Overlap	0.92	0.017
Avg. Dist. Model to Target (mm)	0.67	0.179
Avg. Dist. Target to Model (mm)	0.85	0.220

4.3.3 Fitting Accuracy

The proposed branching medial model is fitted to the 428 manual segmentation of 2-chamber heart model on a 8-CPU Linux cluster over approximately 48 hours. Examples of fitting results are illustrated in Fig 4.4. Given that the fitted cardiac shapes are from both healthy subjects and patients suffering common cardiovascular pathologies, this fitting experiment demonstrates the robustness of the method.

The quality of the fit between a target cardiac shape \mathcal{H} and a fitted medial model \mathcal{C} is evaluated using the following criteria: the Dice similarity coefficient (Dice, 1945) $\frac{2\text{Vol}(\mathcal{C} \cap \mathcal{H})}{\text{Vol}(\mathcal{C}) + \text{Vol}(\mathcal{H})}$; average and maximum distance from boundary of \mathcal{C} to boundary of \mathcal{H} ; and average and maximum distance from boundary of \mathcal{H} to boundary of \mathcal{C} . The results are summarized in Tab 4.1. The cardiac shapes are fitted with mean Dice overlap coefficient of $0.92(\pm 0.017)$ considering the 8-10mm distance between slices. The average distances between the medial model and the target boundaries are 0.67mm and 0.85mm respectively, both at sub-voxel level. Fig 4.6 shows a color map of the average pointwise distance from the model boundary to the target. Most mismatch occurs at boundary points associated with vertices on the branching curve with a small valence. It might be due to the lack of freedom for these vertices to deform while trying to satisfy the branching constraints.

4.3.4 Groupwise Comparison of the Thickness and Thickening Maps

This study uses the branching medial models of 73 subjects belonging to three groups: HCM group (7 subjects with average age 61.5 ± 17.7), AMI group (38 subjects with average age 63.5 ± 11.6), and healthy heart group (28 subjects with average age 50 ± 14.7) where no pathology in the heart has been found.

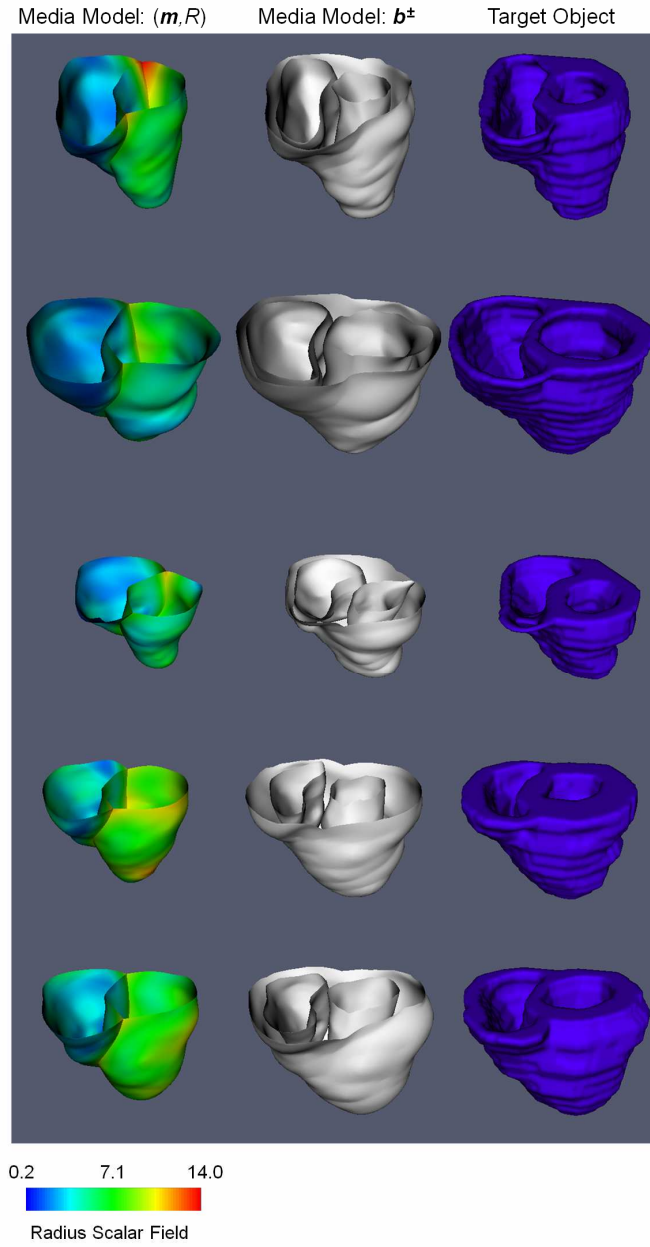


Figure 4.4: Examples of medial models fitted to binary segmentations of 2-chamber heart shapes. For each heart shape, shown are the medial manifold colored by the radius function R , the model boundary generated by inverse skeletonization, and the boundary of the segmentation to which the medial model was fitted.

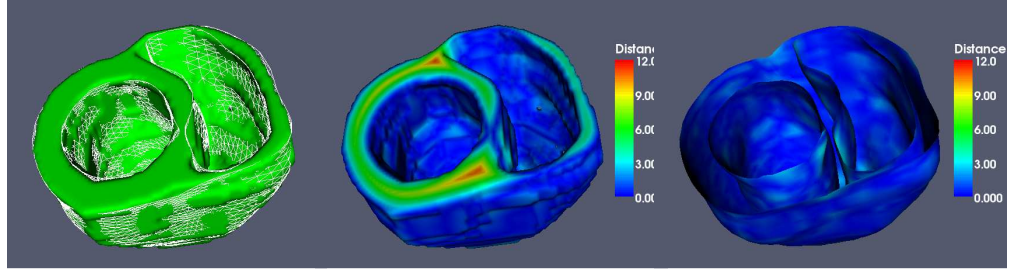


Figure 4.5: Illustration of distance (mm) between the boundary of the target shape and the fitted medial model. The left figure overlays the model boundary, which is shown as white wireframe, on the binary segmentation boundary, which is shown as green surfaces. The middle figure is the distance map from the target to the model. And the right figure is the distance map from the model to the target.

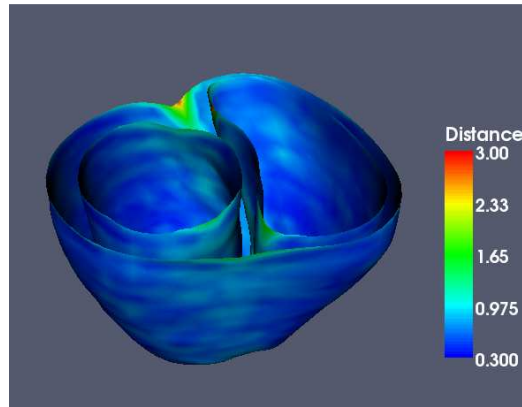


Figure 4.6: Average pointwise distance (mm) from the model boundary to the target for all 428 cardiac shapes.

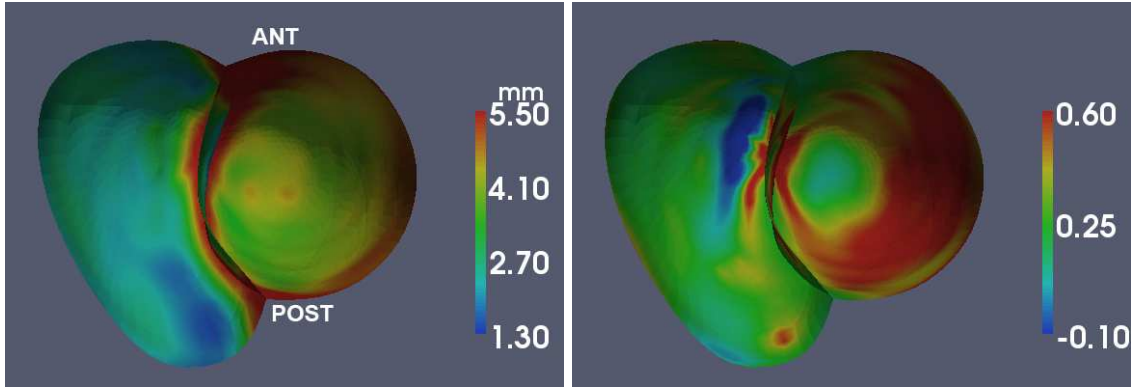


Figure 4.7: The mean thickness (left) and thickening (right) map for 28 healthy hearts in our data set.

The mean thickness and thickening map for the healthy heart group are illustrated on Figure 4.7. As an example, the statistics derived from healthy heart group is used to identify regions with abnormal thickness or thickening for a new patient. The result is illustrated in Figure 4.8. This patient has a region with thicker wall and a region with decreased thickening, suggesting a coexisting condition of hypertrophy and myocardial infarction. Results are consistent with the visual inspection by an expert clinician.

We performed cluster-based groupwise analysis on our dataset, comparing the AMI group and HCM group with the healthy heart group. Significant clusters of each patient subgroup are shown in Table 4.2 and illustrated in Fig. 4.9, Fig. 4.10 and Fig. 4.11. Only clusters with *permutation corrected* p-value less than 0.01 are listed. The pairs of compared groups are detailed on the furthest left column (see legend for details). Note that the interpretation of results might be limited to the dataset.

Group difference and t-value maps are visualized in Fig. 4.10 for HCM patients and in Fig. 4.9 for AMI patients. As can be observed in Fig. 4.9, most patients did not display myocardial loss due to AMI. Myocardial loss (wall thinning) may present itself after the AMI event as a chronic consequence of the lesion (Dymarkowski et al., 2005). Instead, a high percentage of the patients in this database developed a localized mild hypertrophy

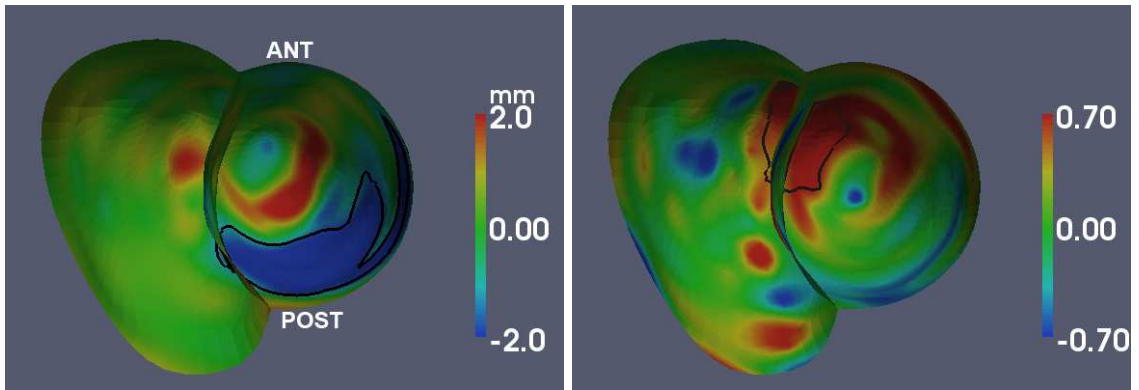


Figure 4.8: The abnormal thickness (left) and thickening (right) regions for a patient are depicted with contours on the difference maps of the normal group mean and this patient (patient minus the average of normal group).

along the septum and the anterolateral wall (cluster S1 and S2). Manual examination provided by an expert clinician supports these findings. Indeed most of the patients found in clinical practice are affected by several conditions. The localization of these two clusters suggest an overload condition of the LV (i.e. high blood pressure or aortic stenosis) (Bogaert and Taylor, 2005) is common for the patients in the dataset. For the group of HCM patients, meaning patients whose main pathological condition is hypertrophy, we observed an increased wall thickness over all the LV walls. This uniformly distributed (concentric) pattern of hypertrophy is one of the most commonly found (Bogaert and Taylor, 2005).

The group difference and t-value maps of the wall thickening are displayed in Fig. 4.11 for AMI group. The M1 cluster is related to the prevalent infarcted areas of this population since an infarcted area will display reduced contractility. Most infarctions appear to be located at the anterolateral wall at basal and mid-ventricular level. The inferior wall is affected more on the apical segments. No significant thickening cluster is found for HCM group.

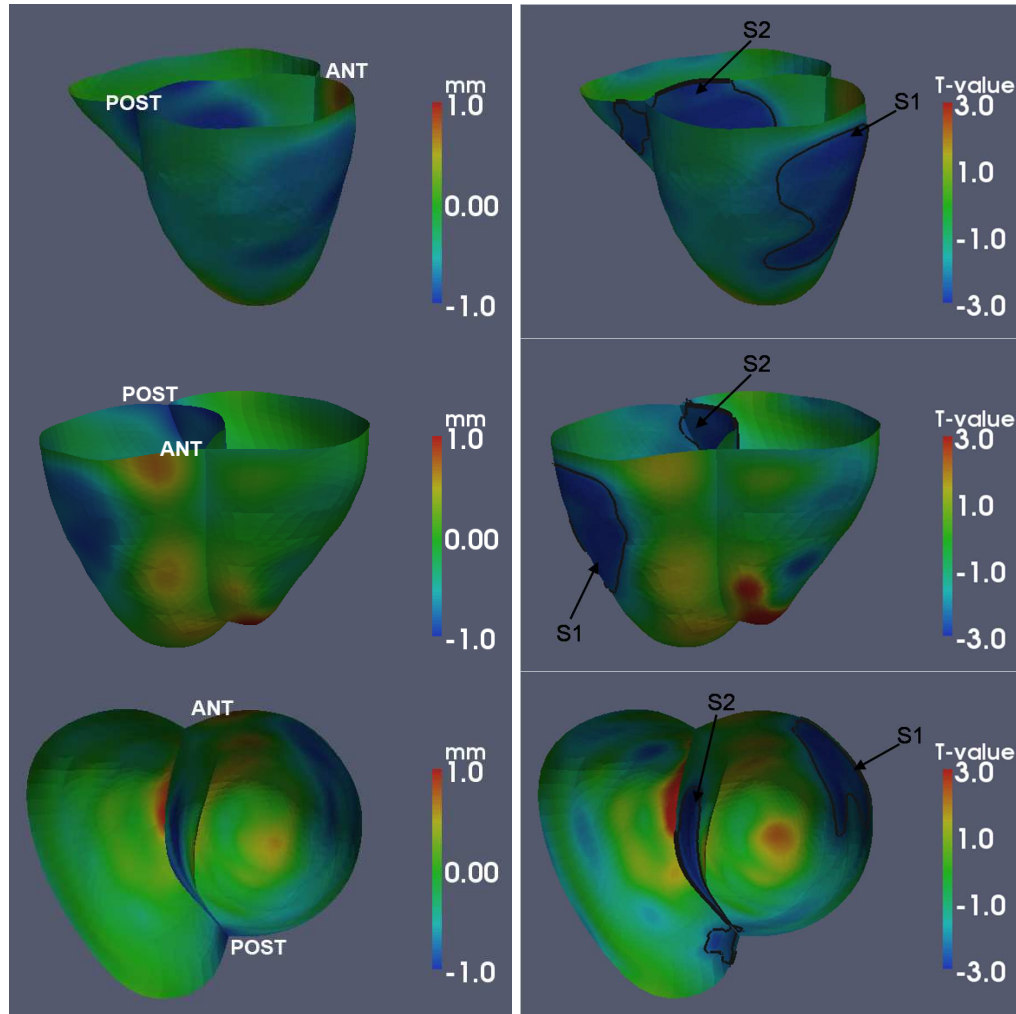


Figure 4.9: Thickness differences between the healthy heart group (28 subjects) and the acute myocardial infarction group (38 subjects). The left column shows the average group difference (healthy group minus AMI group) whereas the right column shows the corresponding t-statistic map. Significant clusters of group difference are depicted with contours on the t-maps, and are also listed in Table 4.2. Different rows are shown from different viewpoints.

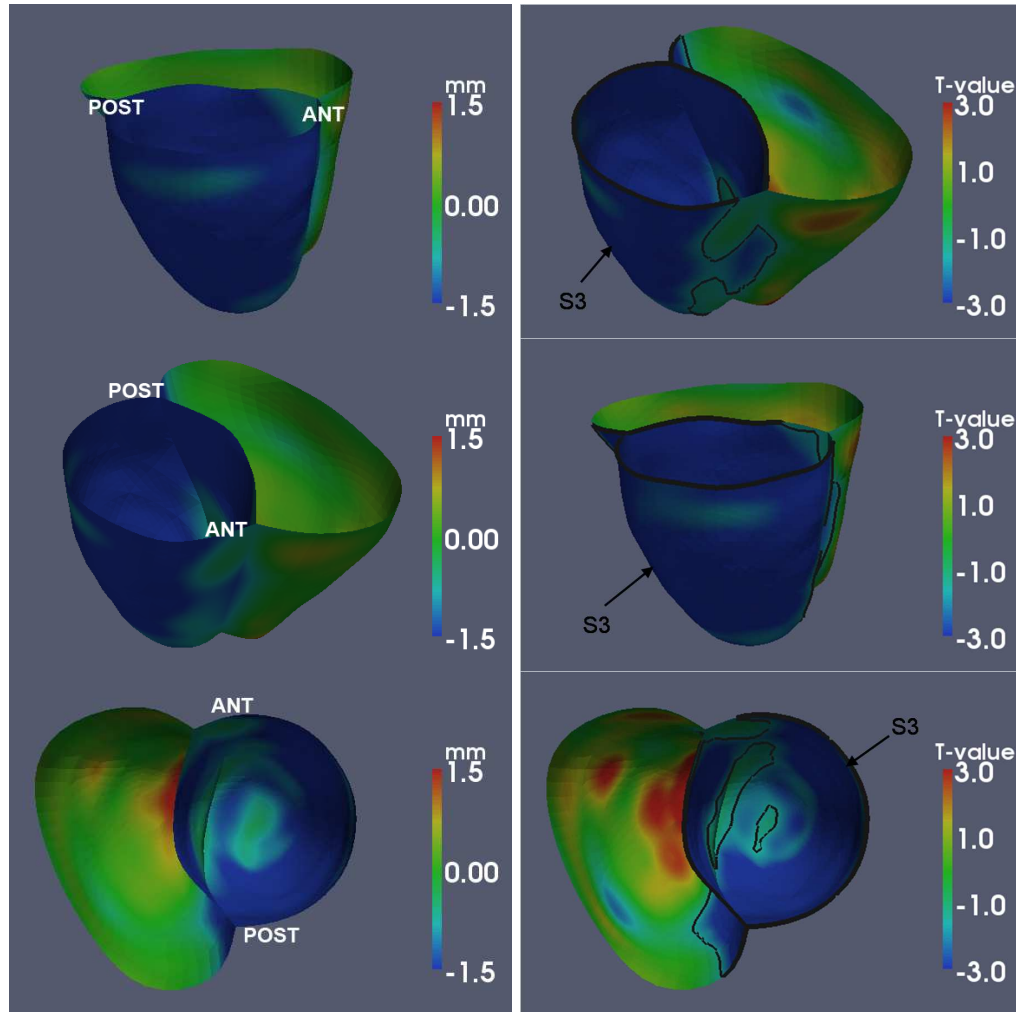


Figure 4.10: Thickness differences between the healthy heart group (28 subjects) and the hypertrophic cardiomyopathy group (7 subjects). The left column shows the average group difference (healthy group minus HCM group) whereas the right column shows the corresponding t-statistic map. Significant clusters of group difference are depicted with contours on the t-maps, and are also listed in Table 4.2. Different rows are shown from different viewpoints.

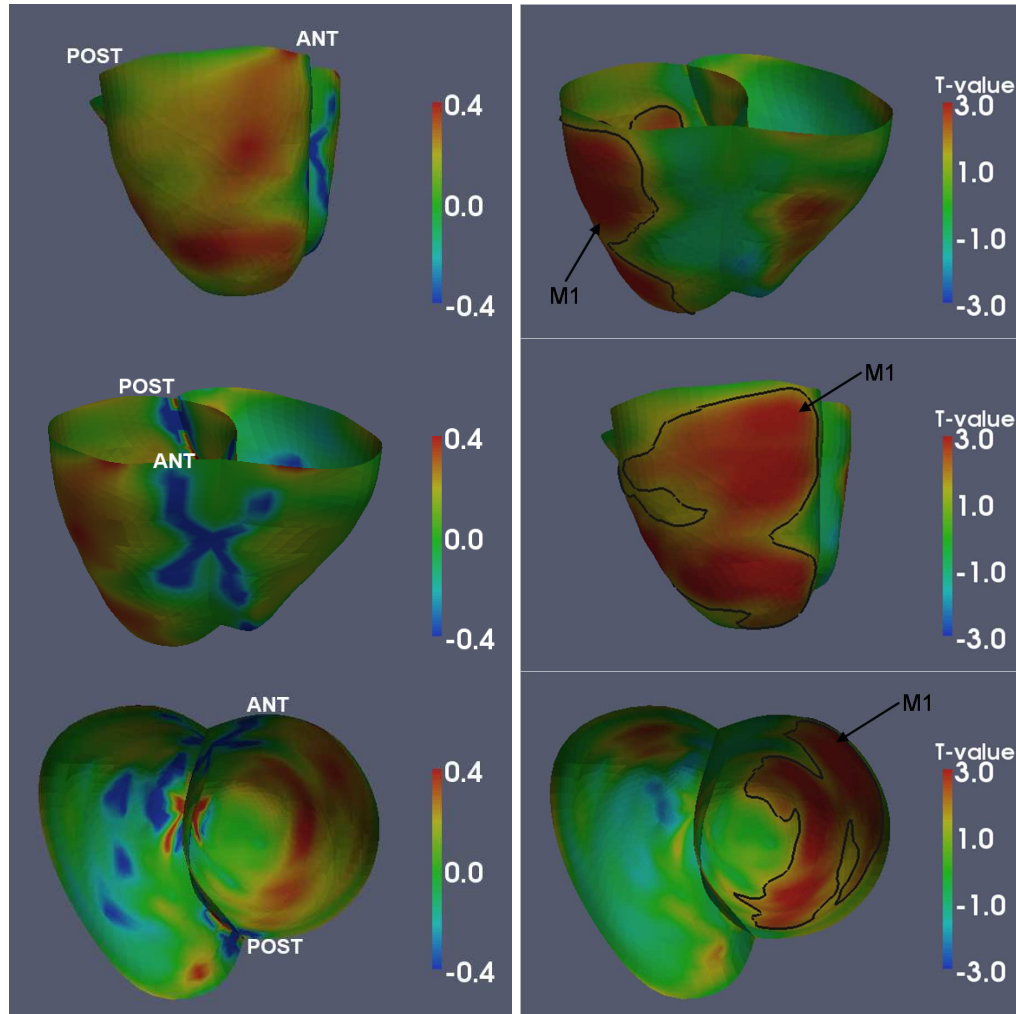


Figure 4.11: Systolic thickening differences between the healthy heart group (28 subjects) and the acute myocardial infarction group (38 subjects). The left column shows the average group difference (healthy group minus AMI group) whereas the right column shows the corresponding t-statistic map. Significant clusters of group difference are depicted with contours on the t-maps, and are also listed in Table 4.2. Different rows are shown from different viewpoints.

Table 4.2: Table enumerating clusters of significant differences in thickness and thickening between different pairs of subject groups, as defined in column 1. Column 1 also gives information of which group has a greater thickness/thickening for the particular cluster. Cluster mass is the integral of $|t|$ over the cluster. Every cluster is defined as a connected region with a $p < p_0$. p_{corr} is the FWER-corrected p-value of the cluster.

Thickness clusters				
Group contrast	cluster	cluster mass	p_0	p_{corr}
Normal < AMI	S1	3942.6	0.01	0.005
Normal < AMI	S2	4600.7	0.01	0.002
Normal < HCM	S3	38120.4	0.05	0.001
Thickening clusters				
Normal > AMI	M1	10608.8	0.05	0.001

4.4 Discussion and Conclusion

In this chapter a new branching medial model has been presented to extend the continuous medial model to complex shapes with multi-figures. This approach allows us to model a much larger class of shapes using continuous medial representation, which not only provides rich descriptive shape features, but also parameterizes the entire model interior, setting up a framework to perform a combined statistical analysis of shape and appearance.

Regarding the ways to define thickness, there are several other possibilities which are all based on the medial axis. One way is to define thickness based on the SLS. For sheet-like structures, the SLS thickness is about (but less than) twice of the Blum thickness. SLS thickness might be more analogous to the clinical practice which identifies pairs of boundary points and measures the point distance. However, a subset of points on the boundary - the points belonging to multiple *figures*, or in another words, the boundary points generated by points on medial seam curves - will have more than one SLS thickness measure, one for each *figure*. There's yet another way to define thickness in literature. In the "centersurface method" (Bolson and Sheehan, 1993), the thickness is defined as the length of the line segment that is orthogonal to the skeleton and lies between the boundary surfaces. This defines the thickness as the distance from the boundary to the skeleton, as opposed to skeleton to the boundary in the Blum thickness. However, there is

neither guarantee that each orthogonal line only cuts into the boundary exactly twice nor proof of how many times each point on the boundary can be hit by such orthogonal lines. Shape features other than wall thickness, like the Mean and Gaussian Curvatures of the endocardium/epicardium/medial surfaces, are not explored in this study. But they might also be useful in characterizing certain pathologies.

The medial modeling is particularly useful for population-wise comparison and analysis. Comparing with deterministic skeletonization, which yields discrete surfaces with uncertain number of vertices and uncertain number of branches that are sensitive to noise on the boundary, the medial model produces a robust approximation to the medial axis with consistent branching configuration and consistent surface representation. This simple and robust representation of the medial manifolds allows population-wise study and is also useful for visualization of statistical results.

We also demonstrate a statistical scheme to analyze the ventricular thickness and thickening maps. Derived from the medial model, the ventricular thickness and thickening maps were used for statistical studies on a data set consisting of HCM patients, AMI patients and subjects with no pathology in the heart. The statistics of the healthy heart group is used to identify regions with abnormal thickness or thickening in a patient. Cluster-based analysis reveals the prevalent patterns of thickness and thickening change for AMI and HCM patients in this dataset. The statistical studies yield information that can potentially be helpful for diagnosis and treatment.

Chapter 5

Model-Based Segmentation using Statistical Medial Model

This chapter presents a novel approach for the automatic segmentation of the myocardium in short-axis MRI. The method uses the branching medial model proposed in Chapter 4, whose ability to explicitly represent the thickness of objects is leveraged to construct a Markovian prior on myocardial thickness. This thickness prior is combined with the best practices from the ASM literature, such as a global shape prior, statistical modeling of appearance, and the use of local search to guide model deformation, all of which are adapted to the medial model. The performance of the segmentation method is evaluated by comparing to manual segmentation in a heterogeneous adult MRI dataset. The results show that the proposed method can provide a robust and accurate segmentation with overall mean point-to-surface error $1.0 (\pm 0.21)$ mm for the endo- and epicardial surfaces of the left and right ventricles. The left ventricle volume differences between the manual measurement and model-based estimation (manual-model) is in the range of $-6.2 \sim 13.8$ ml. The model also automatically provides a thickness estimation for the myocardium being segmented. The mean absolute estimation error of the mean thickness for the left ventricular wall, the interventricular septal wall and the right ventricular wall is $0.47 (\pm 0.36)$ mm, $0.53 (\pm 0.38)$ mm and $0.66 (\pm 0.31)$ mm respectively.

The research described in this chapter was done in collaboration with Dr. Hongzhi Wang and Dr. Paul A. Yushkevich at University of Pennsylvania and with Dr. Alejandro F. Frangi, Dr. Federico Sukno and Catalina Tobon Gomez at University of Pompeu Fabra, who together contributed to every facet of the work.

5.1 Introduction

Automatic segmentation of the human heart in *in vivo* imaging data is one of the persistent challenges in biomedical imaging analysis. Segmentation is a necessary step for virtually any subsequent analysis of heart structure and function. Statistical shape models are widely used to segment cardiac images, since the model-based segmentation approaches are usually more robust than low-level algorithms given they contain information about the expected shape and appearance of the structure of interest. Probably the most generic and, at the same time, the most popular way for a model to represent a shape is by representing its boundaries. A large number of studies on cardiac segmentation have been conducted using boundary models (Lotjonen et al., 2004; Assen et al., 2006; Lorenz and von Berg, 2006; Zheng et al., 2008; Wierzbicki et al., 2008; Peters et al., 2009). In this chapter, however, I would like to investigate the feasibility of using the *statistical medial model* in cardiac segmentation.

The medial models, have been used successfully for several biomedical image segmentation tasks, such as hippocampus and kidney segmentation (Pizer et al., 2001; Joshi et al., 2002). However, to the best of my knowledge, this is the first approach to use deformable medial models for myocardium segmentation. An important property of the medial model is that it can represent and control thickness explicitly. This can be particularly helpful during the segmentation of thin, sheet-like structures, such as the myocardium. The benefits of regulating the thickness during the myocardium segmentation have been explored in (Zeng et al., 1998; Paragios, 2002; Jolly et al., 2009). In this chapter, I segment the myocardium of both left and right ventricles with a Markovian prior on myocardial thickness.

Most existing cardiac segmentation approaches, even those dealing with 4-chambers such as (Zheng et al., 2008; Wierzbicki et al., 2008; Peters et al., 2009; Zhuang et al., 2008), conventionally only segment the myocardium of the left ventricle, which is relatively thick. For the right ventricle, most authors (Zheng et al., 2008; Peters et al., 2009; Zhuang et al., 2008) only model the endocardial surface. Wierzbicki et al. (Wierzbicki et al., 2008), whose application is towards image-guided cardiac surgery, model the epicardium of the right ventricle but leave the endocardium unattended. As we know, the myocardium of the right ventricle is also an important part of the heart and can be useful for characterizing a variety of pathologies, such as right ventricle hypertrophy, right ventricular infarction, and ventricular arrhythmias (Sheehan and Redington, 2008; Haddad et al., 2008). One reason that the right ventricular myocardium segmentation has been largely ignored might be due to the doubt about how reliable and useful the segmentation can be given the thinness of the structure and the limited resolution of the image. With the improvement of cardiac imaging, the interest on right ventricular myocardium segmentation is increasing. Another reason might lie in the limitation of the boundary model itself. In order to use a boundary model to segment the thin layer of right ventricular myocardium, particular care needs to be taken to prevent the epicardial and endocardial surfaces from intersecting or folding into each other. With the medial model, the folding would not be a problem since the thickness should be always positive. And even better, the segmentation might further benefit from an explicit thickness prior. In this chapter, I conduct the model-based biventricular myocardium segmentation, compare its agreement with manual segmentation, and assess its ability to estimate myocardium thickness.

In this work, a single medial model is used to represent the shape of both left and right ventricles. The model is first adapted to segmented binary volumes in the training data and the shape priors are constructed based on the medial shape features. The local appearance model is also constructed for each boundary position by utilizing the Adaptive Boosting (AdaBoost) algorithm (Freund and Schapire, 1997) to pick and combine weak classifiers to build a strong one. Then the medial model is adapted to unseen cardiac images under

the guidance of the boundary detection results and under the regularization of the shape priors to achieve model-based segmentation.

The rest of the chapter is organized as follows. The medial model and shape priors are introduced in Section 5.2 and the appearance model is introduced in Section 5.3. Section 5.4 reviews the overall segmentation algorithm. In Section 5.5 the experimental results are reported. The comparison with literature, the correspondence problem, the limitations and plans for future research are discussed in Section 5.6. Section 5.7 concludes the chapter.

5.2 Shape Priors

To fit the model to unseen image data, I still use the same Bayesian framework as I used in the binary image adaptation, but change the definition of the likelihood term and add additional shape priors terms. I will discuss the new likelihood term in Section 5.4. In this section I deal with the shape prior terms.

The medial model has two types of parameters: the parameters \mathbf{m} to describe the medial surfaces, which in my implementation are the x, y, and z coordinates of the medial control points, and the parameters R to describe the associated radial thickness. Variability in medial surface shape is modeled using a multivariate Gaussian distribution: PCA is applied to \mathbf{m} . Before PCA, Generalized Procrustes Analysis (Gower, 1975) is applied to \mathbf{m} to factor out the differences in scaling, rotation, and rigid motion. The number of PCA modes c is chosen to capture 95% of total variability. During the segmentation algorithm, to calculate the probability of \mathbf{m} given the PCA model, I first apply Generalized Procrustes Analysis to align it with the PCA mean $\bar{\mathbf{m}}$. Then the aligned \mathbf{m}' is projected onto the PCA space to obtain the coefficients b_i . Since there are always variation that cannot be fully captured by PCA, I allow a residual but regularize it to be within a reasonable range:

$$-\log(p(\mathbf{m}; \bar{\mathbf{m}}, \lambda_1, \dots, \lambda_c, \mathbf{v}_1, \dots, \mathbf{v}_c)) \sim \sum_{i=1}^c \frac{b_i^2}{\lambda_i} + \alpha \|\mathbf{m}' - \mathbf{m}'_{PCA}\|^2, \quad (5.1)$$

where \mathbf{v}_i, λ_i are the eigenvector and eigenvalue of the PCA covariance matrix, \mathbf{m}'_{PCA} is the reconstructed model parameter using the projected the PCA coefficients b_i . Thickness variability is modeled by a more localized Gibbs distribution (i.e., thickness is treated as a Markov random Field):

$$-\log(p(R_1, \dots, R_N; \mu_\bullet, \sigma_\bullet)) \sim \sum_{i=1}^N \frac{(R_i - \mu_i)^2}{\sigma_i^2} + \beta \sum_{(j,k) \in E} \frac{(|R_j - R_k| - \mu_{jk})^2}{\sigma_{jk}^2}, \quad (5.2)$$

where $i = 1, \dots, N$ indexes vertices in the medial surface, E is the set of all edges of the triangle mesh, and $\{\mu_i, \sigma_i, \mu_{jk}, \sigma_{jk}\}$ are parameters estimated from the training data.

The reason I use different priors for \mathbf{m} and R stems from the fact that thickness varies much more smoothly than the x, y, and z coordinates of the medial surface. Thus, the MRF is an appropriate model for thickness, but it is too restrictive for shape. I performed experiments that show that using PCA for both \mathbf{m} and R leads to worse segmentation performance than using PCA for \mathbf{m} and MRF for R .

5.3 Appearance Model and Boundary Detection

In the popular ASM approach, texture features are sampled around the boundary landmarks along the direction perpendicular to the model boundary. In the original version of the ASM (Cootes et al., 1995), appearance features are modeled using PCA, extracting a mean feature vector and principal modes of variations for each landmark. Later, ASM was adapted to various segmentation tasks in the biomedical image field, during which different appearance features have been explored, and different ways for constructing the appearance model out of the features have been proposed. Commonly used appearance features include image intensity values, their derivatives, Haar wavelets, Gabor wavelets (Daugman, 1988; McKenna et al., 1997), and steerable features (Freeman and Adelson, 1991). During the model-based segmentation, ASM searches along the directions perpendicular to the boundary to locate new boundary landmarks. This is usually achieved by

evaluating a designed match function that is supposed to achieve maximum at the boundary. The match function can be Mahalanobis distance, a gradient-based edge detector, a k-nearest-neighbor (kNN) classifier (de Bruijne et al., 2003), or other discriminative training-based classifiers (Zheng et al., 2008).

The AdaBoost algorithm (Freund and Schapire, 1997), which provides a way to select and combine different features from a potentially large feature pool to build a strong classifier, is used in this work. AdaBoost has been used in several image segmentation applications. For example, Morra et al. (Morra et al., 2010) show that AdaBoost can automatically select good features for hippocampus segmentation. In this application, AdaBoost algorithm is used to help construct local appearance models which are used to drive image segmentation, as illustrated by Figure 5.1. Below I describe the appearance model in detail.

5.3.1 AdaBoost Training and Classification

At each vertex in the medial model, I build a model of local appearance, which is subsequently used to drive image segmentation. Recall that for most medial pseudo-landmarks there are two corresponding boundary nodes, one on each side. At these two nodes, the maximal inscribed ball which centers at the medial pseudo-landmark is tangent to the model boundary. The exceptions are the medial pseudo-landmarks on the branching curves at the two ends of the interventricular septum, which have three corresponding boundary nodes. The *triple tangency* branching points are treated as the limit case, where three *bitangency* points meet together. Each one of these three bitangency points belongs to one branch of the medial axis and is treated normally during the training and boundary detection. After boundary detection, the triple tangency medial pseudo-landmark and the radius will be updated as the average of the three independent bitangency detection results. Below I only deal with bitangency cases.

At each boundary node, I train an AdaBoost classifier to discriminate between a “well-placed” boundary node and a “misplaced” boundary node, as illustrated in Figure 5.3. A

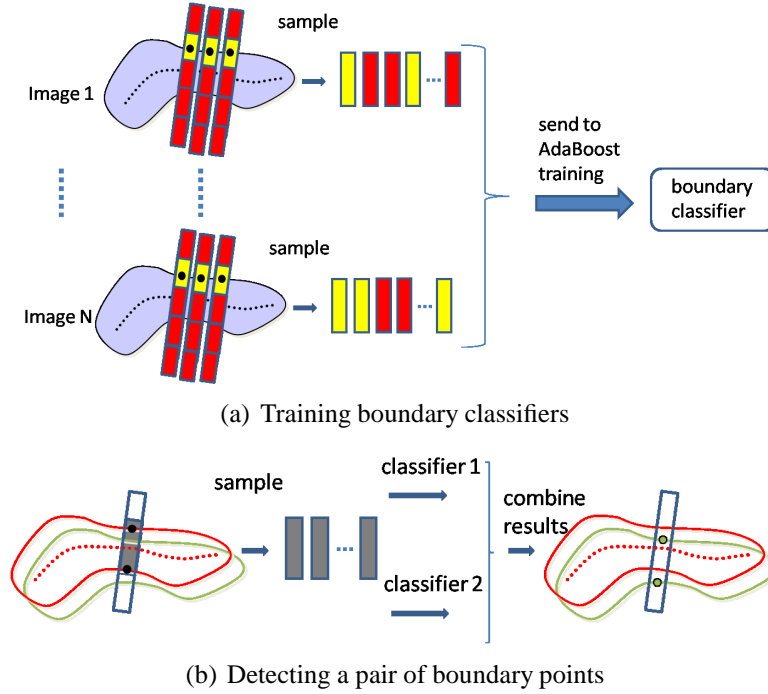


Figure 5.1: Illustration of appearance matching using the AdaBoost classifier. (a). The classifier is trained to differentiate between boundary nodes located at the correct anatomical boundary and displaced boundary nodes. In the figure, the yellow bars show samples drawn from correct anatomical boundary, while the red bars are samples that are displaced. During training, each boundary node is displaced along the *chord direction* (illustrated in Figure 5.2), and samples from the image neighborhood are used to generate appearance features. Combining features from different subjects, at each boundary node, I train an AdaBoost classifier with two classes (displaced node vs. not displaced). (b). The deformable model is shown in red color while the underlying object is shown in green color. During segmentation, the classifier is used to position boundary nodes close to anatomical boundaries. Pairs of boundary nodes that share a medial pseudo-landmark are displaced along the chord direction, governed by the AdaBoost classifiers corresponding to the nodes. Following these displacements, the deformable model is updated so as to satisfy the necessary geometric constraints and to abide by the shape priors.

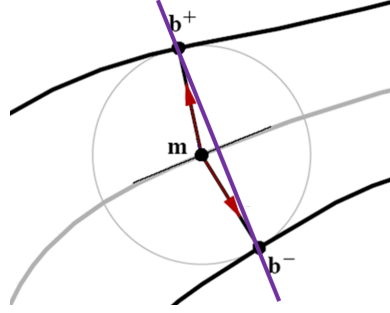


Figure 5.2: Illustration of chord direction. For boundary nodes \mathbf{b}^{\pm} which correspond to the medial pseudo-landmark \mathbf{m} , the chord direction which crosses \mathbf{b}^+ and \mathbf{b}^- shown as purple line in the figure.

well-placed boundary node lies within a certain distance to the corresponding anatomical boundary in the training image, and a misplaced boundary node lies some distance away from the anatomical boundary, as illustrated in Figure 5.3. Well-placed boundary nodes are obtained by fitting models to manual segmentations of the myocardium in the training data. Misplaced boundary nodes are obtained by applying displacements to the well-placed boundary nodes along the direction between the two corresponding boundary nodes. This displacement direction, called *chord direction* since it is a chord of the MIB, is illustrated in Figure 5.2. Therefore training exemplars for each classifier include well-placed and misplaced versions of a given boundary node across all subjects included in the training subset. To further increase the number of training exemplars and make classifiers less sensitive to location, I include, as training exemplars for each classifier, misplaced and well-placed versions of the boundary nodes in the two-ring neighborhood of the boundary node associated with the classifier.

During local boundary detection, each sample corresponding to a pseudo-landmark go through two classifiers, one for each of the two corresponding boundary nodes. According to the classification scores, a pair of points satisfying the following conditions is selected to be the new candidates of boundary nodes: (1) they are classified as correct boundary nodes according to the two classifiers respectively; (2) their order is consistent with the right order of the boundary nodes (otherwise the boundaries would intersect); and (3) the

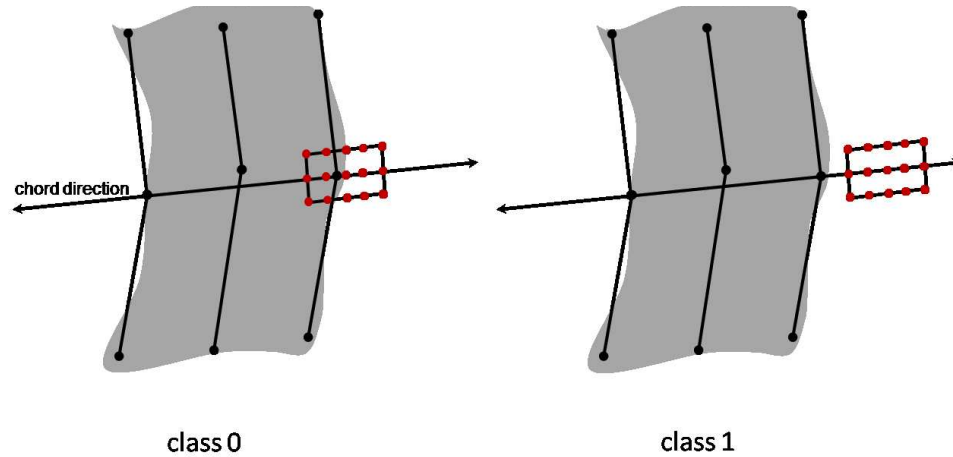


Figure 5.3: Illustration of training exemplars of a “well-placed” boundary node (class 0) and a “misplaced” boundary node (class 1) in AdaBoost training. The manual segmentation of the anatomical structure is shown in gray. The medial model is fitted to the manual segmentation to obtain medial pseudo-landmarks and corresponding boundary points. The left figure shows a “well-placed” boundary node centered at the exact boundary of the manual segmentation. Note that since the manual segmentation can not be perfect, I actually place three “well-placed” boundary nodes for each boundary location: one is on the exact boundary of the manual segmentation as illustrated in the left figure, the other two are on two sides of the first one and are obtained by applying a small displacement to it along the chord direction. The right figure shows a “misplaced” boundary nodes, which is obtained by applying displacements to the well-placed boundary nodes along chord direction.

overall classification score is the highest for all pairs satisfying condition (1) and (2). If no such pair can be located for a particular medial pseudo-landmark, the local boundary detection algorithm will return a void result for this medial pseudo-landmark.

5.3.2 Features of AdaBoost

A rich set of features is used to build these AdaBoost classifiers.

First, for each MRI slice, I compute a set of texture descriptors at different scales, which are called *irreducible Cartesian differential invariants* (Schmid and Mohr, 1997; Walker et al., 1997; Sukno et al., 2007). Using Einstein notation, with L denoting image derivative in direction $i \in \{x, y\}$, these descriptors are given by L , $L_i L_i$, L_{ii} , $L_i L_{ij} L_j$, and $L_{ij} L_{ji}$. The Cartesian differential invariants are invariant to rigid transformations. The term *irreducible* means that any other algebraic invariant can be reduced to a linear combination of elements of this minimal set.

These texture descriptors are sampled around each boundary node using a cylindrical sampling grid oriented along the chord direction. A 2D illustration is in Figure 5.3. The axis of the cylinder lies along the *chord direction*. On the cross-section of the cylinder, grid points are put both at the center of the circle and on the boundary of the circle. Assume that there are X_c points on the boundary of the circle on each cross-section, and along the axis of the cylinder there are Y_c cross-sections being sampled. Each sample will have $(X_c + 1) \times Y_c$ points.

Linear interpolation is used to sample texture descriptors between slices. Thousands of features are obtained for each boundary node. For each feature, a simple threshold-based weak classifier is constructed. AdaBoost is used to combine these weak classifiers into a single strong classifier.

5.4 Segmentation Algorithm

The current model uses landmark-based initialization. The user manually selects six landmarks, including the LV apex point and five points at the most basal slice. Based on these landmarks, a similarity transformation is determined, which places the model in the image and serves as the initialization. Subsequently, the model is deformed by iteratively applying two steps: *local search* and *Bayesian deformation*. Both of these steps are adaptations of the segmentation algorithm used in active shape models (Cootes et al., 1995), and I only summarize them here.

In the local search step, AdaBoost classifiers are used to find new candidate positions for boundary nodes, as described above in Section 5.3. If a pair of new boundary candidates can be located for a medial pseudo-landmark, I can compute a new medial pseudo-landmark and radius by assuming that the angles between the *chord direction* and the *radial directions* (the vectors starting from the medial pseudo-landmark and pointing to the corresponding boundary points) stay the same. Let's assume that in a previous state the medial pseudo-landmark and radius are (\mathbf{m}, R) and that the corresponding boundary points are $(\mathbf{b}^+, \mathbf{b}^-)$, while in candidate model state after local boundary detection we have new boundary candidates $(\hat{\mathbf{b}}^+, \hat{\mathbf{b}}^-)$. Then the new medial pseudo-landmark and radius $(\hat{\mathbf{m}}, \hat{R})$ are

$$\hat{\mathbf{m}} = \hat{\mathbf{b}}^+ + (\mathbf{m} - \mathbf{b}^+) \cdot \frac{|\hat{\mathbf{b}}^+ - \hat{\mathbf{b}}^-|}{|\mathbf{b}^+ - \mathbf{b}^-|}, \quad (5.3)$$

$$\hat{R} = R \cdot \frac{|\hat{\mathbf{b}}^+ - \hat{\mathbf{b}}^-|}{|\mathbf{b}^+ - \mathbf{b}^-|} \quad (5.4)$$

Following local boundary detection, the medial model will no longer be in a valid state, as the equality medial constraints will surely be violated. Likewise, the model is likely to adhere poorly to the shape prior defined in Section 5.2. To address this, I fit the deformable medial model to the new candidate medial pseudo-landmarks $(\hat{\mathbf{m}}, \hat{R})$ using Bayesian maximum a posteriori estimation, with likelihood given by the distance from the deformable model nodes to the candidate medial pseudo-landmarks, and the prior terms

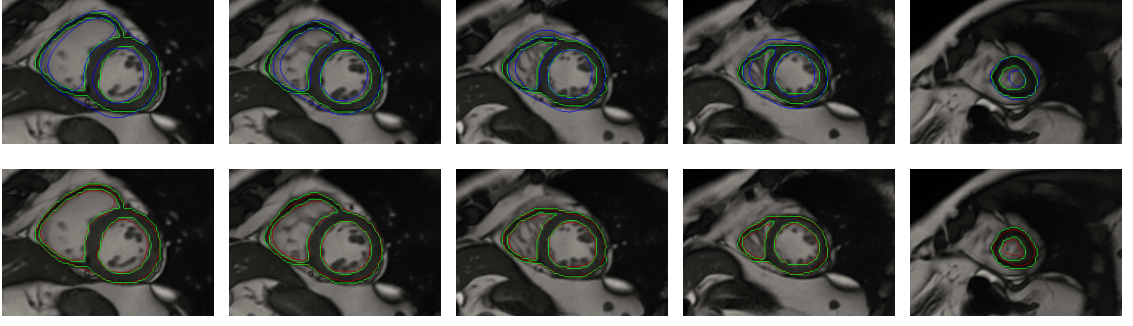


Figure 5.4: Example of automatic segmentation in a single subject. The top row shows the manual segmentation in green and the model initialized by landmarks in blue. The bottom row shows the segmentation result in red, with manual segmentation in green. From left to right, slices progress from most basal slice to the apex.

to ensure the validity and regularity of the medial model. To compute this likelihood term, I calculate the values of medial pseudo-landmarks and the radii from the model, denoting them as (\mathbf{m}_m, R_m) , and define the distance to the candidates $(\hat{\mathbf{m}}, \hat{R})$ as

$$d = \sum_{i=1}^N [|\hat{\mathbf{m}} - \mathbf{m}_m|^2 + (\hat{R} - R_m)^2].$$

This likelihood treats \mathbf{m} and R as having the same units, which has not been a problem in practice. A likelihood term based on Mahalanobis distance could also be used as an alternative. The prior term of the Bayesian model contains the terms used in the binary segmentation adaptation and the shape prior terms as defined in Equation (5.1) and (5.2).

This procedure of local boundary detection followed by global model adaptation is repeated iteratively. Experiments show that the deformable model converges within a few iterations. I adjust the relative weights of the priors to enforce a strong shape constraints at the beginning, when the model is likely to be far from the true segmentation, and relax the shape constraints towards the end to allow the model more freedom to follow the boundary detection results.

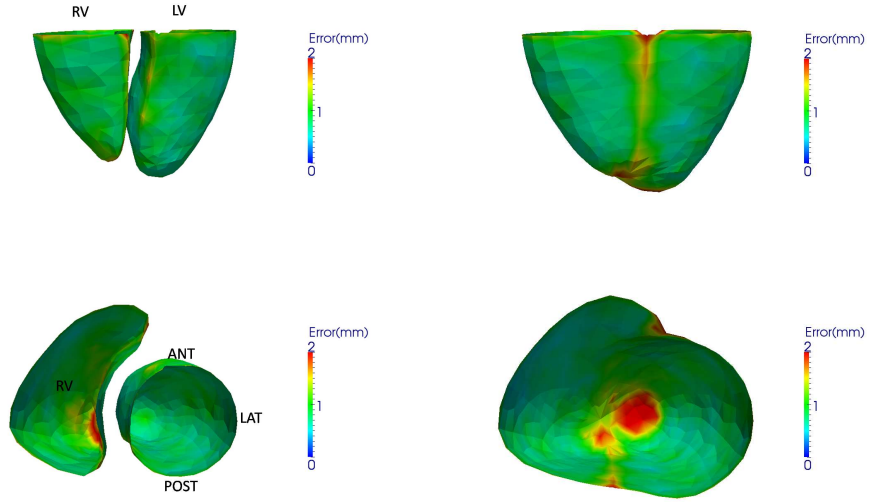


Figure 5.5: Illustrate the mean segmentation error. The meshes are colored by the mean point-to-surface distance from the model boundary mesh to the manual segmentation boundary mesh. The left figures show the endocardial boundary of the left and right ventricles. The right figures show the epicardial boundary of the left and right ventricles. The top row and bottom row are figures from different view point.

5.5 Experiments

5.5.1 Data Set

Two data sets are used in the experiments. The first data set (DB1) contains 81 manually segmented short-axis cardiac MRI volumes in the end diastole phase from both healthy subjects and patients suffering from common cardiovascular pathologies, including myocardial infarction (25), hypertrophy (21), LV dilation (6), LV aneurysm (2), RV dilation (2), LA dilation (5), RA dilation (2), and pericarditis (4). The MR images were generously provided to us by CETIR Sant Jordi Centre (Barcelona, Spain). The expert segmentations were manually drawn on the endocardial left ventricle and right ventricle borders, and on the epicardial border of the left and right ventricles to construct a 2-chamber heart model that typically spans 8-12 slices from the base to the apex.

The second data set (DB2) contains 40 short-axis cardiac MR studies from 4 different groups: healthy (10), myocardial infarction (MI) (10), hypertrophy (10) and dilated cardiomyopathy (DCM) (10). Hui Sun, an author, manually segmented the endocardial and epicardial surfaces of the ventricles using ITK-SNAP (Yushkevich et al., 2006a) (www.itksnap.org). The segmentation is reviewed by Catalina Tobon-Gomez, another author and also a trained expert, to ensure the quality.

The acquisition parameters of both datasets are: TR/TE=2.9/1.2 ms, flip angle=45°, in-slice resolution = 1.5625 mm \times 1.5625 mm, slice thickness= 8 mm, slice separation= 0 mm, field of view= 400 mm \times 340 mm, on a General Electric Signa CVi-HDx 1.5T scanner (GE Healthcare, Milwaukee, USA).

5.5.2 Experimental Design

The DB1, which consists of 81 manual segmentations, is only used for medial template building and shape prior training. The DB2, which consists of 40 images and their manual segmentations, is used for training appearance models and evaluating the segmentation performance through cross-validation experiments. In each round of cross-validation, the appearance model is built on a subset of 24 images (6 images from each subgroup) and the segmentation results are evaluated on the remaining 16 images. Cross-validation is repeated 10 times (the AdaBoost training is time-consuming and precludes us from doing a much larger number of cross-validation experiments) and the average results on the 160 segmentations are reported. The results for each group are also reported separately to study the influence of different heart conditions on automatic segmentation.

5.5.3 Initialization Error Tests

To evaluate the influence of initialization on this segmentation approach, the cross-validation experiment is performed four times. In these experiments, Gaussian noises are added to the x, y, and z coordinates of the true landmark positions to enlarge the initialization error.

Table 5.1: Initialization error tests. The errors (\pm standard deviation) are point-to-mesh distances with the manual segmentation meshes. Here LV/RV indicate the endocardial surface of the left/right ventricle, while EPI means the epicardial surface of both left and right ventricles.

Noise		LV(mm)	RV(mm)	EPI(mm)
N(0,0)	Initialization Error	4.51 ± 1.19	4.44 ± 1.35	3.95 ± 0.84
	Final Error	0.87 ± 0.23	1.19 ± 0.28	0.98 ± 0.23
N(0,1)	Initialization Error	4.58 ± 1.22	4.43 ± 1.38	4.00 ± 0.85
	Final Error	0.87 ± 0.22	1.19 ± 0.28	0.98 ± 0.24
N(0,5)	Initialization Error	5.22 ± 1.64	4.99 ± 1.95	4.85 ± 1.54
	Final Error	0.92 ± 0.28	1.25 ± 0.32	1.02 ± 0.27
N(0,10)	Initialization Error	6.66 ± 2.73	6.13 ± 2.91	6.48 ± 2.80
	Final Error	1.26 ± 1.32	1.71 ± 1.50	1.54 ± 1.77

The Gaussian noises added in the four experiments have zero means and their standard deviations are 0mm, 1mm, 5mm, and 10mm. The initialization error and the final error are summarized in Table 5.1. The boundary delineation errors are measured by the widely used point-to-mesh distance (Assen et al., 2006; Zheng et al., 2008). For each point on the mesh, the closest point (not necessarily mesh triangle vertices) on the other mesh is located and the Euclidean distance between these two points is calculated. This distance is computed for each point on the mesh and the weighted average (according to the area) defines the point-to-mesh distance to the other mesh. The distance is calculated from model-based segmentation mesh to the ground-truth and vice versa to make the measurement symmetric.

Table 5.1 lists the results separately for: the endocardial surface of the left ventricle (LV), the endocardial surface of the right ventricle (RV), the epicardial surface for both left and right ventricles (EPI). The initialization error and the final error increases with the added inaccuracy. When the noise goes up $N(0, 10)$, the result becomes less stable although the average final error is still reasonable.

Table 5.2: The mean point to mesh errors (\pm standard deviation) between the manual segmentation meshes and model-based segmentation meshes based on cross-validation. Here LV/RV indicate the endocardial surface of the left/right ventricle, while EPI means the epicardial surface of both left and right ventricles.

	LV(mm)	RV(mm)	EPI(mm)	Whole mesh(mm)
healthy	0.78 ± 0.13	1.07 ± 0.20	0.96 ± 0.20	0.94 ± 0.14
MI	0.94 ± 0.37	1.16 ± 0.34	1.06 ± 0.38	1.05 ± 0.36
DCM	0.88 ± 0.19	1.33 ± 0.29	0.97 ± 0.13	1.03 ± 0.12
hypertrophy	0.87 ± 0.15	1.19 ± 0.22	0.92 ± 0.12	0.97 ± 0.10
all	0.87 ± 0.23	1.19 ± 0.28	0.98 ± 0.23	1.00 ± 0.21

5.5.4 Boundary Delineation

Figure 5.4 shows an example of model-based segmentation. Figure 5.5 shows the distribution of the mean segmentation error on the boundary mesh. The boundary delineation errors based on the cross-validation described in Section 5.5.2 are summarized in Table 5.5.4. All the segmentation cases in the cross-validation experiments are included in the calculation. The table lists the results separately for: the endocardial surface of the left ventricle (LV), the endocardial surface of the right ventricle (RV), the epicardial surface for both left and right ventricles (EPI), and whole heart mesh (WM). The mean error for the whole mesh is $1.0 (\pm 0.21)$ mm. According to the results, the disease state, especially the MI, does slightly affect the performance of the model-based segmentation. However, results for all different groups are quite encouraging.

The Markovian prior on myocardial thickness helps to improve the result. Instead of using PCA for \mathbf{m} and MRF for R , if I use PCA for both \mathbf{m} and R , the mean point-to-mesh errors for the endocardial surface of the left ventricle, endocardial surface of the right ventricle, and epicardial surface for both left and right ventricles would go up to $0.95(\pm 0.28)$ mm, $1.24(\pm 0.51)$ mm and $1.07(\pm 0.32)$ mm.

Table 5.3: Error of the heart wall thickness estimation in medial models fitted directly to MRI images comparing with medial models fitted to manual segmentations.

	SEP Wall	LV Wall	RV Wall
Mean Absolute Error (mm)	0.53 ± 0.38	0.47 ± 0.36	0.66 ± 0.31
Bias (mm)	-0.35 ± 0.55	-0.41 ± 0.42	-0.65 ± 0.34
Error Range(mm)	$-1.74 \sim 1.37$	$-1.8 \sim 0.47$	$-1.60 \sim 0.31$

5.5.5 Thickness Measurements

The heart wall thickness is an important parameter to assess myocardial function. The medial model associates each point on the medial surface with the diameter of the maximal inscribed ball, which can serve as a thickness measure. Table 5.3 summaries the error of the mean thickness estimation. Note that although the mean point-to-surface distances for the endocardial and epicardial surface are around 1 mm, the mean absolute thickness errors are only within 0.47~0.66 mm. This might be a bonus of using statistical medial model which regularizes the thickness explicitly. However, there is a systematic bias in the thickness measure within -0.65~-0.35 mm. This could be due to the fact that the training data and testing data are segmented by different individuals that may have systematic different preferences.

5.5.6 Left Ventricular Volume

In this section I analyze the estimation of the left ventricular volume (LVV) based on the model segmentation. Table 5.4 summarizes the mean results. The accuracy of the LVV estimation was calculated as the percentage of absolute volume difference relative to true volume, or $1 - \text{abs}(\frac{LVV_{\text{model}} - LVV_{\text{manual}}}{LVV_{\text{manual}}})$. The accuracy is quite similar across different disease groups and the overall mean accuracy is 96.6 (± 2.4)%.

Agreement of LVV model-based measurements with manual measurements is further assessed by means of Bland-Altman plot (Bland and Altman, 1986) in Figure 5.6. The plot shows a slight underestimation of the LVV for model-based measurement with a mean bias

Table 5.4: The mean left ventricular volume (\pm standard deviation) through manual measurement and model-based estimation, as well as the mean accuracy of model-based estimation (\pm standard deviation)

	manual (ml)	model (ml)	accuracy(%)
healthy	83.1 ± 22.5	81.9 ± 22.2	96.4 ± 2.2
MI	104.4 ± 27.2	103.2 ± 27.6	96.9 ± 1.8
DCM	145.0 ± 33.4	140.2 ± 33.5	96.6 ± 3.3
hypertrophy	91.7 ± 22.0	88.7 ± 20.6	96.4 ± 2.1
all	106.0 ± 35.6	103.5 ± 34.6	0.966 ± 0.024

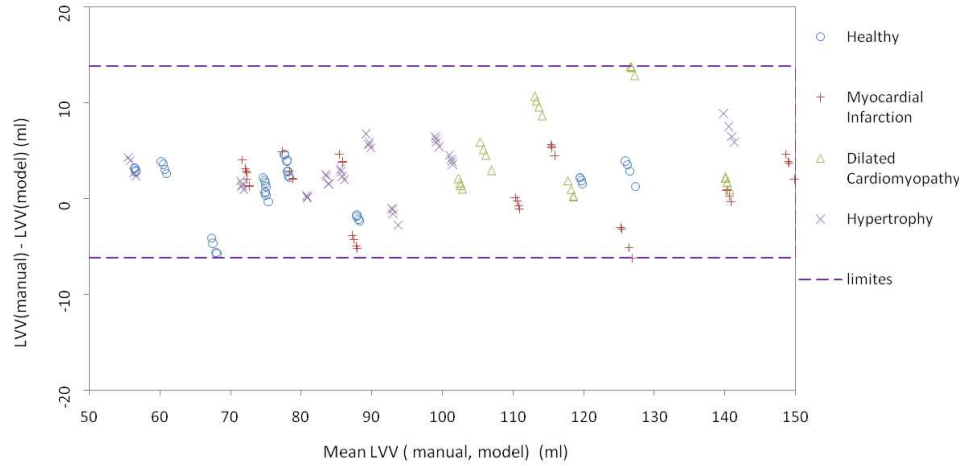


Figure 5.6: Bland-Altman plot for LVV comparing the manual measurement and model-based measurement.

of 2.6 ml. This might be caused by the overestimation of the heart wall. The volume differences between the manual measurement and model-based estimation (manual-model) is in the range of $-6.2 \sim 13.8$ ml. These values are very much within intraobserver variability (Bailly et al., 2008). The mean absolute error for LVV estimation is 3.5 ml.

5.5.7 Right Ventricular Volume

This section briefly analyze the estimation of the right ventricular volume (RVV) based on the model segmentation. Agreement of RVV model-based measurements with manual measurements is assessed by Bland-Altman plot in Figure 5.7. The plot shows a slight underestimation of the RVV for model-based measurement with a mean bias of 7.5 ml.

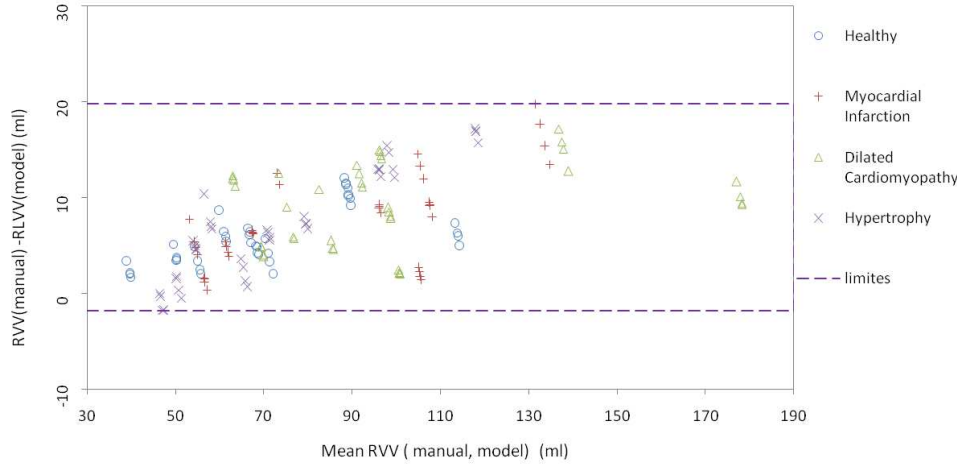


Figure 5.7: Bland-Altman plot for RVV comparing the manual measurement and model-based measurement.

The volume differences between the manual measurement and model-based estimation (manual-model) is in the range of : $-1.8 \sim 19.8$ ml. The mean absolute error for RVV estimation is 7.6 ml.

5.6 Discussion

5.6.1 Compare with Literatures

It is not easy to compare the heart segmentation errors from different papers since they use different model, different data sets and different error measures. Nevertheless, I summarizes them as much as I can in Table 5.5 for the segmentation of cardiac MR images reported in the literature. The error in this approach is the second smallest according to a direct comparison of boundary displacement error. Overall the paper by Peter et al. (Peters et al., 2009) gives the smallest error, but their image resolution is much better than images used in other papers, and only the endocardial surface is segmented for the right ventricle in their method.

Table 5.5: Errors (\pm standard deviation if applicable) reported in the literature for MR image segmentation.

	resolution (mm ³)	LV (mm)	RV (mm)	EPI (mm)
mittchell 02 (*)	1.56 \times 1.56 \times 9	2.75 \pm 0.86	-	2.63 \pm 0.76 (LV)
Lotjonen 04	1.0 \times 1.0 (+)	2.01 \pm 0.31	2.37 \pm 0.50	2.77 \pm 0.49 (LV+RV)
van Assen 08	1.5 \times 1.5 \times 10	1.72	-	1.55 (LV)
Zhuang 08	2 \times 2 \times 2	2.4 \pm 1.1	2.6 \pm 1.5	1.3 \pm 0.21 (LV)
Jolly 09	1.25 \times 1.25 \times 8	2.26	-	1.97 (LV)
Peters 09(**)	0.6 \times 0.6 \times 0.8	0.69	0.74	0.83 (LV)
This approach	1.56 \times 1.56 \times 9	0.87 \pm 0.23	1.19 \pm 0.28	0.98 \pm 0.23 (LV+RV)

(*) distances are measured on 2D slices.

(**) surface to surface distance is used as the error measure

(+) both short-axis and long-axis images are used.

5.6.2 On the Establishment of Model Correspondence

As discussed in Section 2.1.2, there are many different methods to enforce the correspondence for landmark-based boundary models. One of them is via mesh-to-volume registration, i.e., adapting a deformable surface model to the segmented binary volumes and defining the correspondences by the vertex locations of the deformable template after the surface evolution has converged. This is the approach adopted in (Kaus et al., 2003; Zhao and Teoh, 2008). The approach in this chapter is similar to this type of correspondence, with the difference that the deformable model I used is medial model, which defines the correspondence on the medial surface and propagates it to the boundary surface, rather than the boundary model, which defines the correspondence directly on the boundary surface. There are several commonly raised concerns for using mesh-to-volume registration to establish the correspondence. The first is the bias introduced by a randomly chosen template. In my approach, the medial template is derived from an iteratively built volumetric template using the the symmetric diffeomorphic registration (Avants and Gee, 2004), which minimized the possible bias. The second concern is how well the deformable model can approximate the shape. The medial model’s ability to approximate the left and right ventricles accurately was demonstrated in Chapter 4 where the deformable medial model is fitted to 428 three-dimensional heart shapes with a mean Dice overlap of 0.92.

Zhao and Teoh (Zhao and Teoh, 2008) proposed to improve the approximating accuracy of the deformable model by introducing “bridging” shapes for those shapes that are not well approximated in the first round of model fitting. This approach can also be adapted in this medial model in the future to further improve the approximation accuracy. The third concern is whether the deformable model is properly constrained, which in this approach the deformable model is regularized by an internal energy to minimize the area-element distortion of the medial surface. This regularization favors a correspondence that is similar to 2D arc-length-based correspondence, which, although can not guarantee to be anatomically meaningful, is a correspondence with explicit geometric interpolation.

5.6.3 Limitations and Future Work

As the first attempt to use statistical medial model to segment the cardiac shapes, this method bears several limitations that can potentially be improved in future research.

First, the landmark-based initialization still requires manual operation, which can be replaced by an automatic heart localization procedure. In the literature, several methods have been proposed to achieve heart localization, such as optimizing a match function between the model and the image using gradient minimization (Lotjonen et al., 2004), using global or local affine registration to propagate a labeled atlas (Zhuang et al., 2008), using machine learning based 3-D object detection method (Zheng et al., 2008). Similar techniques can be tested for the medial model in the future.

Second, the two datasets used are only manually segmented once. Therefore the intraobserver and interobserver variabilities are not performed. This is a limitation of the dataset.

Third, I have only experimented on one type of local texture descriptor in the paper, which is the irreducible Cartesian differential invariants. There are several other compelling texture descriptors, such as Haar wavelets, Gabor wavelets (Daugman, 1988; McKenna et al., 1997), steerable features (Freeman and Adelson, 1991) among others, which might work equally well or even better. An comparative analysis between a number

of image features could be of interest to optimize the segmentation results.

5.7 Conclusion

In this chapter, I present a segmentation method, which, according to my knowledge, is the first reported method using the statistical medial model to segment the left and right ventricular myocardium. The medial model provides a set of unique shape features, including the thickness, which are learned and incorporated as the shape priors in the model-based segmentation. The boundary detection is performed using AdaBoost learning-based classifiers.

The segmentation algorithm is tested on short-axis cardiac MR images and proved to be accurate and robust. The segmentation of the right ventricular myocardium is rarely conducted in the literature due to its thinness nature. I proved that in a typical short-axis cardiac data set, it is possible to segment the right ventricular myocardium pretty accurately. An extra advantage using medial model to segment the myocardium is that it instantly provides the thickness measure which is an important parameter to characterize the myocardium function.

The accuracy of the segmentation is evaluated separately for four different groups: the healthy group, the acute myocardial infarction group, the hypertrophy group and the dilation group. This can be important if the segmentation results are intended to be used in clinical studies so that the segmentation performance can be considered when interpreting the final results.

Chapter 6

Conclusions

6.1 Summary of Contributions

At the end of this work, this chapter revisits the contribution claims laid out in Chapter 1 and discuss limitations and future research. These claims were:

1. *New method: Constructing a 2D cm-rep by obtaining the explicit closed-form solution of the ODE, which is a 2D equivalent of the PDE used in (Yushkevich et al., 2006b).*

This work is built upon the PDE-based cm-rep approach in (Yushkevich et al., 2006b), which enforces the medial equality constraints as the boundary condition of the Poisson PDE. In Chapter 3, the closed-form solution of the corresponding ODE for 2D objects is derived by utilizing Pythagorean hodograph splines (Farouki and Sakkalis, 1990; Farouki and Neff, 1995), so that the PDE-based approach can be efficiently applied to generate cm-rep for 2D objects without the need to numerically solve the ODE in each iteration. However, since the Poisson PDE approach is only feasible for shapes whose medial axes consist of a single medial manifold, the application of this method is limited to simple 2D shapes.

2. *Application: Being the first to use the medial model to perform shape-based normalization of the corpus callosum and to demonstrate potential advantages over a*

registration-based approach.

This application demonstrates the ability of the medial model to provide a shape-based correspondence and to extend the correspondence from the boundary or the medial axis to the entire interior region of the model. The correspondence employed in this experiment is the equal arc-length subdivision of the symmetry curves, which is entirely shape-based. This demonstration of the correspondence based on the 2D medial model also serves as a good justification for the correspondence adopted in the 3D statistical medial model in Chapter 4 and 5, which is enforced by penalizing the area-element distortion of the medial surface and thus achieves a similar effect as the equal arc-length subdivision in 2D.

This shape-based correspondence for corpora callosa is compared with the technique most commonly used to normalize imaging data: volumetric registration. The results using DTI data from a chromosome DS22q11.2 deletion study demonstrate that shape-based normalization of the corpus callosum using cm-reps makes it possible to detect statistical differences between populations that were not detected when registration was used to normalize the structure. A direct comparison of the alignment of connectivity maps between cm-reps and registration gives further justification to the use of cm-reps, suggesting that the shape-based correspondences in the corpus callosum more accurately reflects the underlying anatomical correspondence. The fact that both types of results are stable with respect to the choice and the parameters of the diffusion tensor tractography algorithm adds further weight to our findings.

However, this evaluation is limited to one registration algorithm using one set of parameters. Therefore the conclusion should not be generalized to judge correspondences that are based on other volumetric registration techniques.

3. New method: Constructing a 3D branching medial model by enforcing the equality medial constraints using soft penalty terms and local corrections in the deformable model.

This new approach to construct 3D medial model for complex shapes is given in Chapter 4. This approach allows us to model a large class of shapes using the cm-rep, which not only provides rich descriptive shape features, but also parameterizes the entire model

interior, setting up a framework to perform a combined statistical analysis of shape and appearance. The deformable branching medial model is constructed by first defining a synthetic medial axis (connected manifolds with radial scalar fields) and then obtaining an object whose true medial axis coincides with the synthetic medial axis via *inverse skeletonization*. The validity of such an object depends on a set of medial constraints, including non-linear equality constraints that hold along the edge and branching curves of medial manifolds and inequality constraints that hold everywhere on the medial manifolds. These constraints ensure that the boundary of the object is closed and not self-intersecting. Our method deals with the medial constraints using a simple but efficient approach: enforcing them as soft penalty terms in the deformable model to minimize the violation, and then applying small local corrections to ensure the smoothness of the model boundary. Comparing with existing branching medial models (Yushkevich, 2008; Terriberry and Gerig, 2006), the proposed approach’s simplicity in implementation and low computation load make it easily applicable to model 3D objects with complex shapes.

4. *Application: Using the 3D branching medial model to represent the left and right ventricular myocardium, which yields aligned thickness and thickening maps.*

This experiment answers a critical question: is the medial representation flexible enough to represent the full range of cardiac shape configurations one is likely to encounter in clinical practice. It has long been pointed out in the literature that medial models and skeletons have certain attractive features for shape analysis, including, in particular, the ability to represent thickness explicitly and succinctly. However, there has always been skepticism about the flexibility of medial models: the ability to cover the full range of shapes that one would like to study in a given application. In Chapter 4, the flexibility of medial models is demonstrated by an experiment on a large scale cardiac data set consisting of both healthy subjects and patients.

Medial modeling not only provides descriptive shape features, but also is particularly useful for population-wise comparison and analysis, as demonstrated by the experiment to analyze ventricular thickness map and thickening map on a data set consisting of HCM

patients, AMI patients and subjects with no pathology in the heart.

5. New method: Constructing a statistical medial model comprising a shape prior of the medial manifolds using PCA, a shape prior of the radial thickness field using MRF, and an appearance prior of the image features sampled around the model boundaries using the Adaboost algorithm.

In chapter 5 we present a scheme to construct the statistical medial model for segmentation. Segmentation is an important application of statistical boundary models. The medial model has advantages over the boundary model in terms of providing intuitive shape features, which potentially make better shape priors for image segmentation. Just like there are many different ways to construct a statistical boundary model, we have a large number of choices on how to construct a statistical medial model. The way we choose is similar to the state-of-art ASM, but with all the scheme redesigned to fit the medial model framework.

Two different shape priors are constructed out of different shape features. The PCA approach is used to model the coordinates of the medial pseudo-landmarks, while MRF is used to model the radial scalar field. Boundary detection is performed using Adaboost classifiers built on boundary-based samples. The sampling direction is along the chord direction of the MIB which connects two corresponding boundary nodes, rather than along the perpendicular direction of the boundary surface in ASMs.

6. Application: Being the first to apply the statistical medial model to cardiac image segmentation and show that it can segment the left and right ventricular myocardium accurately.

This probably is the most important application in the thesis. The segmentation of cardiac images is frequently needed for heart function studies. As the first statistical medial model for cardiac segmentation, this experiment is an important demonstration of how well the statistical medial model can perform in such tasks. The experiment reveals that it does work extremely well, providing a robust and accurate result. It successfully segments both the left and right ventricular myocardium, the latter being rarely segmented by

boundary models. And not only can the statistical medial model segment the myocardium accurately, but also it can provide a thickness measure for the myocardium, which is an important function parameter.

6.2 Discussion and Future Work

Chapter 3, 4 and 5 are the three main chapters of this thesis. Each chapter focuses on demonstrating a unique property of the medial model. Chapter 3 demonstrates the power of the medial model to perform shape registration. Chapter 4 demonstrates the ability of the medial model to perform shape analysis. And Chapter 5 demonstrates the power of the medial model in image segmentation.

Chapter 3 connects to the other two chapters rather loosely. Chapter 4 and 5, which describe the methodology developments on 3D branching medial model and the application to cardiac data, are the focus of this thesis. Chapter 3, which describes a 2D method and its application to corpus callosum study, provides supporting evidence on advantages of the correspondence provided by medial geometry. The 3D version of this correspondence is adopted in Chapter 4 and 5. The limitation of Chapter 3 is obvious. There are only a limited number of anatomical structures that lend themselves well to 2D modeling. And the conclusions drawn from 2D studies do not necessarily extend to 3D cases. In that sense, it would be better if a similar study on the correspondence can be conducted on 3D structures to help estimating the correspondence used during the cardiac study in Chapter 4 and 5.

Chapter 4 and 5 are closely connected. They develop 3D branching medial model and apply it to solve problems in cardiac studies. Chapter 4 is the basis and solves the problem of how to stitch the medial manifolds together during the deformable modeling, which is a fundamental problem that all branching cm-rep approaches need to address. It also solves a series of application-specific problems, such as how to build the medial template for cardiac data, how to maintain the mesh quality during model fitting. Chapter 5 is probably the

most important chapter in the thesis. It combines the deformable medial model with the best practices from the ASM literature, such as statistical modeling of appearance, and the use of local search to guide model deformation, and develops an automatic segmentation algorithm of the myocardium in short-axis MRI. To the best of my knowledge, this is the first approach to use deformable medial models for myocardium segmentation. And the performance of the segmentation compares favorably with published works. This good performance is due to a number of reasons, including the Adaboost algorithm which selects best image features in the local appearance modeling, the coupled searching scheme of the endocardial and epicardial borders of the myocardium, and the Markovian prior on myocardial thickness. However, comparing with ASM, this medial-based segmentation algorithm is much slower. A worthwhile research direction in the future would be improving the speed of the algorithm.

Among the techniques that have been proposed for cm-rep, the PDE-based approach provides a solution that is mathematically rigorous and it has been tested by applications on hippocampus (Yushkevich et al., 2006b; Yushkevich, 2008) and white matter tracts (Yushkevich et al., 2008). The biharmonic PED approach is also able to handle branching medial model. The drawback of this approach is that it requires solving a PDE each time the model coefficients are adjusted, which can be cumbersome for deformable modeling. Our model can serve as a near perfect initialization for such PDE-based models.

Bibliography

- L. S. Allen, M. F. Richey, Y. M. Chai, and R. A. Gorski. Sex differences in the corpus callosum of the living human being. *The Journal of neuroscience : the official journal of the Society for Neuroscience.*, 11(4):933–942, Apr 1991.
- H. C. V. Assen, M. G. Danilouchkine, A. F. Frangi, S. Ordás, J. J. Westenberg, J. H. Reiber, and B. P. Lelieveldt. SPASM: A 3D-ASM for segmentation of sparse and arbitrarily oriented cardiac MRI data. *Medical Image Analysis*, 10(2):286–303, 2006.
- B. B. Avants and J. C. Gee. Symmetric geodesic shape averaging and shape interpolation. In *Proc. Mathematical Methods in Biomedical Image Analysis*, pages 99–110, 2004.
- B. B. Avants, M. Grossman, and J. C. Gee. Symmetric diffeomorphic image registration: Evaluating automated labeling of elderly and neurodegenerative cortex and hippocampus. In *Proc. Biomedical Image Registration*, pages 50–57, 2006.
- S. R. Aylward and E. Bullitt. Initialization, noise, singularities, and scale in height ridge traversal for tubular object centerline extraction. *IEEE Transactions on Medical Imaging*, 21(2):61–75, Feb 2002.
- H. Azhari, S. Sideman, J. Weiss, E. Shapiro, M. Weisfeldt, W. Graves, W. Rogers, and R. Beyar. Three-dimensional mapping of acute ischemic regions using MRI: wall thickening versus motion analysis. *American Journal of Physiology*, 259:H1492–1503, Nov 1990.

- A. Bailly, J. Lipiecki, P. Chabrot, A. Alfidja, J. M. Garcier, S. Ughetto, J. Ponsonnaille, and L. Boyer. Assessment of left ventricular volumes and function by cine-mr imaging depending on the investigator's experience. *Surgical and Radiologic Anatomy*, 31(2): 113–120, 2008.
- C. B. Barber, D. P. Dobkin, and H. Huhdanpaa. The quickhull algorithm for convex hulls. *ACM Transactions on Mathematical Software*, 22(4):469–483, 1996.
- A. Barr. Superquadrics and angle-preserving transformations. *IEEE Computer Graphics and Applications*, 1(1):11–23, Jan 1981.
- P. J. Basser and C. Pierpaoli. Microstructural and physiological features of tissues elucidated by quantitative-diffusion-tensor MRI. *Journal of Magnetic Resonance B*, 111: 209–219, 1996.
- P. J. Basser, J. Mattiello, and D. L. Bihan. Estimation of the effective self-diffusion tensor from the NMR spin echo. *Journal of Magnetic Resonance B*, 103:247–254, 1994.
- P. J. Besl and H. D. McKay. A method for registration of 3-d shapes. *IEEE Transactions on Pattern Analysis and Machine Intelligence*, 14(2):239–256, 1992.
- J. M. Bland and D. G. Altman. Statistical methods for assessing agreement between two methods of clinical measurement. *Lancet*, 327(8476):307–310, Feb 1986.
- H. Blum. A transformation for extracting new descriptors of shape. In *Models for the Perception of Speech and Visual Form*. MIT Press, 1967.
- J. Bogaert and A. M. Taylor. Nonischemic myocardial disease. In J. Bogaert, S. Dymarkowski, and A. M. Taylor, editors, *Clinical Cardiac MRI*, volume 1, pages 217–270. Springer-Verlag New York, Inc, 2005.
- E. Bolson and F. Sheehan. Centersurface model for 3d analysis of regional left ventricular function. In *Proc. Computers in Cardiology*, pages 735–738, Sep 1993.

- F. Bookstein. Principal warps: Thin-plate splines and the decomposition of deformations. *IEEE Transactions on Pattern Analysis and Machine Intelligence*, 11:567–585, 1989.
- S. Bouix, J. C. Pruessner, D. L. Collins, and K. Siddiqi. Hippocampal shape analysis using medial surfaces. *Neuroimage*, 25(4):1077–89, May 2005.
- M. Brady and H. Asada. Smoothed local symmetries and their implementation. *The International Journal of Robotics Research*, 3(3):36–61, 1984.
- C. Brechbühler, G. Gerig, and O. Kübler. Parameterization of closed surfaces for 3-D shape description. *Computer Vision, Graphics, and Image Processing: Image Understanding*, 61(154–170), 1995.
- M. Brejl and M. Sonka. Object localization and border detection criteria design in edge-based image segmentation: Automated learning from examples. *IEEE Transactions on Medical Imaging*, 19(10):973–985, 2000.
- J. W. Bruce, P. J. Giblin, and C. G. Gibson. Symmetry sets. *Proc. Royal Society of Edinburgh*, 101A:163–186, 1985.
- O. T. Carmichael, H. A. Aizenstein, S. W. Davis, J. T. Becker, P. M. Thompson, C. C. Meltzer, and Y. Liu. Atlas-based hippocampus segmentation in Alzheimer’s disease and mild cognitive impairment. *Neuroimage*, 27(4):979–90, Oct 2005.
- V. Caselles, R. Kimmel, and G. Sapiro. Geodesic active contours. In *Proc. International Conference on Computer Vision*, pages 694–699, 1995.
- J. Cauvin, J. Boire, M. Zanca, J. Bonny, J. Maublant, and A. Veyre. 3D modeling in myocardial 201TL SPECT. *Computerized Medical Imaging and Graphics*, 17:345–350, 1993.
- M. D. Cerqueira, N. J. Weissman, V. Dilsizian, A. K. Jacobs, S. Kaul, W. K. Laskey, D. J. Pennell, J. A. Rumberger, T. Ryan, and M. S. a. Verani. Standardized myocardial

- segmentation and nomenclature for tomographic imaging of the heart: a statement for healthcare professionals from the cardiac imaging committee of the council on clinical cardiology of the american heart association. *Circulation*, 105(4):539–542, Jan 2002.
- C. Chen, J. Luo, K. Parker, and T. Huang. CT volumetric data-based left ventricle motion estimation: an integrated approach. *Comput Med Imaging Graph*, 19:85–100, 1995.
- H. I. Choi, S. W. Choi, and H. P. Moon. Mathematical theory of medial axis transform. *Pacific Journal of Mathematics*, 181(1):57–88, 1997.
- H. I. Choi, C. Y. Han, H. P. Moon, K. H. Roh, and N.-S. Wee. Medial axis transform and offset curves by minkowski pythagorean hodograph curves. *Computer-Aided Design*, 31, 1999.
- G. Christensen, S. Joshi, and M. Miller. Volumetric transformation of brain anatomy. *IEEE Transactions on Medical Imaging*, 16:864–877, 1997.
- P. A. Cook, H. Zhang, B. B. Avants, P. A. Yushkevich, D. C. Alexander, J. C. Gee, O. Ciccarelli, and A. J. Thompson. An automated approach to connectivity-based partitioning of brain structures. In *Proc. Medical Image Computing and Computer-Assisted Intervention*, pages 164–171, 2005.
- P. A. Cook, Y. Bai, M. G. Hall, S. Nedjati-Gilani, K. K. Seunarine, G. J. M. Parker, and D. C. Alexander. Camino: Open-source diffusion-MRI reconstruction and processing. In *Proc. Scientific Meeting of the International Society for Magnetic Resonance in Medicine*, page 2759, 2006.
- T. F. Cootes and C. J. Taylor. A mixture model for representing shape variation. In *Proc. Image and Vision Computing*, pages 110–119. BMVA Press, 1997.
- T. F. Cootes, C. J. Taylor, D. H. Cooper, and J. Graham. Active shape models – Their training and application. *Computer Vision and Image Understanding*, 61(1):38–59, Jan 1995.

- T. F. Cootes, G. J. Edwards, and C. J. Taylor. Active appearance models. *IEEE Transactions on Pattern Analysis and Machine Intelligence*, 23(6):681–685, 2001.
- I. Corouge, P. T. Fletcher, S. Joshi, S. Gouttard, and G. Gerig. Fiber tract-oriented statistics for quantitative diffusion tensor MRI analysis. *Medical Image Analysis*, 10:786–798, 2006.
- J. Csernansky, S. Joshi, L. Wang, J. Haller, M. Gado, J. Miller, U. Grenander, and M. Miller. Hippocampal morphometry in schizophrenia via high dimensional brain mapping. In *Proc. National Academy of Sciences*, volume 95, pages 11406–11411, 1998.
- J. Damon. Determining the geometry of boundaries of objects from medial data. *International Journal of Computer Vision*, 63(1):45–64, 2005.
- J. Daugman. Complete discrete 2-d gabor transforms by neural networks for imageanalysis and compression. *IEEE Transactions on Acoustics, Speech and Signal Processing*, 37(7):1169–1179, 1988.
- C. Davatzikos, M. Vaillant, S. Resnick, J. Prince, S. Letovsky, and R. Bryan. A computerized approach for morphological analysis of the corpus callosum. *Journal of Computer Assisted Tomography*, 20:207–222, 1995.
- R. H. Davies. *Learning Shape: Optimal Models for Analysing Natural Variability*. PhD thesis, University of Manchester, 2002.
- R. H. Davies, C. J. Twining, T. F. Cootes, J. C. Waterton, and C. J. Taylor. A minimum description length approach to statistical shape modeling. *IEEE Transactions on Medical Imaging*, 21(5):525–37, 2002.
- M. de Bruijne, B. van Ginneken, W. J. Niessen, M. Loog, and M. A. Viergever. Model-based segmentation of abdominal aortic aneurysms in cta images. In *Proc. of SPIE Medical Imaging: Image Processing*, volume 5032, pages 1560–1571. Press, Feb 2003.

- F. De La Torre and M. J. Black. A framework for robust subspace learning. *International Journal of Computer Vision*, 54(1-3):117–142, 2003.
- C. DeLacoste-Utamsing and R. L. Holloway. Sexual dimorphism in the human corpus callosum. *Science*, 216(4553):1431–1432, June 1982.
- L. R. Dice. Measures of the amount of ecologic association between species. *Journal of Ecology*, 26:297–302, 1945.
- I. L. Dryden and K. Mardia. *Statistical Shape Analysis*. John Wiley and Sons, 1998.
- S. Dymarkowski, J. Bogaert, and Y. Ni. Ischemic heart disease. In J. Bogaert, S. Dymarkowski, and A. M. Taylor, editors, *Clinical Cardiac MRI*, volume 1, pages 173–216. Springer-Verlag New York, Inc, 2005.
- B. S. Emanuel, D. McDonald-McGinn, S. C. Saitta, and E. H. Zackai. The 22q11.2 deletion syndrome. *Advances in pediatrics*, 48:39–73, 2001.
- A. Ericsson and K. Astrom. Minimizing the description length using steepest descent. In *Proc. British Machine Vision Conference*, volume 2, pages 93–102, 2003.
- R. T. Farouki and C. A. Neff. Hermite interpolation by Pythagorean hodograph quintics. *Journal of Computational Mathematics*, 64(212):1589–1609, Oct 1995.
- R. T. Farouki and T. Sakkalis. Pythagorean hodographs. *IBM Journal of Research and Development*, 34:736–752, 1990.
- P. T. Fletcher and S. C. Joshi. Principal geodesic analysis on symmetric spaces: Statistics of diffusion tensors. In *Proc. Computer Vision and Mathematical Methods in Medical and Biomedical Image Analysis*, pages 87–98, 2004.
- P. T. Fletcher, C. Lu, S. M. Pizer, and S. Joshi. Principal geodesic analysis for the study of nonlinear statistics of shape. *IEEE Transactions on Medical Imaging*, 23(8):995–1005, Aug 2004.

- J. Foong, M. Maier, C. A. Clark, G. J. Barker, D. H. Miller, and M. A. Ron. Neuropathological abnormalities of the corpus callosum in schizophrenia: a diffusion tensor imaging study. *Journal of Neurology, Neurosurgery, and Psychiatry*, 68(2):242–244, Feb 2000.
- A. Frangi, W. Niessen, and M. Viergever. Three-dimensional modeling for functional analysis of cardiac images: a review. *IEEE Transactions on Medical Imaging*, 20:2–25, Jan 2001a.
- A. F. Frangi, D. Rueckert, J. A. Schnabel, and W. J. Niessen. Automatic 3d asm construction via atlas-based landmarking and volumetric elastic registration. In *Proc. International Conference on Information Processing in Medical Imaging*, pages 78–91, London, UK, 2001b. Springer-Verlag.
- A. F. Frangi, D. Rueckert, J. A. Schnabel, and W. J. Niessen. Automatic construction of multiple-object three-dimensional statistical shape models: application to cardiac modeling. *IEEE Transactions on Medical Imaging*, 21:1151–1166, Sep 2002.
- W. T. Freeman and E. H. Adelson. The design and use of steerable filters. *IEEE Transactions on Pattern Analysis and Machine Intelligence*, 13:891–906, 1991.
- Y. Freund and R. E. Schapire. A decision-theoretic generalization of on-line learning and an application to boosting. *Journal of Computer and System Sciences*, 55(1):119–139, 1997.
- K. Friston, K. Worsley, R. Frackowiak, J. Mazziotta, and A. Evans. Assessing the significance of focal activations using their spatial extent. *Human Brain Mapping*, 1:214–220, 1994.
- M. Galassi, J. Davies, J. Theiler, B. Gough, G. Jungman, M. Booth, and F. Rossi. *GNU Scientific Library Reference Manual*. 2nd edition. ISBN 0-9541617-3-4.

- J. C. Gee, H. Zhang, A. Dubb, B. B. Avants, P. A. Yushkevich, and J. T. Duda. Anatomy-based visualizations of diffusion tensor images of brain white matter. In J. Welckert and H. Hagen, editors, *Visualization and Image Processing of Tensor Fields*, pages 155–163. Berlin:Springer, 2005.
- G. Gerig, K. E. Muller, E. O. Kistner, Y. Chi, M. Chakos, M. Styner, and J. A. Lieberman. Age and treatment related local hippocampal changes in schizophrenia explained by a novel shape analysis method. In *Proc. Medical Image Computing and Computer-Assisted Intervention*, 2003.
- G. Germano, H. Kiat, P. Kavanagh, M. Moriel, M. Mazzanti, H. Su, K. Van Train, and D. Berman. Automatic quantification of ejection fraction from gated myocardial perfusion SPECT. *The Journal of Nuclear Medicine*, 36:2138–2147, Nov 1995.
- P. Giblin and B. Kimia. A formal classification of 3D medial axis points and their local geometry. In *IEEE Computer Society Conference on Computer Vision and Pattern Recognition*, pages 566–573, 2000.
- P. J. Giblin and B. B. Kimia. On the intrinsic reconstruction of shape from its symmetries. *IEEE Transactions on Pattern Analysis and Machine Intelligence*, 25(7):895–911, 2003.
- P. Golland, W. Grimson, and R. Kikinis. Statistical shape analysis using fixed topology skeletons: corpus callosum study. In *International Conference on Information Processing in Medical Imaging*, LNCS 1613, pages 382–388. Springer Verlag, 1999.
- A. Gopal, D. King, J. Katz, L. Boxt, D. King, and M. Shao. Three-dimensional echocardiographic volume computation by polyhedral surface reconstruction: in vitro validation and comparison to magnetic resonance imaging. *Journal of the American Society of Echocardiography*, 5:115–124, 1992.
- J. C. Gower. Generalized procrustes analysis. *Psychometrika*, pages 33–51, 1975.

- T. Gustavsson, R. Pascher, and K. Caidahl. Model based dynamic 3D reconstruction and display of the left ventricle from 2D cross-sectional echocardiograms. *Computerized Medical Imaging and Graphics*, 17:273–278, 1993.
- F. Haddad, S. A. Hunt, D. N. Rosenthal, and D. J. Murphy. Right ventricular function in cardiovascular disease, part i: Anatomy, physiology, aging, and functional assessment of the right ventricle. *Circulation*, 117(11):1436–1448, Mar 2008.
- Q. Han, C. Lu, G. Liu, S. M. Pizer, S. Joshi, and A. Thall. Representing multiframe anatomical objects. In *Proc. IEEE International Symposium on Biomedical Imaging*, pages 1251–1254, 2004.
- Q. Han, S. M. Pizer, D. Merck, S. Joshi, and J.-Y. Jeong. Multi-figure anatomical objects for shape statistics. In *Proc. Information Processing in Medical Imaging*, pages 701–712, 2005.
- Q. Han, S. M. Pizer, and J. N. Damon. Interpolation in discrete single figure medial objects. In *Proc. Conference on Computer Vision and Pattern Recognition Workshop*, page 85, Washington, DC, USA, 2006. IEEE Computer Society.
- S. Hayasaka and T. E. Nichols. Validating cluster size inference: random field and permutation methods. *Neuroimage*, 20(4):2343–2356, Dec 2003.
- A. Hyvärinen and E. Oja. Independent component analysis: algorithms and applications. *Neural Networks*, 13(4-5):411–430, 2000.
- L. K. Jacobsen, J. N. Giedd, J. C. Rajapakse, S. D. Hamburger, A. C. Vaituzis, J. A. Frazier, M. C. Lenane, and J. L. Rapoport. Quantitative magnetic resonance imaging of the corpus callosum in childhood onset schizophrenia. *Psychiatry Research*, 68(2-3): 77–86, Feb 1997.
- M.-P. Jolly, H. Xue, L. Grady, and J. Guehring. Combining registration and minimum surfaces for the segmentation of the left ventricle in cardiac cine MR images. In *Proc.*

- Medical Image Computing and Computer-Assisted Intervention*, volume II of *LNCS*, pages 910–918. Springer-Verlag, 2009.
- S. Joshi. *Large Deformation Diffeomorphisms and Gaussian Random Fields for Statistical Characterization of Brain Sub-Manifolds*. PhD thesis, Washington Univ., St. Louis, MO, 1997.
- S. Joshi, S. Pizer, P. Fletcher, P. Yushkevich, A. Thall, and J. Marron. Multi-scale deformable model segmentation and statistical shape analysis using medial descriptions. *IEEE Transactions on Medical Imaging*, 21(5):538–550, 2002.
- S. Joshi, B. Davis, M. Jomier, and G. Gerig. Unbiased diffeomorphic atlas construction for computational anatomy. *Neuroimage*, 23 Suppl 1:S151–S160, 2004.
- M. A. Just, V. L. Cherkassky, T. A. Keller, R. K. Kana, and N. J. Minshew. Functional and anatomical cortical underconnectivity in autism: Evidence from an fmri study of an executive function task and corpus callosum morphometry. *Cerebral Cortex*, June 2006.
- M. Kaus, V. Pekar, C. Lorenz, R. Truyen, S. Lobregt, and J. Weese. Automated 3d pdm construction from segmented images using deformable models. *IEEE Transactions on Medical Imaging*, 22(8):1005–1013, 2003.
- A. Kelemen, G. Szekely, and G. Gerig. Elastic model-based segmentation of 3-d neuro-radiological data sets. *IEEE Transactions on Medical Imaging*, 18(10):828–839, Oct 1999.
- B. Kimia, A. Tannenbaum, and S. Zucker. Shape, shocks, and deformations I: the components of two-dimensional shape and the reaction-diffusion space. *International Journal of Computer Vision*, 15:189–224, 1995.
- A. Kotcheff and C. Taylor. Automatic construction of eigenshape models by direct optimization. *Medical Image Analysis*, 2:303–314, Dec 1998.

- A. C. W. Kotcheff and C. J. Taylor. Automatic construction of eigenshape models by genetic algorithm. *Information Processing in Medical Imaging*, pages 1–14, 1997.
- K. K. Kubota. Pythagorean triples in unique factorization domains. *The American Mathematical Monthly*, 79:503–505, 1972.
- R. M. Lapp, M. Lorenzo-Valdés, and D. Rueckert. 3d/4d cardiac segmentation using active appearance models, non-rigid registration, and the insight toolkit. In *Proc. Medical Image Computing and Computer-Assisted Intervention*, pages 419–426, 2004.
- C. Li, C.-Y. Kao, J. C. Gore, and Z. Ding. Implicit active contours driven by local binary fitting energy. In *Proc. IEEE Conference on Computer Vision and Pattern Recognition*, pages 1–7, 2007.
- Y. Li and W. Ito. Shape parameter optimization for adaboosted active shape model. In *IEEE International Conference on Computer Vision (ICCV) Volume 1*, pages 251–258, Washington, DC, USA, 2005. IEEE Computer Society.
- C. Loop and T. DeRose. Generalized b-spline surfaces of arbitrary topology. In *Computer Graphics (ACM SIGGRAPH Proceedings)*, pages 347–356, 1990.
- C. Lorenz and J. von Berg. A comprehensive shape model of the heart. *Medical Image Analysis*, 10:657–670, 2006.
- J. Lotjonen, S. Kivisto, J. Koikkalainen, D. Smutek, and K. Lauerma. Statistical shape model of atria, ventricles and epicardium from short- and long-axis mr images. *Medical Image Analysis*, 8(3):371–386, 2004.
- R. Malladi and J. A. Sethian. Image processing via level set curvature flow. *Proceedings of the National Academy of Sciences*, 92(15):7046–50, 1995.
- T. Mansi, S. Durrleman, B. Bernhardt, M. Sermesant, H. Delingette, I. Voigt, P. Lurz, A. M. Taylor, J. Blanc, Y. Boudjemline, X. Pennec, and N. Ayache. A statistical model

- of right ventricle in tetralogy of fallot for prediction of remodelling and therapy planning. In *Proc. Medical Image Computing and Computer-Assisted Intervention*, pages 214–221, 2009.
- A. Matheny and D. B. Goldgof. The use of three- and four-dimensional surface harmonics for rigid and nonrigid shape recovery and representation. *IEEE Transactions on Pattern Analysis and Machine Intelligence*, 17(10):967–981, 1995.
- S. J. McKenna, S. Gong, R. P. Würtz, J. Tanner, and D. Banin. Tracking facial feature points with gabor wavelets and shape models. In *Proc. International Conference on Audio- and Video-Based Biometric Person Authentication*, pages 35–42, London, UK, 1997. Springer-Verlag.
- M. Miller, M. Beg, C. Ceritoglu, and C. Stark. Increasing the power of functional maps of the medial temporal lobe using large deformation metric mapping. *Proc. National Academy of Sciences of the USA*, 102:9685–9690, 2005.
- S. C. Mitchell, J. G. Bosch, B. P. F. Lelieveldt, R. J. van der Geest, J. H. C. Reiber, and M. Sonka. 3-d active appearance models: segmentation of cardiac mr and ultrasound images. *IEEE Transactions on Medical Imaging*, 21(9):1167–1178, 2002.
- S. Mori and P. C. M. van Zijl. Fiber tracking: principles and strategies: a technical review. *NMR in Biomedicine*, 15:468–480, 2002.
- S. Mori, B. J. Crain, V. P. Chacko, and P. C. M. van Zijl. Three dimensional tracking of axonal projections in the brain by magnetic resonance imaging. *Annals of Neurology*, 45:265–269, 1999.
- J. Morra, Z. Tu, L. Apostolova, A. Green, A. Toga, and P. Thompson. Comparison of adaboost and support vector machines for detecting alzheimer’s disease through automated hippocampal segmentation. *IEEE Transactions On Medical Imaging*, 29(1): 30–43, Jan 2010.

- M. Näf, O. Kübler, R. Kikinis, M. Shenton, and G. Székely. Characterization and recognition of 3D organ shape in medical image analysis using skeletonization. In *Proc. Mathematical Methods in Biomedical Image Analysis Workshop*, pages 139–150. IEEE Computer Society, 1996.
- R. L. Ogniewicz and O. Kübler. Hierarchic Voronoi skeletons. *Pattern Recognition*, 28(3):343–359, 1995.
- N. Paragios. A variational approach for the segmentation of the left ventricle in cardiac image analysis. *International Journal of Computer Vision*, 50(3):345–362, 2002.
- J. Peters, O. Ecabert, C. Meyer, R. Kneser, and J. Weese. Optimizing boundary detection via simulated search with applications to multi-modal heart segmentation. *Medical Image Analysis*, 14:70–84, October 2009.
- J.-M. Peyrat, H. Delingette, M. Sermesant, X. Pennec, C. Xu, and N. Ayache. Registration of 4d time-series of cardiac images with multichannel diffeomorphic demons. In *Proc. Medical Image Computing and Computer-Assisted Intervention*, pages 972–979, 2008.
- A. Pitiot, H. Delingette, and P. M. Thompson. Learning shape correspondence for n-d curves. *International Journal of Computer Vision*, 71(1):71–88, 2007.
- J. Piven, J. Bailey, B. J. Ranson, and S. Arndt. An mri study of the corpus callosum in autism. *The American Journal of Psychiatry*, 154(8):1051–1056, Aug 1997.
- S. M. Pizer, D. S. Fritsch, P. A. Yushkevich, V. E. Johnson, and E. L. Chaney. Segmentation, registration, and measurement of shape variation via image object shape. *IEEE Transactions on Medical Imaging*, 18(10):851–65, Oct 1999.
- S. M. Pizer, S. Joshi, T. P. Fletcher, M. Styner, G. Tracton, and J. Z. Chen. Segmentation of single-figure objects by deformable m-reps. In *Proc. Medical Image Computing and Computer-Assisted Intervention*, pages 862–871, 2001.

- S. M. Pizer, P. T. Fletcher, S. Joshi, A. Thall, J. Z. Chen, Y. Fridman, D. S. Fritsch, A. G. Gash, J. M. Glotzer, M. R. Jiroutek, C. Lu, K. E. Muller, G. Tracton, P. Yushkevich, and E. L. Chaney. Deformable m-reps for 3D medical image segmentation. *International Journal of Computer Vision*, 55(2):85–106, Nov 2003.
- A. Rangarajan, H. Chui, and F. L. Bookstein. The softassign procrustes matching algorithm. In *International Conference on Information Processing in Medical Imaging*, pages 29–42, London, UK, 1997. Springer-Verlag.
- T. Rohlfing. Transformation model and constraints cause bias in statistics on deformation fields. In *Proc. Medical Image Computing and Computer-Assisted Intervention*, pages 207–214, 2006.
- D. Scellier, J.-Y. Boire, C. Thouly, and J. Maublant. Application of skeletonization algorithms for myocardial spect quantification. In *Proc. the 6th International Workshop on Discrete Geometry for Computer Imagery*, pages 227–236, London, UK, 1996. Springer-Verlag.
- C. Schmid and R. Mohr. Local greyvalue invariants for image retrieval. *IEEE Transactions on Pattern Analysis and Machine Intelligence*, 19:530–535, 1997.
- J. A. Sethian. *Level set methods: evolving interfaces in geometry, fluid mechanics, computer vision, and material sciences*. Cambridge University Press, 1996.
- F. Sheehan and A. Redington. The right ventricle: anatomy, physiology and clinical imaging. *Heart*, 94(11):1510–1515, 2008.
- F. Sheehan, E. Bolson, H. Dodge, D. Mathey, J. Schofer, and H. Woo. Advantages and applications of the centerline method for characterizing regional ventricular function. *Circulation*, 74:293–305, Aug 1986.
- P. Shi, A. Sinusas, R. Constable, E. Ritman, and J. Duncan. Point-tracked quantitative

- analysis of left ventricular surface motion from 3-D image sequences. *IEEE Transactions on Medical Imaging*, 19:36–50, Jan 2000.
- K. Siddiqi, A. Ahokoufandeh, S. Dickinson, and S. Zucker. Shock graphs and shape matching. *International Journal of Computer Vision*, 1(35):13–32, 1999.
- K. Sjöstrand, E. Rostrup, C. Ryberg, R. Larsen, C. Studholme, H. Baezner, J. Ferro, F. Fazekas, L. Pantoni, D. Inzitari, and G. Waldemar. Sparse decomposition and modeling of anatomical shape variation. *IEEE Transactions on Medical Imaging*, 26(12):1625–1635, feb 2007.
- L. Staib and J. Duncan. Model-based deformable surface finding for medical images. *IEEE Transactions on Medical Imaging*, 15:720–731, 1996.
- L. H. Staib and J. S. Duncan. Boundary finding with parametrically deformable models. *IEEE Transactions on Pattern Analysis and Machine Intelligence*, 14(11):1061–1075, 1992.
- C. E. L. Stark and Y. Okado. Making memories without trying: Medial temporal lobe activity associated with incidental memory formation during recognition.
- M. B. Stegmann, K. Sjöstrand, and R. Larsen. Sparse modeling of landmark and texture variability using the orthomax criterion. In *International Symposium on Medical Imaging 2006, San Diego, CA*, volume 6144. The International Society for Optical Engineering (SPIE), feb 2006.
- M. Styner, G. Gerig, S. Joshi, and S. Pizer. Automatic and robust computation of 3D medial models incorporating object variability. *International Journal of Computer Vision*, 55(2):107–122, Nov 2003a.
- M. Styner, G. Gerig, J. Lieberman, D. Jones, and D. Weinberger. Statistical shape analysis of neuroanatomical structures based on medial models. *Medical Image Analysis*, 7(3):207–20, Sept 2003b.

- M. Styner, K. Rajamani, L. Nolte, G. Zsemlye, G. Székely, C. Taylor, and R. H. Davies. Evaluation of 3D correspondence methods for model building. In *International Conference on Information Processing in Medical Imaging*, 2003c.
- M. A. Styner, I. Oguz, R. G. Smith, C. Cascio, and M. Jomier. Corpus callosum subdivision based on a probabilistic model of inter-hemispheric connectivity. In *Proc. Medical Image Computing and Computer-Assisted Intervention*, pages 765–772, 2005.
- G. Subsol, J.-P. Thirion, and N. Ayache. A scheme for automatically building three-dimensional morphometric anatomical atlases: application to a skull atlas. *Medical Image Analysis*, 2(1):37–60, Mar 1998.
- F. M. Sukno, S. Ordas, C. Butakoff, S. Cruz, and A. F. Frangi. Active shape models with invariant optimal features: Application to facial analysis. *IEEE Transactions on Pattern Analysis and Machine Intelligence*, 29(7):1105–1117, 2007.
- H. Sun, P. A. Yushkevich, J. N. Giedd, G. Gerig, and J. C. Gee. Corpus callosum morphometry in childhood-onset schizophrenia. In *Proc. The International Society for Magnetic Resonance in Medicine*, 2007a.
- H. Sun, P. A. Yushkevich, H. Zhang, P. A. Cook, J. T. Duda, T. J. Simon, and J. C. Gee. Shape-based normalization of the corpus callosum for dti connectivity analysis. *IEEE Transactions on Medical Imaging*, 26(9):1166–1178, 2007b.
- H. Sun, B. B. Avants, A. F. Frangi, S. Ordas, J. C. Gee, and P. A. Yushkevich. Branching medial models for cardiac shape representation. In *Proc. IEEE International Symposium on Biomedical Imaging*, pages 1485–1488, 2008a.
- H. Sun, B. B. Avants, A. F. Frangi, F. Sukno, J. C. Gee, and P. A. Yushkevich. Cardiac medial modeling and time-course heart wall thickness analysis. In *Proc. Medical Image Computing and Computer-Assisted Intervention*, pages 766–773, 2008b.

- H. Sun, C. Tobon-Gomez, S. R. Das, M. Huguet, P. A. Yushkevich, and A. F. Frangi. Ventricular wall thickness analysis in acute myocardial infarction and hypertrophic cardiomyopathy. In *Proc. IEEE International Symposium on Biomedical Imaging*, pages 670–673, 2009.
- G. Székely, A. Kelemen, C. Brechbühler, and G. Gerig. Segmentation of 2-d and 3-d objects from mri volume data using constrained elastic deformations of flexible fourier contour and surface models. *Medical Image Analysis*, 1(1):19–34, 1996.
- H. Tagare, D. O’Shea, and A. Rangarajan. A geometric criterion for shape-based non-rigid correspondence. *Proc. International Conference on Computer Vision*, page 434, 1995.
- T. B. Terriberry. *Continuous Medial Models in Two-Sample Statistics of Shape*. PhD thesis, University of North Carolina at Chapel Hill, 2006.
- T. B. Terriberry and G. Gerig. A continuous 3-D medial shape model with branching. In *Medical Image Computing and Computer-Assisted Intervention, MFCA Workshop Proceedings*, 2006.
- A. Thall. Fast C^2 interpolating subdivision surfaces using iterative inversion of stationary subdivision rules. Technical report TR02-001, University of North Carolina, Chapel Hill, 2002.
- A. Thall. *Deformable solid modeling via medial sampling and displacement subdivision*. PhD thesis, Dept. of Comp. Sci., UNC Chapel Hill, 2004.
- H. Thodberg. Minimum description length shape and appearance models. In C. Taylor and J. A. Noble, editors, *Proc. Information Processing in Medical Imaging*, Lecture Notes in Computer Science, pages 51–62, 2003.
- P. Thompson, K. Hayashi, G. de Zubicaray, A. Janke, S. Rose, J. Semple, M. Hong, D. Herman, D. Gravano, S. Dittmer, D. D.M., and A. Toga. Improved detection and mapping of dynamic hippocampal and ventricular change in Alzheimers disease using

- 4D parametric mesh skeletonization. In *9th Annual Meeting of the Organization for Human Brain Mapping*, 2003.
- P. M. Thompson, C. Schwartz, and A. W. Toga. High-resolution random mesh algorithms for creating a probabilistic 3d surface atlas of the human brain. *Neuroimage*, (1):19–34, 1996.
- A. Tsai, A. Yezzi, W. Wells, C. Tempany, D. Tucker, A. Fan, W. Grimson, and A. Willsky. A shape-based approach to the segmentation of medical imagery using level sets. *IEEE Transactions on Medical Imaging*, 22:137–154, Feb 2003.
- Y.-H. Tseng, J.-N. Hwang, and F. H. Sheehan. 3-d heart modeling and motion estimation-based on continuous distance transform neural networks and affine transform. *Journal of VLSI Signal Processing Systems*, 18(3):207–218, 1998.
- N. Tustison and A. Amini. Biventricular myocardial strains via nonrigid registration of anatomical NURBS model. *IEEE Transactions on Medical Imaging*, 25:94–112, Jan 2006.
- C. Twining and C. Taylor. Kernel principal component analysis and the construction of non-linear active shape models. In *Proc. British Machine Vision Conference*, pages 23–32, 2001.
- C. N. Vidal, R. Nicolson, T. J. DeVito, K. M. Hayashi, J. A. Geaga, D. J. Drost, P. C. Williamson, N. Rajakumar, Y. Sui, R. A. Dutton, A. W. Toga, and P. M. Thompson. Mapping corpus callosum deficits in autism: an index of aberrant cortical connectivity. *Biological Psychiatry*, 60(3):218–225, Aug 2006.
- K. N. Walker, T. F. Cootes, and C. J. Taylor. Correspondence using distinct points based on image invariants. In *Proc. British Machine Vision Conference*, volume 1, pages 540–549, 1997.

- M. Wierzbicki, J. Moore, M. Drangova, and T. Peters. Subject-specific models for image-guided cardiac surgery. *Physics in Medicine and Biology*, 53:5295–5312, 2008.
- S. F. Witelson. Hand and sex differences in the isthmus and genu of the human corpus callosum. a postmortem morphological study. *Brain*, 112 (Pt 3):799–835, June 1989.
- P. W. Woodruff, M. L. Phillips, T. Rushe, I. C. Wright, R. M. Murray, and A. S. David. Corpus callosum size and inter-hemispheric function in schizophrenia. *Schizophrenia Research*, 23(3):189–196, Feb 1997.
- G. Xu. Discrete laplace-beltrami operators and their convergence. *Computer Aided Geometric Design*, 21(8):767–784, 2004.
- A. Yezzi, S. Kichenassamy, A. Kumar, P. Olver, and A. Tannenbaum. A geometric snake model for segmentation of medical imagery. *IEEE Transactions on Medical Imaging*, 16:199–209, Apr 1997.
- P. Yushkevich, S. M. Pizer, S. C. Joshi, and J. S. Marron. Intuitive, localized analysis of shape variability. In *IPMI '01: Proceedings of the 17th International Conference on Information Processing in Medical Imaging*, pages 402–408, London, UK, 2001. Springer-Verlag.
- P. Yushkevich, P. T. Fletcher, S. Joshi, A. Thall, and S. M. Pizer. Continuous medial representations for geometric object modeling in 2D and 3D. *Image and Vision Computing*, 21(1):17–28, 2003.
- P. Yushkevich, A. Dubb, Z. Xie, R. Gur, R. Gur, and J. Gee. Regional structural characterization of the brain of schizophrenia patients. *Academic Radiology*, 12(10):1250–61, Oct 2005.
- P. A. Yushkevich. Continuous medial representation of brain structures using the biharmonic pde. *Neuroimage*, (1 Suppl):s99–110, 2008.

- P. A. Yushkevich, J. Piven, H. Cody Hazlett, R. Gimpel Smith, S. Ho, J. C. Gee, and G. Gerig. User-guided 3D active contour segmentation of anatomical structures: Significantly improved efficiency and reliability. *Neuroimage*, 31(3):1116–1128, 2006a.
- P. A. Yushkevich, H. Zhang, and J. Gee. Continuous medial representation for anatomical structures. *IEEE Transactions on Medical Imaging*, 25(2):1547–1564, Dec 2006b.
- P. A. Yushkevich, H. Zhang, T. J. Simon, and J. C. Gee. Structure-specific statistical mapping of white matter tracts. *NeuroImage*, (2):448–461, 2008.
- X. Zeng, L. H. Staib, R. T. Schultz, and J. S. Duncan. Volumetric layer segmentation using coupled surfaces propagation. In *Proc. IEEE Conference on Computer Vision and Pattern Recognition*, pages 708–715, Santa Barbara, CA, 1998.
- Z. Zhao and E. K. Teoh. A new scheme for automated 3d pdm construction using deformable models. *Image and Vision Computing*, 26(2):275–288, 2008.
- Y. Zheng, A. Barbu, B. Georgescu, M. Scheuering, and D. Comaniciu. Four-chamber heart modeling and automatic segmentation for 3-d cardiac ct volumes using marginal space learning and steerable features. *IEEE Transactions on Medical Imaging*, 27(11):1668–1681, 2008.
- X. Zhuang, K. Rhode, S. Arridge, R. Razavi, D. Hill, D. Hawkes, and S. Ourselin. An atlas-based segmentation propagation framework using locally affine registration — application to automatic whole heart segmentation. In *Proc. Medical Image Computing and Computer-Assisted Intervention*, pages 425–433, Berlin, Heidelberg, 2008. Springer-Verlag.